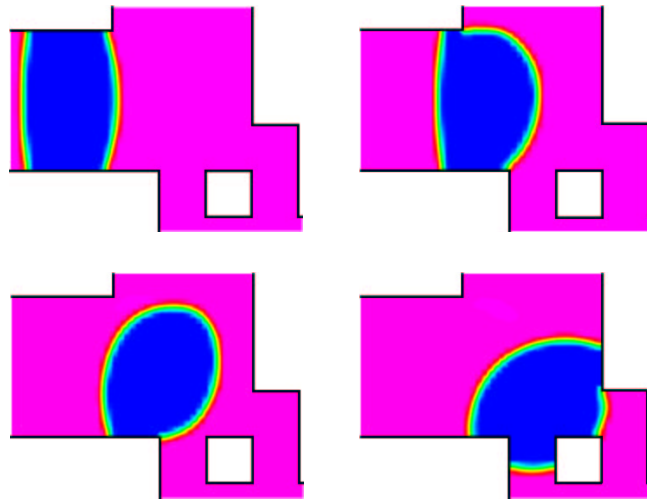


MASTER PROJECT, c960853

# BUBBLES IN MICROCHANNELS

MADS JAKOB JENSEN



Supervisors: Henrik Bruus and Goran Goranović

Mikroelektronik Centret - MIC  
Technical University of Denmark



May 1<sup>st</sup>, 2002



# Abstract

Advances made during the last decades in the microfluidic field have drawn attention to the need of an increased theoretical and computational effort. This thesis combines a theoretical study of two-phase and three-phase flows with numerical simulations of actual bubbles in microstructures.

The theoretical understanding of effects related to surface tension such as contact angle, wetting phenomenon, moving bubbles, and the so-called clogging pressure is essential. Moreover the specific impact of different channel geometries on the behavior of bubbles is studied. A MATLAB program developed by the author and the commercial CFD-ACE+ software are utilized for that purpose.

During the thesis work a great amount of insight into CFD-ACE+ is gained. The free surface handling VOF-method (Volume-Of-Fluid) is investigated thoroughly in several examples. Shortcomings regarding the free surface module are pinpointed and commented. The properties of two types of channel contractions, the sudden contraction and the tapered channel, are compared. The tapered channel geometry exhibits many advantages. Based on the insights gained a novel bubble trap is developed and simulated.

The thesis work both pinpoints several important geometric features having an influence on bubble motion in microchannels and identifies lacks in the numerical implementation of boundary conditions at contact lines.



# Resumé

De fremskridt, der er gjort inden for mikrofluidikken i de sidste årtier, har hængt opmærksomheden på, at der er behov for en øget indsats på det teoretiske og simuleringsmæssige område. Denne afhandling kombinerer en teoretisk undersøgelse af to- og trefase strømninger med numeriske simuleringer af faktiske bobler i mikrostrukturer.

Det er vigtigt at få en teoretisk forståelse af overfladespændingseffekter som f.eks. kontaktvinkel, ”wetting”-fænomener, bobler i bevægelse og de såkaldte ”clogging”-tryk (tilstopningstryk). Desuden er forskellige kanalgeometriers særlige indflydelse på, hvorledes bobler opfører sig i kanaler, blevet undersøgt. Hertil er anvendt et af forfatteren udviklet MATLAB-program samt den kommercielle CFD-ACE+ programpakke.

Under projektføreløbet er der erhvervet stor erfaring med CFD-ACE+ . Gennem flere eksempler er VOF-metoden (Volume-Of-Fluid) for frie overflader blevet indgående undersøgt, og mangler er herved blevet fundet og kommenteret. Egenskaberne ved to typer kanalindsnævninger, den pludselige indsnævring og den tilspidsede kanal, er blevet sammenlignet. Herved påvises de mange fordele, der er forbundet med geometrien for den tilspidsede kanal. På baggrund af den opnåede viden er en ny og innovativ geometri til at fange bobler blevet udviklet og simuleret.

Mange vigtige geometriske egenskaber, der har indflydelse på boblers dynamik i mikrokanaler, er blevet påvist under arbejdet med projektet, ligesom der er fundet mangler ved den numeriske implementering af randbetingelser ved berøringslinjer.



# Preface

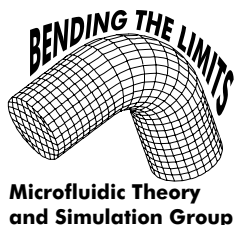
The present master thesis work is submitted in candidacy to the cand. polyt. title at the Technical University of Denmark. The work has been carried out at Mikroelektronik Centret, MIC in the  $\mu$ TAS group under supervision of Henrik Bruus and Goran Goranović from September 2001 to may 2002. It has been a privilege being part of the germ of the new Micro Fluidic Theory and Simulation Group at MIC.

First of all I would like to thank Goran Goranović for the mammoth work he made in the early stages of the thesis period, for his help in defining my project, and for many inspiring discussions in which he gladly shared his many ideas. I am moreover thankful for the enthusiasm my other supervisor Henrik Bruus showed as he joined the project. His ability to grasp problems by their root and analyze them yielded many interesting discussions.

The working atmosphere at MIC has been very nice, the staff has been very helpful and shown interest in the work I was doing. Especially many thanks to the  $\mu$ TAS group under the supervision of Jörg Kutter.

Last, but not least I would like to take the opportunity to thank my three master thesis companions Lennart Bitsch, Anders Brask, and Flemming Rytter Hansen for their "free child" spirit. The atmosphere in the master student room was always relaxed, but certainly also very inspiring. We did bend the limits (see our logo below).

Mads Jakob Jensen  
Lyngby, May 2002





# Contents

<b>List of Symbols</b>	<b>xv</b>
<b>1 Introduction</b>	<b>1</b>
<b>2 Basic Fluid Dynamics</b>	<b>5</b>
2.1 The Continuum Hypothesis . . . . .	5
2.2 Fluids in General . . . . .	6
2.3 Incompressible Fluids . . . . .	7
2.4 Types of Flow . . . . .	8
<b>3 Surface Tension</b>	<b>11</b>
3.1 Energy and Force Descriptions . . . . .	11
3.2 The Young-Laplace Equation . . . . .	13
3.3 Marangoni Effect . . . . .	15
3.4 Experimental Data . . . . .	16
3.5 More Thermodynamics: Gibbs' Free Energy . . . . .	16
3.6 Dimensionless Numbers . . . . .	18
<b>4 Contact Angle</b>	<b>21</b>
4.1 Classical Description . . . . .	21
4.1.1 The Young Equation . . . . .	21
4.1.2 Adhesion . . . . .	24
4.1.3 Wetting and Spreading . . . . .	24
4.2 Molecular Description . . . . .	25
4.3 Experimental Data . . . . .	27
4.4 Dependence of the Contact Angle . . . . .	27
4.4.1 Heterogeneous Surfaces . . . . .	28
4.4.2 Surface Roughness . . . . .	28
4.4.3 Liquid-Surface Interactions . . . . .	29
4.4.4 Dynamic Contact Angle . . . . .	29
4.5 Lubrication vs. Contact Angle . . . . .	32
4.6 Notes on Pressures and Energy . . . . .	34
<b>5 Capillarity and Examples</b>	<b>37</b>
5.1 Capillary Rise . . . . .	37
5.2 Clogging of Contracting Microchannels . . . . .	40
5.3 Non-Cylindrical Tubes . . . . .	44
5.4 Lubrication/Thin-Film Theory . . . . .	46
5.5 Bubble Motion in a Capillary Tubes . . . . .	48

<b>6</b>	<b>Bubbles in General</b>	<b>49</b>
6.1	Solubility of Gas in Liquids . . . . .	49
6.2	Formation of Bubbles . . . . .	50
6.2.1	Pressure Effects (cavitation) . . . . .	50
6.2.2	Other Causes . . . . .	52
<b>7</b>	<b>A Short Review of Microchannels</b>	<b>53</b>
7.1	Dimensions . . . . .	53
7.2	Physical Characteristics . . . . .	54
7.3	Problem Areas . . . . .	55
7.4	Removing Bubbles . . . . .	55
<b>8</b>	<b>Commercial Software</b>	<b>57</b>
8.1	The Flow Module . . . . .	58
8.2	The VOF Module . . . . .	59
8.3	Bugs . . . . .	63
8.4	Test Cases . . . . .	64
8.4.1	2D Couette Flow . . . . .	64
8.4.2	Poiseuille Flow . . . . .	65
8.4.3	2D Static Interface . . . . .	67
<b>9</b>	<b>2D Simulations</b>	<b>71</b>
9.1	Straight Channel . . . . .	71
9.1.1	Wall Resolution and Flow Regimes . . . . .	72
9.1.2	Contact Angle and Flow Regimes . . . . .	75
9.2	Sudden Contraction . . . . .	78
9.3	Tapered Channel . . . . .	78
9.4	Roughness . . . . .	84
9.5	Passive Bubble Trap . . . . .	86
<b>10</b>	<b>3D Simulations</b>	<b>91</b>
10.1	Static Interface Shapes . . . . .	91
10.2	Circular Tube . . . . .	93
<b>11</b>	<b>Conclusion</b>	<b>95</b>
	<b>Bibliography</b>	<b>99</b>
<b>A</b>	<b>Curvature in <math>\mathbb{R}^2</math> and <math>\mathbb{R}^3</math></b>	<b>103</b>
A.1	Curvature in General . . . . .	103
A.2	Interpretation of curvature in $\mathbb{R}^2$ . . . . .	104
A.3	Curvature of a Surface of Revolution . . . . .	105
<b>B</b>	<b>Poiseuille and Couette Flow</b>	<b>107</b>
B.1	Couette Flow . . . . .	107
B.2	Poiseuille Flow . . . . .	108
<b>C</b>	<b>Exact Solution of Capillary Rise</b>	<b>109</b>
C.1	Method . . . . .	109
C.2	Example . . . . .	110
C.3	Source Code . . . . .	111

<b>D</b>	<b>Clogging Program</b>	<b>113</b>
	D.1 Method and Discussion . . . . .	114
	D.2 Source Code . . . . .	116
<b>E</b>	<b>Interface in Tubes of Constant Cross Section</b>	<b>118</b>
<b>F</b>	<b>Temperature Dependence of Surface Tension</b>	<b>122</b>
<b>G</b>	<b>Flow Around a Bubble with Marangoni effects</b>	<b>124</b>
<b>H</b>	<b>Excel Simulation Sheets</b>	<b>126</b>
	H.1 Couette Flow . . . . .	126
	H.2 Poiesuille Flow . . . . .	127
	H.3 2D Static Interface . . . . .	128
	H.4 2D Bubble in Tube . . . . .	130



# List of Figures

2.1	2D shear flow . . . . .	7
3.1	Stretched membrane . . . . .	11
3.2	Soap film in wire frame . . . . .	13
3.3	Differential expansion of interface . . . . .	14
3.4	Marangoni effect . . . . .	15
4.1	Force equilibrium . . . . .	22
4.2	Surface energy minimum . . . . .	23
4.3	Wetting conditions . . . . .	25
4.4	Advancing and receding contact angles . . . . .	27
4.5	Slip length . . . . .	29
4.6	Four regions of interface profile . . . . .	30
4.7	Wetting behavior of moving bubble . . . . .	32
4.8	Sign convention in Young-Laplace . . . . .	34
4.9	Pressure drop definitions . . . . .	34
4.10	Energy argument and "Γ" concept. . . . .	35
5.1	Capillary rise . . . . .	38
5.2	Capillary "fall" . . . . .	38
5.3	Curvature of interface . . . . .	41
5.4	Sudden contraction . . . . .	42
5.5	Tapered channel . . . . .	42
5.6	Relative friction vs. contact angle . . . . .	43
5.7	Cylindrical system of co-ordinates . . . . .	44
5.8	Cross section of square capillary . . . . .	45
6.1	Negative pressure . . . . .	51
6.2	Energy barrier . . . . .	52
7.1	Scanned PMMA channel cross section . . . . .	54
7.2	Cross section of wide microchannel . . . . .	54
8.1	VOF surface reconstruction (PLIC) . . . . .	60
8.2	VOF high wall resolution . . . . .	62
8.3	Couette flow: simulation results . . . . .	65
8.4	Poiseuille flow: grids . . . . .	66
8.5	Poiseuille flow: simulation results . . . . .	66
8.6	Static meniscus: set-up and initial conditions . . . . .	67
8.7	Static meniscus: time evolution of pressure . . . . .	68

8.8	Static meniscus: contour plot of $F$	68
8.9	Static meniscus: capillary wave induced $\Delta P_i$	69
9.1	Straight channel: initial set-up	72
9.2	Straight channel: moving bubble	73
9.3	Straight channel: $h_0$ , $w$ , and $\Delta P_b$	74
9.4	Straight channel: bubble rear	76
9.5	Straight channel: $\Delta P_b$ and $F$ data slices	77
9.6	Straight channel: numerical adhesion	78
9.7	Sudden contraction	79
9.8	Tapered channel: geometry	79
9.9	Tapered channel: four snapshots	81
9.10	Tapered channel: theory and simulation data	81
9.11	Tapered channel: moving into the tapering	82
9.12	Tapered channel: clogging	83
9.13	Roughness: geometry	84
9.14	Roughness: domain and grid	84
9.15	Roughness: theory	85
9.16	Roughness: bubble in rough area	86
9.17	Bubble trap: geometry	87
9.18	Bubble trap: initial condition	87
9.19	Bubble trap: four snapshots	88
9.20	Bubble trap: non-wetting bubble	88
9.21	"Bug leg" structure	89
10.1	Dimensionless curvature relevant to 3D simulation	91
10.2	Static interface in a rectangular 3D tube, $\theta < \theta_c$	92
10.3	Static interface in a rectangular 3D tube, $\theta > \theta_c$	92
10.4	Bubble in 3D cylindrical tube	93
A.1	Differential approach to curvature in $\mathbb{R}^2$	105
A.2	Curvature of a surface of revolution	106
B.1	Couette flow	107
C.1	Dimensions of capillary rise	109
C.2	Meniscus profile at equilibrium	110
D.1	Geometry used in clogging program	113
D.2	Clogging program results	115
D.3	Meniscus deformation around edge	115
D.4	Transition area for $L$	115
E.1	Two cross section of a static interface	118
E.2	Cross section of rectangular tube	119
E.3	Graph of the dimensionless curvature	121
F.1	Box liquid and lid	122
G.1	Simple approximation to flow profile in wetting layer	124





# List of Symbols

Symbol	Description	Unit
$\mathcal{A}$	Area.	$\text{m}^2$
$a$	Tube radius.	$\text{m}$
$b$	Slip length.	$\text{m}$
$Bo$	Bond number.	-
$C$	Specific heat capacity.	$\text{J K}^{-1}$
$C_m$	Dimensionless curvature.	-
$Ca$	Capillary number.	-
$d$	Small tube diameter.	$\text{m}$
$D$	Large tube diameter.	$\text{m}$
$E^s$	Surface energy.	$\text{J m}^{-2}$
$F$	Volume-of-fluid function.	-
$F$	Helmholtz's free energy.	$\text{J}$
$G$	Gibbs' free energy.	$\text{J}$
$G^s$	Surface Gibbs' free energy.	$\text{J m}^{-2}$
$h_0$	Wetting layer thickness.	$\text{m}$
$H$	Mean curvature.	$\text{m}^{-1}$
$H$	Enthalpy.	$\text{J}$
$H^s$	Surface enthalpy.	$\text{J m}^{-2}$
$k$	Wetting coefficient.	-
$k_B = 1.3807 \times 10^{-23}$	The Boltzmann constant.	$\text{J K}^{-1}$
$k_w$	Wave number.	$\text{m}^{-1}$
$Kn$	The Knudsen number.	-
$\ell$	Length or characteristic length.	$\text{m}$
$\ell_b$	Length of bubble.	$\text{m}$
$l$	Length.	$\text{m}$
$l_O$	Offset length.	$\text{m}$
$l_R$	Roughness length.	$\text{m}$
$l_t$	Trap length.	$\text{m}$
$L$	Length or characteristic length.	$\text{m}$
$L_c$	Critical length.	$\text{m}$
$L_{\text{mol}}$	Intermolecular length.	$\text{m}$
$\mathbf{M} = [M_{ij}]$	Matrix (capital letters).	-
$M_{\text{mol}}$	Molar mass.	$\text{kg mol}^{-1}$
$N$	number of particles.	-
$N_A = 6.0221 \times 10^{23}$	Avogadro's number.	$\text{mol}^{-1}$
$N_{St}$	Stokes number.	-

Symbol	Description	Unit
$P$	Pressure.	Pa
$P_0$	Hydrostatic pressure.	Pa
$P_{\text{in}}$	Inlet pressure.	Pa
$P_{\text{out}}$	Outlet pressure.	Pa
$P_L$	Pressure just left of bubble.	Pa
$P_R$	Pressure just right of bubble.	Pa
$\Delta P_b$	Pressure drop over bubble.	Pa
$\Delta P_i$	Pressure drop over interface.	Pa
$Q$	Flow rate.	$\text{m}^3 \text{s}^{-1}$
$r$	Radius.	m
$r$	Radius of curvature.	m
$r$	Intermolecular distance.	m
$r_0$	Collision diameter.	m
$R, R_1, R_2$	Radius of curvature.	m
$Re$	Reynolds number.	-
$S$	Spreading coefficient.	-
$S$	Entropy.	$\text{J K}^{-1}$
$S^s$	Surface entropy.	$\text{J m}^{-2} \text{K}^{-1}$
$t$	Time.	s
$T$	Temperature.	K
$u$	Bubble speed.	$\text{m s}^{-1}$
$\mathbf{u}$	Velocity vector.	$\text{m s}^{-1}$
$U$	Internal energy.	J
$U$	Characteristic velocity.	$\text{m s}^{-1}$
$v$	Fluid average speed.	$\text{m s}^{-1}$
$V$	Volume.	$\text{m}^3$
$V(r)$	Lennard-Jones potential.	J
$w$	Excess speed parameter.	-
$W$	Work.	J m
$W_{sl}$	Work of adhesion.	$\text{J m}^{-2}$
$\mathbf{x}$	Position vector.	m
$\hat{\mathbf{x}}$	Unit vector.	-
$x_{ij}$	Tensor.	-
$\alpha$	Empirical friction surface tension parameter.	$\text{J m}^{-2}$
$\delta$	Characteristic length.	m
$\delta t$	Time step.	s
$\epsilon$	Energy well depth.	J
$\zeta$	Bulk viscosity.	$\text{kg (m s)}^{-1}$
$\theta$	Static contact angle.	-
$\theta_c$	Critical contact angle.	-
$\theta_d$	Dynamic contact angle.	-
$\theta_A$	Advancing contact angle.	-
$\theta_R$	Receding contact angle.	-
$\lambda$	Mean free path of a molecule.	m
$\lambda_b$	Effective slip length.	m
$\lambda_w$	Wavelength.	m
$\mu$	Dynamic viscosity.	$\text{kg (m s)}^{-1}$
$\mu_c$	Chemical potential.	$\text{J mol}^{-1}$

Symbol	Description	Unit
$\nu$	Kinematic viscosity.	$\text{m}^2 \text{s}^{-1}$
$\xi$	Friction angle.	-
$\rho$	Density.	$\text{kg m}^{-3}$
$\sigma = \sigma_{gl}$	Surface tension (gas-liquid).	$\text{J m}^{-2}$
$\sigma_{sl} = \sigma_{ls}$	Interfacial surface tension (liquid-solid).	$\text{J m}^{-2}$
$\sigma_{sg} = \sigma_{gs}$	Interfacial surface tension (gas-solid).	$\text{J m}^{-2}$
$\sigma_{ij}$	Stress tensor.	Pa
$\tau$	characteristic time.	s
$\tau_{xy}$	Shear stress in $y$ direction on plane with normal in $x$ .	$\text{N m}^{-2}$
$\phi_{ij}$	Van der Waals attractive potential.	J
$\omega$	Angular velocity.	$\text{s}^{-1}$
$\Gamma$	Pressure gradient.	$\text{Pa m}^{-1}$
$\Gamma_s$	Surface excess parameter.	$\text{mol kg}^{-1} \text{m}^{-2}$
$\Delta_c$	Capillary length.	m
$\Lambda$	Interface length or area.	m or $\text{m}^2$
$\nabla_s$	Surface gradient.	$\text{m}^{-1}$
$\nabla$	Nabla or del operator.	$\text{m}^{-1}$



# Chapter 1

## Introduction

In the last decades great innovations in the microfluidic area have been made. Microfluidic is hydrodynamic at micrometer scale. A great amount of work has been put into the development of different components such as micropumps, microvalves, mixing chambers, and chemical reaction chambers. An integration of these components makes up the so-called "lab-on-a-chip" concept which is one of the driving ideas behind the research. The miniaturization process is expected to revolutionize the chemical, biochemical, and medical industry. Complete chemical and biological analyzes will be carried out in the lab-on-a-chip systems, also called Micro Total Analysis Systems ( $\mu$ TAS).

The microfluidic systems will most certainly make paramount changes in the way laboratories work: smaller, cheaper, and fully automated devices will perform faster and more accurate measurements than today. The application prospects are wide. From easy environmental monitoring to medical monitoring of patients in geographically remote areas. The microfluidic field is vast, in full expansion and the subject of increasing investments from industry. The development and fabrication of integrated microfluidic devices are a true multidisciplinary field: process specialists, chemists, biologists, material scientists, surface physics specialists, and microfluidic specialists all play key roles in the process.

In the history of microfluidics bubbles have often been rather a handicap than an asset. The interfacial surface tension effects, associated with the presence of bubbles, introduce a unique type of force that scales directly to length. At the present typical micrometer scale and operating flow regime the surface tension forces dominate most other forces, such as gravity, pressure, and viscous drag. As the surface tension effects are directly related to lengths the actual geometry of devices is cardinal. Gas bubbles may get stuck in sensitive places and clog the flow completely eliminating the functionality of the microdevice. In the recent years the design of microfluidic devices making use of surface tension effects has been attempted, [22, 49, 50].

Microfluidic devices are already at a stage where a further efficient development requires the use of simulation capabilities. Advances in computational fluid dynamics (CFD) enable a better and less expensive design process. An

effort in the CFD field should nevertheless be made together with a thorough theoretical study of the given subject. In relation to the bubble phenomenon great progress in the numerical handling of the interface has been made in the last decade. The increased computational power of personal computers and the development of commercial CFD software provide research facilities with easy access to good simulation capabilities.

The bubble phenomenon is in this thesis studied within the philosophy of a joined computational and theoretical investigation. A thorough analysis of classical theory for surface tension and multi-phase flows, including the Young-Laplace equation and the contact angle phenomenon, is carried out. Newer microscopic theories are also introduced. The manifestation of the interfacial surface tension related scale effects "capillarity" are studied and exemplified. The theory is applied to two specific geometries of contracting microchannels. In this context a MATLAB program is implemented. After the theoretical investigation the capabilities of the commercial CFD software CFD-ACE+ are investigated and several practical examples are studied. The CFD-ACE+ package utilizes the so-called volume-of-fluid (VOF) method to handle the free surface interface boundary. The VOF method has undergone a drastic evolution since its initial implementation in the late seventies and is today one of the foremost utilized techniques to handle free surfaces, Rider and Kothe [43]. Both two and three-dimensional geometries are studied, in both cases the produced data is compared with theory and discussed in detail. The specific report structure is as follows:

- **Basic Fluid Dynamics (Chap. 2)**

A discussion of the continuum approximation and presentation of the governing equations of fluid dynamics. The aspects of microfluidics are taken into account.

- **Surface Tension (Chap. 3)**

The surface tension phenomenon is presented in great detail. Both an energy and a force description are presented and the central Young-Laplace equation is derived.

- **Contact Angle (Chap. 4)**

The contact angle at gas-liquid-solid contact line is presented. Both a classical and a molecular description are given. The dependence of the contact angle with respect to several parameters is further investigated.

- **Capillarity and Examples (Chap. 5)**

The phenomena related to surface tension and contact angle: capillarity are here presented. The aiming is to describe the clogging of microchannels by bubbles and movement of bubbles in microchannels. The clogging pressure concept is introduced.

- **Bubbles in General (Chap. 6)**

This chapter introduces some general notions about the formation of bubbles. Emphasis is put on pressure effects.

- **A Short Review of Microchannels (Chap. 7)**

The purpose of chapter 7 is to relate the presented physical theories to

actual microfluidic devices. Scales and flow regimes are presented in view of the simulations made in chapter 9 and 10.

- **Commercial Software (Chap. 8)**

The commercial simulation software package CFD-ACE+ is presented and tested on three test cases. Special focus is put on the properties of the free surface handling VOF-method.

- **2D and 3D Simulations (Chap. 9 and 10)**

Simulations of two-phase flows in both 2D and 3D geometries are finally made. The results are compared with theory and discussed thoroughly. An innovative method to handle the bubble problem is proposed and analyzed: the so-called passive bubble trap.

Through the work with the thesis emphasis was put on the close relation between theoretical physics and simulations. The theoretical study is motivated by the later CFD application and the intent to investigate the capabilities of the CFD-ACE+ package. Simulation results should always be scrutinized in detail. The building up of knowledge enabling an analysis of a microfluidic system eventually based on certain global design rules is the final goal. This thesis presents some of the problematic geometries, but also a novel bubble trap device designed according to a few simple, but powerful principles.



# Chapter 2

## Basic Fluid Dynamics

To initiate the physics discussions of the next chapters some basic fluid dynamics are first shortly discussed. The following discussion is quite general, however, certain specifics related to microfluidics are detailed.

The continuum hypothesis is firstly discussed. Secondly, the governing equations for a general Newtonian liquid are presented. The more relevant case of incompressible fluids is then presented and at last different types of flow are discussed in relation to the Reynolds number  $Re$ .

### 2.1 The Continuum Hypothesis

In this thesis all fluids discussed are Newtonian and are generally treated as continuous isotropic matter (mean molecular fields). The continuum description could however be questioned because of the small length scales present in microfluidics.

A way of defining deviations from the continuum description is through the Knudsen number

$$Kn = \frac{\lambda}{\ell}, \quad (2.1)$$

where  $\lambda$  is the mean-free-path of the molecules and  $\ell$  is a characteristic length scale.  $\ell$  should be chosen to include gradients in the velocity field. For liquids  $\lambda$  is approximately the intermolecular length  $L_{\text{mol}}$  (bond length). The volume occupied by one molecule  $L_{\text{mol}}^3$  is easily approximated, yielding

$$L_{\text{mol}} = \left( \frac{M_{\text{mol}}}{\rho N_A} \right)^{1/3}, \quad (2.2)$$

where  $\rho$  is the density,  $M_{\text{mol}}$  the molar mass, and  $N_A$  is Avogadro's number. For water  $\lambda = L_{\text{mol}} \approx 0.31$  nm. The Knudsen number identifies the continuum regimes and the governing equations.<sup>1</sup>

---

<sup>1</sup>For  $0 < Kn < 0.01$  the continuum approximation is applicable and the Navier-Stokes equation usable, this regime is generally in use in microfluidic flows. For  $0.01 < Kn < 0.1$  the Navier-Stokes equation is still applicable however with use of so-called slip conditions to account for microscopic phenomenon at solid boundaries.

A more intuitive way of justifying the use of the continuum approximation is through a precision criterion. At sufficiently high precision fluids are never continuous. The concept of a continuous velocity field does, e.g., only makes sense for small changes in the center of mass, of a small characteristic volume, due to random fluctuations in velocities. Another example could be to determine the mass density to a certain relative precision  $r$ .

- **Example**

Determining the mass density  $\rho = mN/V$  to the relative precision  $r$ , with  $N$  the number of molecules of mass  $m$  in a small volume  $V$ . There are only fluctuations in the relative number of molecules  $\Delta N$  due to random walk which is typically  $\Delta N \approx \sqrt{N}$ . For  $r = 1\%$  the requirement  $\Delta N/N < r$  yields  $N > 1/r^2 = 10^4$ . The given volume hence needing dimensions  $\ell > 22L_{\text{mol}}$ . For the case of water  $\ell > 7\text{ nm}$  which is a factor  $10^3$  smaller than the geometric dimensions of the microfluidic systems analyzed in this thesis.

Liquid-gas interfaces are of prime interest in the present thesis. Because a liquid-gas interface only has a thickness comparable to the molecular scale  $L_{\text{mol}}$  it is reasonable to describe the involved fluids (liquid and gas) as continuums, Evans [30]. The interface is characterized through a discontinues change from one isotropic continuum to another. In certain cases however the length scales involved, in the physical descriptions, compromise the continuum hypothesis. These are in the following chapters clearly mentioned. This is, e.g., the case in Sec. 4.4 where small length scales are considered near moving triple points (gas-liquid-solid contact lines).

## 2.2 Fluids in General

The complete system of equations for the motion of isotropic Newtonian fluids, both liquids and gases, is presented in the following. Each equation is stated and commented individually.

### Momentum

The most general momentum equation covering all aspects of fluid dynamics is the Navier-Stokes equation. It is essentially obtained by applying Newton's second law to an infinitesimal fluid element

$$\rho \frac{d\mathbf{u}(\mathbf{x}(t), t)}{dt} = \sum \text{volume and surface forces} \quad (2.3)$$

yielding

$$\rho \left( \frac{\partial \mathbf{u}}{\partial t} + (\mathbf{u} \cdot \nabla) \mathbf{u} \right) = -\nabla P + \mu \nabla^2 \mathbf{u} + \frac{1}{3} \mu \nabla (\nabla \cdot \mathbf{u}) + \mathbf{f}. \quad (2.4)$$

that is conservation of momentum. Where  $\mathbf{u} = (u, v, w)$  is the velocity vector,  $P$  the dynamic pressure,  $\rho$  the density,  $\mu$  the dynamic viscosity, and  $\mathbf{f}$  a volume force (body force).

### Continuity

The requirement of global conservation of mass reduces locally, by the use of Gauss' theorem, to

$$\frac{\partial \rho}{\partial t} + \nabla \cdot (\rho \mathbf{u}) = 0, \quad (2.5)$$

which is the continuity equation, i.e., the local continuity equation for mass.

### Dynamic Pressure and Equation of State

In the Navier-Stokes equation Eq. (2.4) the pressure  $P$  is the so-called dynamic pressure. It originates from the specific nature of the stress tensor. In Newtonian fluids it reduces to

$$P = P_0 + \zeta \nabla \cdot \mathbf{u}. \quad (2.6)$$

Where  $P_0$  is the hydrostatic pressure in the fluid for  $\mathbf{u} = \mathbf{0}$  and  $\zeta$  is the bulk viscosity.  $\zeta$  is analogue to the bulk modulus for elastic materials and is a measure of incompressibility, Lautrup [12]. To complete Eq. (2.6) an equation of state

$$P_0 = P_0(\rho), \quad (2.7)$$

relating the equilibrium pressure  $P_0$  to the the fluid motion, is necessary.

### Constitutive Equation for Viscosity

Fluids with a linear relationship between stress and rate of strain (deformation) are called Newtonian fluids. The specific relation is expressed in a constitutive equation specifying the material properties of the liquid through the stress-strain relation: Newtonian fluids give in to shear stress and flow in such a way that shear is eliminated in equilibrium.

- **Example**

In the 2D shear flow illustrated in Fig. 2.1, the relation between stress and strain is called Newton's formula

$$\tau_{yx} = \mu \left( \frac{\partial u}{\partial y} \right). \quad (2.8)$$

Where  $\tau_{yx}$  is the stress in the  $x$ -direction on a plane with normal in the  $y$ -direction. The coefficient of proportionality  $\mu$  is the dynamic viscosity. Maxwell interpreted Eq. (2.8) kinematically as a vertical momentum interchange.

At room temperature the linear nature of the Newtonian fluids is a very good approximation for, e.g., pure water. The linear relation breaks down for some suspensions and polymer solutions. The reason for non-Newtonian behavior is found on a microscopic level, Probstein [2]. Further details on the flow equations are found in several very good books: Fung [45], Lautrup [12] or Fredsøe [4].

## 2.3 Incompressible Fluids

The above set of governing equations are very general. However, in most cases assuming the fluid to be incompressible is a good approximation. In an incompressible fluid the density  $\rho_0$  is constant. This fact reduces the governing

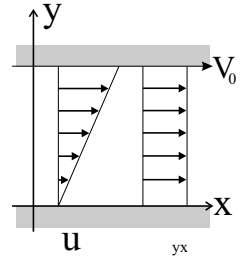


Figure 2.1: 2D shear flow: upper plate is moving at speed  $V_0$  and the lower is stationary.

equations to

$$\rho_0 \left( \frac{\partial \mathbf{u}}{\partial t} + (\mathbf{u} \cdot \nabla) \mathbf{u} \right) = -\nabla P_0 + \mu \nabla^2 \mathbf{u} + \mathbf{f} \quad (2.9a)$$

$$\nabla \cdot \mathbf{u} = 0. \quad (2.9b)$$

The first equation being the momentum equation and the second the continuity equation. The constitutive equation, in tensor notation, simplifies likewise to

$$\tau_{ij} = \mu(\nabla_i u_j + \nabla_j u_i). \quad (2.10)$$

Which is a general form of Newton's formula. The stress tensor  $\sigma_{ij}$  being

$$\sigma_{ij} = -P_0 \delta_{ij} + \tau_{ij} = -P_0 \delta_{ij} + \mu(\nabla_i u_j + \nabla_j u_i). \quad (2.11)$$

## 2.4 Types of Flow

In the Navier-Stokes equation for incompressible fluids Eq. (2.9a) the different terms are the instantaneous acceleration  $\partial \mathbf{u} / \partial t$ , the convective or inertia term  $(\mathbf{u} \cdot \nabla) \mathbf{u}$ , the pressure gradient  $-\nabla P_0$ , the shear viscosity term  $\mu \nabla^2 \mathbf{u}$ , and the body force  $\mathbf{f}$ .<sup>2</sup> The most interesting flow patterns arise because of the interplay between inertia and viscosity. The first tries to continue a fluid movement when initiated and the second acts as a break. Though in many cases only one of the terms is of importance. The ratio between the inertia and viscosity is given by the Reynolds number

$$Re = \frac{\text{inertia forces}}{\text{viscous forces}} \approx \frac{|\rho(\mathbf{u} \cdot \nabla) \mathbf{u}|}{|\mu \nabla^2 \mathbf{u}|} \approx \frac{\rho U^2 / \delta}{\mu U / \delta^2} = \frac{\rho U \delta}{\mu} \quad (2.12)$$

where  $U$  is the characteristic velocity change over the the characteristic length scale  $\delta$ , normally determined by geometry.

At high Reynolds numbers ( $Re \gg 1$ ) inertia is dominant and Eq. (2.9a) effectively reduces to Euler's equation describing ideal flow (non-viscous). At low Reynolds numbers ( $Re \ll 1$ ) Eq. (2.9a) reduces to the creeping flow equation.

The Reynolds number also characterizes whether a flow is turbulent or laminar. If the viscous forces are of importance the flow is popularly said to be more sluggish, whereas it is more lively for negligible viscous effects. For a given geometry a stability analysis will reveal at which Reynolds numbers the flow pattern varies. Two flows having the same Reynolds number are said to be dynamically equivalent as they exhibit the same stability (laminar or turbulent).<sup>3</sup>

<sup>2</sup>The form of the instantaneous acceleration and inertia terms result from the eulerian viewpoint, i.e., fixed in space and not following a liquid element. The terms follow naturally from a mathematical point of view. However, the inertia term has a physical interpretation. It corresponds to the inertial force exerted by surrounding fluid on the given observed fluid element.

<sup>3</sup>A rearrangement of the governing equations yield an equation for transport of rotation/vorticity. By use of perturbation theory an energy equation for a perturbation in the rotation can be derived (time variation, production, and energy loss due to viscous work). The Reynolds number appears as determining the amount of energy loss, i.e., if the perturbation will decay.

Microfluidic flows are laminar, Gravesen *et al.* [48] and Chap. 7. Creeping flow regime may also appear as the Reynolds numbers may be very small. The creeping flow equation is

$$\rho_0 \frac{\partial \mathbf{u}}{\partial t} = -\nabla P_0 + \mu \nabla^2 \mathbf{u}. \quad (2.13)$$

where the body forces have been neglected. The exact nature of the flow is nevertheless geometrically dependent.



## Chapter 3

# Surface Tension

Surface tension is the energy per area of an interface between two phases. It gives rise to many physical phenomena and fascinating behaviors of fluids. Many of these are every day occurrences: the formation of droplets, the curvature of the liquid surface in a glass of water, and the formation of beautiful soap films. The physics and chemistry behind the phenomena are not understood completely. This does not mean the phenomena are not applied - they are in many cases as, e.g., in the well known ink-jet printers.

In the following first section two descriptions of the surface tension,  $\sigma$ , are presented<sup>1</sup>. The assumptions and physical arguments are firstly presented through a force description and secondly through an energy description. In the second section, an important consequence of the existence of surface tension, namely, the curvature of interfaces, is presented and the essential Young-Laplace equation is derived. The third section treats the effect of surface tension gradients the so-called Marangoni effect. Then, in the fourth section surface tension data is briefly presented. The fifth section introduces an alternative energy consideration through the Gibbs' free energy. Finally the last section introduce some dimensionless numbers used through out the thesis.

### 3.1 Energy and Force Descriptions

#### Inter Molecular Forces

At a liquid-gas interface the molecules in the liquid are bound by the van der Waals forces, where the gas molecules are relatively free to move. At the liquid surface the molecules are mainly attracted inward and to the sides. Of course some liquid molecules evaporate, but it is a small fraction. Mostly there is no outward attraction to balance the inward force. The surface molecules are thus attracted inward normal to the surface and the surface tends to curve. This results in the surface acting like a stretched membrane, with a tension  $\sigma = \mathcal{F}/\ell$  along the edge, i.e., a force per unit length tending to decrease the surface area, Fig 3.1.

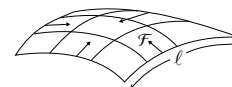


Figure 3.1: A force  $\mathcal{F}$  acting on the border length  $\ell$  of a stretched membrane.

<sup>1</sup>In European literature surface tension is labelled  $\sigma$  where as in American  $\gamma$  is often used.

### Energy and Work

An energy description of the surface tension originates from the fact that the molecules at the interface (liquid-gas) are attracted by less neighboring molecules than those in the interior of the liquid. The attraction energy at the interface must hence be less than that of an interior molecule. The molecules at the surface thus have the highest energy. Work is required to form surface area that is to move molecules from the interior to the surface interface<sup>2</sup>. As the total free energy of the system minimizes, the surface area tends to minimize. This fact leads to the other definition of the surface tension, namely, that  $\sigma$  is the energy per unit area that tends to minimize area (contract the surface) hence

$$\sigma = \left( \frac{\partial F}{\partial \mathcal{A}} \right)_{T,V}, \quad (3.1)$$

for constant temperature  $T$  and volume  $V$ .  $\mathcal{A}$  is the surface area and  $F$  is the Helmholtz's free energy also known as the work function

$$F = F(T, V, N) = U - TS \quad (3.2)$$

defined in terms of the total internal energy  $U$ , the temperature  $T$ , and the entropy  $S$ . The independent variables of  $F$  are temperature  $T$ , volume  $V$ , and number of particles  $N$ .<sup>3</sup> The  $TS$  term corresponds to the energy not available to achieve uniform motion in the surroundings, i.e., the entropical loss.  $F$  is hence the energy available for conversion into work.

For constant temperature and volume Eq. (3.1) simply states that for a given surface tension  $\sigma$ ,  $dF$  will decrease with decreasing  $d\mathcal{A}$ . The surface free energy will tend to a minimum. The surface tension is thus the Helmholtz free energy per area, provided the viscosity of the liquid is not too high (Probstein Ch. 10 [2]).<sup>4</sup> From the definition, Eq. (3.2), it follows that surface tension decreases with increasing temperature, i.e.,

$$\frac{\partial \sigma}{\partial T} = \left( \frac{\partial^2 F}{\partial T \partial \mathcal{A}} \right)_V < 0. \quad (3.3)$$

A thought experiment justifying the above expression is presented in Appendix F. See the later Sec. 2.6 for further discussion of the surface tension in regard to thermodynamical potentials.

### Example

To illustrate the different approaches, but also the agreement of the two previous descriptions consider the following instructive example.

In the previous paragraphs  $\sigma$  is treated as an energy per unit area and as a force per unit length. Consider a soap film stretched over a wire frame with a movable end, see Fig. (3.2). When moving the end  $dx$  in the direction of the

<sup>2</sup>The molecules in the bulk of the liquid are lying in a deeper potential well than those at the interface.

<sup>3</sup>In the following it is given that the number of particles  $N$  is held constant. The small number evaporating from the surface is neglected.

<sup>4</sup>In a liquid with high viscosity the molecules have difficulty moving around. They have a higher activation energy, that is, a smaller probability to move around. A considerable fraction of the internal free energy available for work is hence associated with movement of molecules within the bulk of the liquid. The surface tension cannot minimize the surface area.

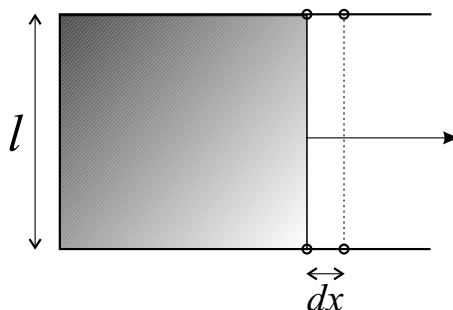


Figure 3.2: Experimental set-up: a soap film in a wire frame where one end can move. Surface tension may be illustrated as work and as a force.

arrow experiments show that a force is acting in the opposite direction. The work  $W$  made by extending the membrane  $dx$  is

$$W = \sigma l dx. \quad (3.4)$$

The work could equally have been expressed as

$$W = \sigma d\mathcal{A}, \quad \text{with} \quad d\mathcal{A} = l dx. \quad (3.5)$$

In Eq. (3.4)  $\sigma$  is given as a force per length ( $[\sigma] = \text{N m}^{-1} = \text{kg s}^{-2}$ ) whereas it in Eq. (3.5) is an energy per area ( $[\sigma] = \text{J m}^{-2} = \text{kg s}^{-2}$ ).

The present example is meant to illustrate how both descriptions yield an identical solution. The energy description is the more describing and useful one, as one of the key aspects of interfaces or surfaces is to minimize surface energy hence area. This naturally leads to the next discussion of the Young-Laplace equation.

## 3.2 The Young-Laplace Equation

Because of the existence of surface tension, an interface will have a tendency to curve. The curvature results from the minimization of area driven by the minimization of free surface energy. This curvature results in a pressure difference across the interface  $\Delta P_i$  (the highest pressure on the concave side). An expression for the pressure difference is found by considering the work (pressure-volume) needed to expand a curved surface. Notice that a surface in  $\mathbb{R}^3$  is characterized by two principal curvatures (Millman and Parker [5] and Appendix A) or radii of curvature  $R_1$  and  $R_2$ . For a sphere the radii are equal,  $R_1 = R_2$ .

In the following a small test section of an arbitrary surface depicted in Fig. 3.3 is utilized to find an expression for the mentioned pressure difference. The curvatures are assumed locally constant.

When displacing the surface outwards by  $dz$  the resulting change in surface area is:

$$d\mathcal{A} = (x + dx)(y + dy) - xy = xdy + ydx.$$

The corresponding work made in stretching the surface with surface tension  $\sigma$  is hence

$$dW = \sigma d\mathcal{A} = \sigma(xdy + ydx). \quad (3.6)$$

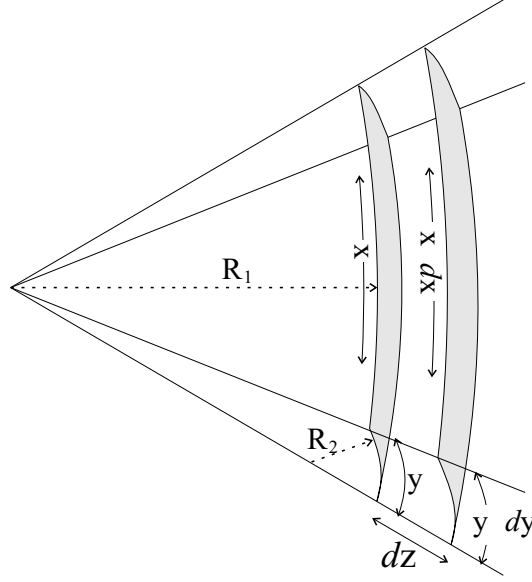


Figure 3.3: Differential expansion of an interface with locally constant curvatures  $1/R_1$  and  $1/R_2$ .

The work is also delivered as force times distance: counteracting a pressure difference  $\Delta P_i$  across the surface area  $xy$  moved the distance  $dz$  hence

$$dW = \Delta P_i x y dz. \quad (3.7)$$

A simple geometrical consideration on similar triangles yields

$$\frac{x + dx}{R_1 + dz} = \frac{x}{R_1} \Rightarrow dx = \frac{x}{R_1} dz \quad (3.8)$$

$$\frac{y + dy}{R_2 + dz} = \frac{y}{R_2} \Rightarrow dy = \frac{y}{R_2} dz$$

For the system to be in equilibrium the work made by the surface tension, Eq. (3.6), and the work made by the pressure, Eq. (3.7), must be equal. Equating and using the expressions Eq. (3.8) result in the Young-Laplace equation

$$\Delta P_i = \sigma \left( \frac{1}{R_1} + \frac{1}{R_2} \right) = \sigma 2H = \sigma (-\nabla \cdot \hat{\mathbf{n}}). \quad (3.9)$$

Where  $H$  is the mean curvature see Eq. (A.5) in Appendix A. The last of the three identical formulations defines the curvature through the divergence the surface unit normal:  $-\nabla \cdot \hat{\mathbf{n}}$ .

The above equation is essential in describing all capillary and especially small bubble phenomena.  $\Delta P_i$  is the pressure difference required to sustain the curvature resulting from the surface tension.  $\Delta P_i$  is defined positive and is thus the pressure at the convex side minus the pressure at the concave. An extended discussion is given Sec. 4.6. If no external forces are present a static

interface has the same mean curvature at every point. If this was not the case different pressures would appear and deform the interface. In zero gravity a drop is spherical whereas it is deformed by gravity on earth.

On a plane surface, e.g., a large puddle, the pressure difference is obviously zero as  $R_1 \rightarrow \infty$  and  $R_2 \rightarrow \infty$ .<sup>5</sup> Note that for large scale phenomena, such as ocean waves  $\Delta P_i$  resulting from the surface tension is negligible as  $R_1$  and  $R_2$  tend to infinity. Conversely  $\Delta P_i$  becomes very important at small scales as  $R_1$  and  $R_2$  may tend to zero. These length scale effects are important in microfluidics and are amply discussed in the rest of the thesis.

### 3.3 Marangoni Effect

The surface tension is not in general a spatially constant physical quantity on, say, a liquid-gas interface. Spatial variations in the surface tension may exist and result in additional shear stresses, that is, tractive forces on the adjoint bulk liquid. This gives rise to fluid motions in the bulk liquid. These motions induced by gradients in the surface tension are called Marangoni effects.

The spatial variations of  $\sigma$  may arise from variations in different quantities such as the surface temperature, concentrations of surface active additives (surfactants), or in electric charge of surface potentials, Probstein [2]. An important effect of surfactants is that they may have strong effects on the pressure drop necessary to push a bubble through a fine capillary. This is further commented in Chap. 5. The influence of electric fields on the surface tension is, e.g., used in pumping devices, Matsumoto and Colgate [22].

As mentioned the surface tension variation along an interface creates a tangential force per unit area,  $f_s$ , a tangential stress or shear stress,

$$f_s = \nabla_s \sigma \quad (3.10)$$

where  $\nabla_s$  is the surface gradient. Note that the positive sign on  $\nabla_s \sigma$  indicates that the liquid on/in the interface will tend to move from areas with low surface tension to areas with high surface tension. On Fig. 3.4 areas of high and low surface tension are depicted. As the surface tension represents the tendency to reduce area there must be a net surface tangential stress from the low to the high surface tension regions.

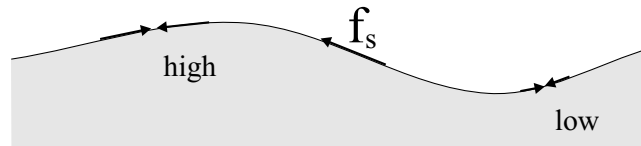


Figure 3.4: Areas of low and high surface tension are illustrated by small and large arrows, respectively. They induce a net tangential stress, the Marangoni effect.

Newton's third law requires that stress vectors are continuous across boundaries. Both normal and tangential components. Surface tension however gives

<sup>5</sup>The pressure drop is zero as  $H = 0$ , this is the case as a plane is a special minimal surface. A minimal surface is a surface having  $H = 0$ . It also has the property of locally minimizing area, for further details see Osserman [19].

rise to discontinuous jumps across an interface: (1) The Young-Laplace equation describes the jump in pressure (normal stress), and (2) the Marangoni effects may give rise to jumps in the shear stress (tangential stress) and hence create forces in the bulk liquids, Lautrup [12]. A simple example regarding the tangential stress is given in Appendix G.

### 3.4 Experimental Data

Data for the liquid-vapor surface tension,  $\sigma$ , at different temperatures is presented in Table. 3.1.

Liquid	$T/^\circ\text{C}$	$\sigma/(\text{mJ m}^{-2})$
Water	20	72.94
	21.5	72.75
	25	72.13
<i>Organics:</i>		
Benzene	20	28.88
Methanol	20	22.50
Blood		55.5-61.2
<i>Metals:</i>		
Hg	20	486.5
	25	485.5
	30	484.5

Table 3.1: Values of liquid-vapor interface surface tensions (Adamson and Gast [1]).  $\sigma$  for water at  $20^\circ\text{C}$  is given as  $72.88 \text{ mJ m}^{-2}$  in Probstein [2], hence variations exist in literature.

### 3.5 More Thermodynamics: Gibbs' Free Energy

In the following some thermodynamical considerations regarding the surface tension are made. They lead to an expression for the surface energy, the specific heat, and some semi empirical expressions. The surface tension has previously been defined in terms of the thermodynamical potential the Helmholtz free energy  $F$  as

$$\sigma = \left( \frac{\partial F}{\partial \mathcal{A}} \right)_{T,V}. \quad (3.11)$$

The differential form of the Helmholtz free energy is

$$dF = -SdT - PdV. \quad (3.12)$$

In that context  $F$  is constant for constant volume  $V$  and temperature  $T$ .  $F \equiv F(V,T)$  so the useful potential to use when discussing processes at constant volume and temperature.<sup>6</sup>

<sup>6</sup>Formally  $F \equiv F(V,T,N)$  and  $G \equiv G(P,T,N)$  where  $N$  is the number of particles. So that  $dF = -SdT - PdV + \mu_c dN$  where  $\mu_c$  is the chemical potential. The thermodynamical potentials may also be given per mole so that  $dN = 0$ .

Another way of defining the surface tension is in terms of the Gibbs' free energy  $G \equiv G(P, T)$  defined as

$$G = F + PV = H - TS \quad (3.13)$$

where  $H = U + PV$  is the enthalpy. In differential form  $G$  is given as follows (using total derivation),

$$dG = dH - TdS - SdT = VdP - SdT \quad (3.14)$$

as  $dU = TdS - PdV$  (the first law of thermodynamics). For constant pressure and temperature Eq. (3.13) yields

$$dG = 0. \quad (3.15)$$

In terms of work the Gibbs free energy is the value of the maximal amount of non-expansion work<sup>7</sup> that can be made in a system of constant pressure and temperature. Take, e.g., a drop of liquid with a given volume and temperature. The surface tension will deform the surface to minimize the free surface energy, i.e., a non-expansion work. In this regard the surface tension is hence also defined as

$$G^s = \sigma = \left( \frac{\partial G}{\partial \mathcal{A}} \right)_{T,P}. \quad (3.16)$$

the suffix  $s$  designates surface quantities. For constant volume ( $dV = 0$ ) the surface entropy is readily found from Eq. (3.14) and Eq. (3.16) as

$$\left( \frac{\partial G^s}{\partial T} \right)_P = \frac{\partial \sigma}{\partial T} = -S^s. \quad (3.17)$$

Finally the total surface enthalpy per surface area is found from Eq. (3.13) as

$$H^s = G^s + TS^s, \quad (3.18)$$

often (Adamson and Gast [1], and Both and Christiansen [8]) the surface enthalpy  $H^s$  is a good approximation for the total surface energy  $E^s$  hence using Eq. (3.16) and Eq. (3.17) yields<sup>8</sup>

$$E^s \simeq H^s = \sigma - T \frac{\partial \sigma}{\partial T}. \quad (3.19)$$

The total surface energy  $E^s$  is in general greater than the Gibbs' free surface energy. Moreover it is the quantity which is easiest to relate to microscopic models. From the total surface energy the surface specific heat capacity  $C^s$  readily follows

$$C^s = \frac{\partial E^s}{\partial T} = -T \frac{\partial^2 \sigma}{\partial T^2}, \quad (3.20)$$

$C_P^s$  and  $C_V^s$  are rarely distinguished as follows from Eq. (3.19).

From Eq. (3.17) it follows that the surface tension decreases with increasing temperature (as  $S \geq 0$ ). Experiments show that  $\sigma$  decreases in a nearly linear

<sup>7</sup>Expansion work is the pressure volume work:  $dW_{exp} = -PdV$

<sup>8</sup>As  $H^s = E^s + PV$  at the surface with the volume approximately zero it is reasonable to set  $H^s = E^s$ .

manner with increasing  $T$  until a critical temperature  $T_c$  where it vanishes, Adamson and Gast [1], and Probstein [2]. An algebraic relation originating from van der Waals in 1894 was further developed and states that

$$\sigma = \sigma_0 \left(1 - \frac{T}{T_c}\right)^n \quad (3.21)$$

where  $n$  is about  $\frac{11}{9}$  for organic materials and near one for metals,  $\sigma_0$  is a material parameter.

### 3.6 Dimensionless Numbers

Special dimensionless numbers related to the effects of surface tension (capillarity) are here introduced. These numbers relate surface tension, viscosity, and gravitation to specific characteristic dimension. They are listed below:

- A measure of the surface tension force to the gravitational force is given by the Bond number

$$Bo = \frac{\text{gravitational force}}{\text{surface tension force}} = \frac{\rho g L^2}{\sigma} \quad (3.22)$$

where  $L$  is the characteristic length scale. The characteristic length may, for example, be a meniscus<sup>9</sup> height (see the later capillary rise example in Chap. 5). When the Bond number is large the surface pressure effects (due to surface curvature given by the Young-Laplace equation) may be neglected in the liquid at rest.

- A length scale for surface tension governed phenomenon is derived from the Bond number Eq. (3.22). Having

$$L \ll \left(\frac{\sigma}{\rho g}\right)^{\frac{1}{2}} \equiv \Delta_c \Rightarrow Bo \ll 1 \quad (3.23)$$

where  $\Delta_c$  is the so-called capillary length. For  $L = \Delta_c$  the Bond number is 1.  $\Delta_c$  provides a measure (length scale) for when phenomena are either controlled by gravity ( $> \Delta_c$ ) or surface tension  $< \Delta_c$ .

- When a system has an imposed characteristic velocity, say,  $U$ , the so-called capillary number is introduced. The number is the ratio of viscous forces to surface tension forces and is defined as

$$Ca = \frac{\text{viscous forces}}{\text{surface tension forces}} = \frac{\mu U}{\sigma} \quad (3.24)$$

where  $\mu = \rho\nu$  is the dynamic viscosity. Having Newton's formula  $\tau = \mu(\frac{\partial u}{\partial y} + \frac{\partial v}{\partial x})$  in mind (Fredsoe [4]) gives some insight into the capillary number:  $\tau \approx F/L^2 \sim \mu U/L$  and  $\sigma \approx F/L$  hence  $Ca \approx F_{viscosity}/F_\sigma$ .

<sup>9</sup>A meniscus is a concavo-convex lens-like shape as, e.g., the curved upper surface of a column of liquid.

- Taking the ratio between the capillary and the Bond number yields the Stokes number. It is a measure of the viscous force to gravity force and is defined as

$$N_{St} = \frac{\text{viscous forces}}{\text{gravitational force}} = \frac{\mu U}{\rho g L^2} = \frac{\nu U}{g L^2}. \quad (3.25)$$

- Finally the well known Reynolds number  $Re$  relating momentum or inertial forces ( $\approx \rho U^2/\delta$ ) to viscous forces ( $\approx \mu U/\delta^2$ ) is given as

$$Re = \frac{\text{momentum forces}}{\text{viscous forces}} = \frac{U\delta}{\nu} \quad (3.26)$$

where  $\delta$  is a characteristic length on which  $U$  varies, normally determined by geometry. Note that low Reynolds numbers in a flow imply that inertial forces are negligible and the flow is creeping. High Reynolds numbers predict that inertia dominates; the flow is in an ideal fluid regime. The Reynolds number and types of flow are readily discussed in Chap. 2.

The dimensionless numbers defined above are going to be used in characterizing contact angle phenomenon as well as the flow in the following chapters. In the later Chap. 7 some specific dimensions for microfluidics are used to characterize the regimes of the numbers.



## Chapter 4

# Contact Angle

At the line of contact between three phases an angle between two of the phases may be defined. The angle emerge from a minimum configuration of interfacial energies. In the following the angle between a liquid and a solid at a gas-liquid-solid contact is named the contact angle  $\theta$ . The contact angle of a liquid on a solid surface is an important concept: it is an essential parameter in numerical models and generally it gives rise to capillarity<sup>1</sup>.

This chapter will thoroughly describe many aspects of the contact angle phenomenon. The first section in this chapter starts out with a classical macroscopic thermodynamical description of the contact angle phenomenon. A microscopic description is then presented. In the third section contact angle data is listed. The fourth section deals with the dependence of the contact angle on different parameters. Notably the first sections deal with the static contact angle, that is, of a system in equilibrium. The important topic of dynamic contact angle and hysteresis of measurement are also treated in the fourth section. The fifth section develops the notion of static and dynamic contact angle further. A moving bubble is used as an example to illustrate the possible lubrication effects that may arise. The last section details some aspects of the pressure drops given by the Young-Laplace equation and relate them to surface energies.

### 4.1 Classical Description

When a liquid drop is placed on a solid surface it will normally not only be in contact with the surface, but also with a gas. The liquid will not wet the solid totally, but remain as a drop having a specific angle of contact with the solid, the static contact angle (see Figs. 4.1 and 4.2). The important Young's equation is derived in the following.

#### 4.1.1 The Young Equation

Classically, as for the surface tension, the contact angle is dealt with in two ways: firstly, a force balance method that leaves some questions unanswered

---

<sup>1</sup>Capillarity is the phenomenon resulting from the fact that liquids have a finite or zero contact angle with solids. Examples of this are described in Chap. 5.

and secondly, the more useful and correct energetic description. The two do of course yield the same solution. Nevertheless the force description is quite intuitive.

**Force Balance**

When in static equilibrium the line delimiting the wetted and the dry part of the surface, the contact line, has to remain fixed.

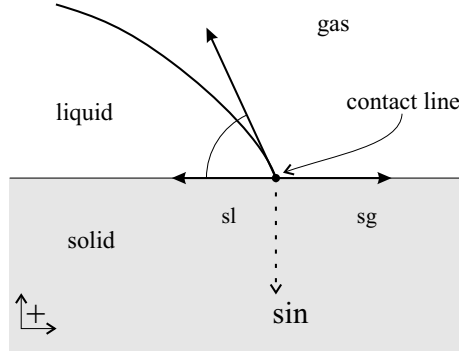


Figure 4.1: Static force equilibrium of the contact line of, e.g., a liquid drop placed on a solid.

In the horizontal direction this is fulfilled by a simple force balance illustrated in Fig. 4.1. Hence having

$$\sigma \cos \theta = \sigma_{sg} - \sigma_{sl}, \tag{4.1}$$

where  $\sigma \cos \theta$  is the force component of the liquid-gas surface tension  $\sigma (= \sigma_{lg})$ .  $\sigma_{sg}$  is the solid-gas surface tension and  $\sigma_{sl}$  is the solid-liquid surface tension. The surface tensions are here treated as "force per length" along the contact line. Eq. (4.1) is known as the Young's equation and was first published in 1805.

Now, static equilibrium also requires a force balance in the vertical direction. A normal force,  $\sigma \sin \theta$  must hence act downward on the solid at the contact line. As described in Probst [2] there is no unambiguous description of that force component. This last fact leads to a more consistent description of the contact angle, namely, an energetic.

**Energy**

A system in static equilibrium is in a configuration of minimum energy. At constant pressure and temperature the energy of relevance is the surface free energy  $G^s$ , i.e., the surface tensions  $\sigma$ , see Eq. (3.16).

With an eye on Fig. 4.2 the change in total surface free energy,  $\Delta G^s$ , resulting from a displacement,  $dx$ , of the liquid is

$$\Delta G^s = \Delta \mathcal{A}(\sigma_{sl} - \sigma_{sg}) + \sigma L \Delta l. \tag{4.2}$$

Where  $L$  is the arc length along the contact line, hence  $\Delta \mathcal{A} = L dx$ . With  $L \Delta l = L(l_d - l)$ , that is, a first order Taylor approximation to the change in area on the gas-liquid interface.  $\Delta l$  is found by applying the sine relations to the triangle with the sides  $l$   $l_d$   $dx$ , i.e.,

$$\frac{\sin(d\theta)}{dx} = \frac{\sin(\theta - d\theta)}{l} = \frac{\sin(\pi - \theta)}{l_d}$$

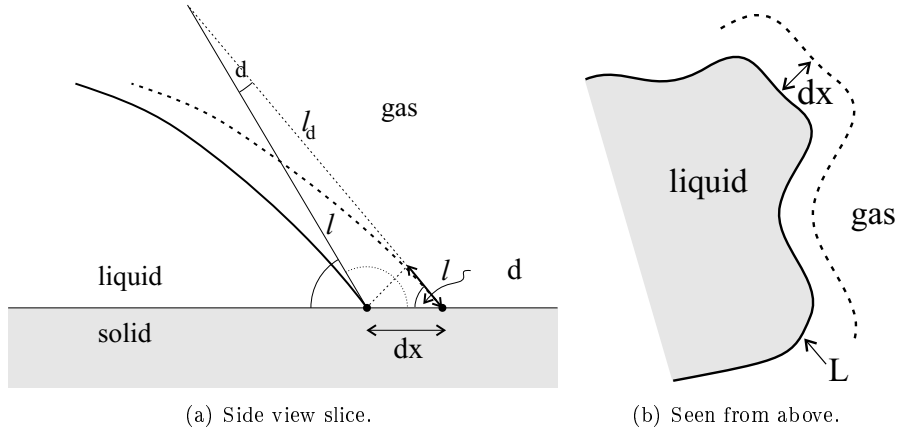


Figure 4.2: Set to find the surface energy minimum by finding the change in free surface energy accompanying a small displacement  $dx$  of the contact line. The liquid-gas interface length is increased by  $\Delta l$ .

using this and the trigonometrical addition formula yields

$$\begin{aligned} \Delta l = l_d - l &= dx \left( \frac{\sin(\pi - \theta)}{\sin(d\theta)} - \frac{\sin(\theta - d\theta)}{\sin(d\theta)} \right) \\ &\simeq dx \left( \frac{\sin(\theta)}{d\theta} - \frac{\sin(\theta) - \cos(\theta)d\theta}{d\theta} \right) \\ &= dx \cos(\theta). \end{aligned} \quad (4.3)$$

In deriving Eq. (4.3)  $\sin(d\theta) \simeq d\theta$  as  $dx$  tends to zero<sup>2</sup>. This is motivated by the fact that at equilibrium

$$\frac{dG^s(\mathcal{A})}{d\mathcal{A}} = \lim_{\Delta\mathcal{A} \rightarrow 0} \frac{\Delta G^s}{\Delta\mathcal{A}} = 0. \quad (4.4)$$

The above equation expresses that the surface free energy is at a minimum when in equilibrium. Inserting Eq. (4.2) and Eq. (4.3) into Eq. (4.4) yields

$$\sigma \cos \theta = \sigma_{sg} - \sigma_{sl}, \quad (4.5)$$

that is, the Young equation. The expression in Eq. (4.4) states that at equilibrium the surface free energy is at a minimum, any change in  $\Delta\mathcal{A}$  will increase  $G^s$ .

In the Young's equation Eqs. (4.1) and (4.5) it should be pointed out that the interfaces liquid-solid, liquid-gas, and solid-gas are in equilibrium. According to Adamson and Gast [1] the surface tension  $\sigma_{sg}$  should in fact be given as

$$\sigma_{sg} - \pi^0 \quad (4.6)$$

where  $\pi^0$  is the change in surface tension (interfacial free energy) due to adsorption. That is, the attachment of particles to the solid surface. As mentioned

<sup>2</sup>In general a Taylor expansion should have been made both in  $\theta$  and  $x$ . It is readily shown (Adamson and Gast [1]) that all other terms go to zero at least as  $dx^2$  for  $dx \rightarrow 0$ .

$G \equiv G(P, T, N)$  and so a function of the number of particles  $N$ . The change  $\pi^0$  can be found from the Gibbs equation (Adamson and Gast Ch. III-5 [1], and Atkins [6]). It relates changes in the surface tension with the changes of the substances present at the surface. The surface tension of a solid changes with adsorption of gas molecules, i.e., depending on the gas pressure  $P$  in general related to the saturated vapor pressure  $P^0$ . For constant temperature

$$\pi^0 = \frac{RT}{\Sigma} \int_0^{P^0} n d(\ln \phi P) \quad (4.7)$$

where  $\phi$  is the fugacity coefficient, that is, the deviation from the ideal gas law (for an ideal gas  $\phi = 1$ ). The surface excess per square centimeter is  $\Gamma_s = \frac{n}{\Sigma}$ , with  $n$  the moles adsorbed per gram and  $\Sigma$  the specific surface area.

### 4.1.2 Adhesion

It is further interesting to define the work of adhesion,  $W_{sl}$ , in a solid-liquid interface. In this context ideal adhesion is simply defined as the adhesion on uniform materials over a well defined unit surface area. The work of adhesion is simply the change in surface free energies given as

$$W_{sl} = \sigma_{lg} + \sigma_{sg} - \sigma_{sl}. \quad (4.8)$$

Hence the work required to separate one unit area solid-liquid into one unit area solid-gas and one liquid-gas. Combining Eq. (4.8) and the Young's equation yields an alternative definition of the contact angle

$$W_{sl} = \sigma(1 + \cos \theta) \quad \text{with} \quad \sigma \equiv \sigma_{lg}. \quad (4.9)$$

### 4.1.3 Wetting and Spreading

Young's equation may be written in yet another form

$$k = \frac{\sigma_{sg} - \sigma_{sl}}{\sigma} = \cos \theta \quad (4.10)$$

where  $k$  is the wetting coefficient. It is important to note that there is no restriction on the magnitude of  $\sigma_{sg}$  and  $\sigma$ , nor on the sign and magnitude of  $\sigma_{sl}$ . Their magnitude depend on the appropriate inter molecular forces (see next subsection). It is only required that  $-1 \leq k \leq 1$ , several cases are distinguished see Fig. 4.3 and the following:

$k = 1$ : The contact angle  $\theta$  is zero and the the liquid spreads completely over the solid. The solid is termed "completely wetted". The idea is that here  $\sigma_{sg} = \sigma + \sigma_{sl}$  and the system finds it equally profitable to have a solid-gas interface as having a solid-liquid and liquid-gas interface. Gravity and intermolecular forces lower the overall potential energy by "totally" spreading out the liquid.

$0 < k < 1$ :  $\theta$  lies between 0 and  $\frac{\pi}{2}$  and the solid is said to be "wetted". This term might be a little confusing as the solid is actually only partially wetted.

$-1 < k < 0$ :  $\theta$  lies between  $\pi$  and  $\frac{\pi}{2}$  and the solid denoted "un-wetted" by the liquid. This statement is again a little confusing as the solid is partially wetted.  $\sigma_{sl}$  is not large enough to inhibit wetting. E.g., a drop of mercury on glass has  $\theta \simeq 180^\circ$ , this is a consequence of the strong inter molecular forces within the liquid.

$k = -1$ : The contact angle  $\theta$  is  $\pi$  and the solid is completely un-wetted. This limit is un-physical, but can be modeled by assuming the liquid supported by a thin film of gas.

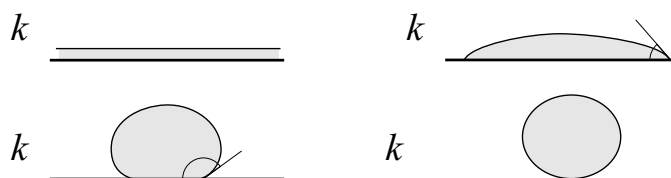


Figure 4.3: A schematic representation of the four different wetting configurations.

It is further possible to introduce yet another quantity  $\mathcal{S}$  termed the spreading coefficient, given as

$$\mathcal{S} = \sigma_{sg} - \sigma_{sl} - \sigma. \quad (4.11)$$

Introducing this in the Young's equation yield

$$k = 1 + \frac{\mathcal{S}}{\sigma} = \cos \theta. \quad (4.12)$$

For  $\mathcal{S} > 0$  it is evident that no equilibrium can exist in the contact line as  $\mathcal{S} > 0 \Rightarrow k > 1$ .  $\mathcal{S} > 0$  implies that  $\sigma_{sg} > \sigma_{sl} + \sigma$  meaning that a solid-gas interface would immediately be replaced by solid-liquid and liquid-gas interfaces (having lower energy). According to Probstein [2]  $\mathcal{S} > 0$  is only possible on a molecular scale where as  $\mathcal{S} = 0$  is the condition for complete wetting on a macroscopic scale (see above).

Examples of the capillary phenomena emerging from finite contact angles, i.e., the presence of a surface free energies or surface tensions are presented in Chap. 5. But first some microscopic theory is investigated.

## 4.2 Molecular Description

In the previous section a classical thermodynamical description of the contact angle phenomena was presented. The purpose is now to present and comment a molecular (or quantum mechanical) approach described in the work by Kwok and Neumann [9, 10], from 1999 and 2000. The work is based on new surface tension and contact angle measurements.

The idea is to utilize the theory from intermolecular interaction in terms of attractive potentials and so-called combining rules. The frame of the theory is then used as guesses for several formula combining: contact angle  $\theta$ , surface tensions  $\sigma$ , and work of adhesion.

The van der Waals forces is a general term for intermolecular forces in liquids, they include interactions between permanent and/or induced molecular dipole moments. If the stronger hydrogen bonds are present in the liquid (e.g., in water) they dominate the van der Waals (Atkins [6]). The van der Waals interactions are also important in the fewer solids where the much stronger ionic, covalent, and metallic bonds are absent (Elliot Ch. 2.2.2 [11]). The general form of a van der Waals attractive potential is

$$\phi_{ij} = -\frac{C_6}{r^6} \quad (4.13)$$

where  $r$  is the distance between two molecules,  $C_6$  is a coefficient that depends on the identity of the molecules, and  $i, j$  denotes specific molecules. Generally  $C_6$  includes all van der Waals contributions. A limitation of Eq. (4.13) is that it only relates interactions of pairs of molecules. Interactions of, say, three molecules are given by the Axilrod-Teller formula. Eq. (4.13) is only the attractive part of the total potential of interaction. When two molecules come too close nuclear and electronic repulsion take over, the repulsion is included, e.g., in the well known Lennard-Jones (12,6)-potential model

$$V(r) = 4\epsilon \left[ \left( \frac{r_0}{r} \right)^{12} - \left( \frac{r_0}{r} \right)^6 \right] \quad (4.14)$$

where  $r_0$  is the collision diameter and  $\epsilon$  is the energy-well depth.

The work of Kwok and Neumann takes expressions like Eqs. (4.13) and (4.14) together with different combining rules<sup>3</sup> and apply them to surface properties, all though some points are left unanswered in their work as only interactions between induced dipole moments are taken into account<sup>4</sup>. Notice that solids may be polar or combine in hydrogen bonds with the liquid. Only few solids are van der Waals solids. Hence one should be aware of these restrictions, as they also point out in the articles the validity of the combining rules lack experimental support.

By the joint application of a modified molecular model, classical theory (presented in the previous section), and data fitting they provide the semi empirical formula,

$$\cos \theta = -1 + 2 \sqrt{\frac{\sigma_{sg}}{\sigma_{lg}}} \left( \frac{4(\sigma_{sg}/\sigma_{lg})^{1/3}}{(1 + (\sigma_{sg}/\sigma_{lg})^{1/3})^2} \right)^{(\alpha\sigma_{sg})^{2/3}} \quad (4.15)$$

where  $\alpha = 1.17\text{m}^2(\text{mJ})^{-1}$  is a numerical fitting constant. In the articles  $\alpha$  is found to be nearly independent of the chosen materials

All measurements are made on a few synthetic surfaces as, e.g., PMMA. The results are compared with measurements of the contact angle and show an accuracy of Eq. (4.15) in the order  $\pm 2^\circ$ . The work on microscopic models presented here seems encouraging, but clearly needs some generalization.

<sup>3</sup>A combining rule is used to express the energy well depth  $\epsilon$  of two unlike molecules in terms of the energy well depth of two like molecules. This rule may, e.g., contain ionization and polarizability parameters. The simplest rule is the Berthelot rule:  $\epsilon_{ij} = \sqrt{\epsilon_{ii}\epsilon_{jj}}$ .

<sup>4</sup>This interaction energy is given by the London formula (Atkins [6]) and is normally derived quantum mechanically by a perturbation method, Bransden and Joachain Ch. 15 [13].

The models presented in this and the previous section are all for ideal solids and liquids. The contact angle given is based on the Young equation. In practical measurements there are many physical parameters that influence on the contact angle. They are discussed in Sec. 4.4.

### 4.3 Experimental Data

Data for the static contact angle (the Young angle) is given in Table. 4.1.

Contact Angle Data, 20 – 25°C.					
Liquid	Solid	$\theta$	$\frac{d\theta}{dT}$	$\pi^0$	Ref.
Water	PMMA	73.7	-	-	[10]
Glycerol	PMMA	66.8	-	-	[10]
Formamide	PMMA	57.7	-	-	[10]
Water	Platinum	40	-	-	[1]
Water	Gold	0	-	-	[1]

Table 4.1: Data for the static measured contact angle (the Young angle).

### 4.4 Dependence of the Contact Angle

In the previous sections the contact angle has been treated as a stable and static quantity (the Young contact angle). This is in general not true as contact angles may be meta stable and differ from the quantity predicted from the Young equation  $\theta$ . This is the phenomenon of contact angle hysteresis: the usual observation is that the measured contact angle for a liquid advancing on a surface  $\theta_A$  is different from the one receding  $\theta_R$  from a surface. The difference  $\theta_A - \theta_R$  is the contact angle hysteresis and can be as large as  $50^\circ$  for water on mineral surfaces, Adamson and Gast [1]. An example of an experimental setup capable of measuring both advancing and receding contact angles is seen in Fig. 4.4.

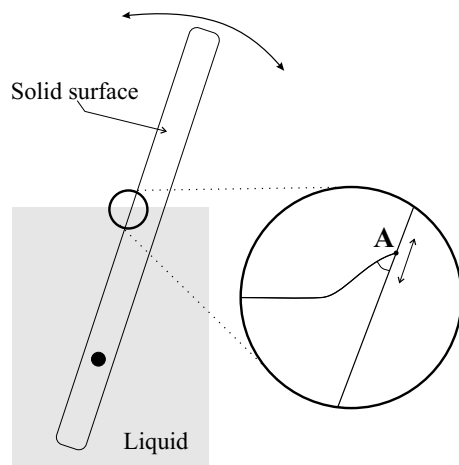


Figure 4.4: An experimental setup enabling the measurement of both advancing and receding contact angles of a liquid on a solid. The movement direction of the contact line at **A** depends on the movement direction of the stick. The stick is rotating about a fixed axle. Dussan V. *et al.* [16].

The static contact angle further differs for non-static measurements when the contact line is moving. The measured parameter is the dynamic contact angle  $\theta_d$ . It is dependent on velocity and deformations due to viscous forces that is on the capillary number  $Ca$ .

The main causes to hysteresis (heterogeneous surfaces, surface roughness, and liquid-surface interactions) are presented below together with the dynamic contact angle.

#### 4.4.1 Heterogeneous Surfaces

Surfaces having areas of impurity or being made up of, say, two materials (with distinct separated areas over small length scales) are said to have heterogeneities. These can be modelled by the Cassie equation

$$\sigma \cos \theta = f_1(\sigma_{s1g} - \sigma_{s1l}) + f_2(\sigma_{s2g} - \sigma_{s2l}) \quad \Leftrightarrow \quad (4.16)$$

$$\cos \theta = f_1 \cos \theta_1 + f_2 \cos \theta_2 \quad (4.17)$$

where  $f_1$  and  $f_2$  are the fractions occupied by surface with contact angle  $\theta_1$  and  $\theta_2$ , respectively. Adamson and Gast [1] also propose to average (or weight) the two different areas by

$$(1 + \cos \theta)^2 = f_1(1 + \cos \theta_1)^2 + f_2(1 + \cos \theta_2)^2. \quad (4.18)$$

The validity of the two model depend on the given situation.

An interesting application of the Cassie equation (Eq. 4.17) is for drops on a woven material, i.e., a material with open areas (like a filter). In this case  $\cos \theta_2 = -1$  as  $\theta_2 = 180^\circ$ , that is, un-wetted material, yielding

$$\cos \theta = f_1 \cos \theta_1 - f_2. \quad (4.19)$$

The presence of these multiple contact angles on the material causes meta-stable equilibrium states of the system. The contact line has a tendency to pin to the patches of different material (it has to overcome an energy barrier). In turn showing up as a hysteresis phenomenon.

#### 4.4.2 Surface Roughness

On rough surfaces the contact angle is again different from the one predicted by the Young equation (Eq. (4.5)). The effects of roughness is modelled by the Wenzel equation

$$\cos \theta_{\text{rough}} = r \cos \theta \quad (4.20)$$

$r$  is the ratio between the actual area and the projected area, and  $\theta$  is the ideal angle predicted by the Young equation. Hence an apparent (or projected) area  $A_{\text{apparent}}$  is related to the actual area  $A = rA_{\text{apparent}}$ , i.e.,  $r > 1$ . Eq. (4.20) implies that contact angles less than  $90^\circ$  are decreased and angles greater than  $90^\circ$  are increased by roughness.

Note that Eq. (4.20) is an empirical formula, generally contact angle measurements on rough surfaces are non-reproducible (Adamson and Gast Ch. X.B [1]). Furthermore roughness is greatly dependent on topology: parallel groves and pits may have the same roughness,  $r$ , but yield completely different angles.

### 4.4.3 Liquid-Surface Interactions

Another set of causes for hysteresis arise when the liquid interacts with the solid. The liquid may traverse the solid and alter its molecular structure through chemical interactions. Hence the contact angle may be different for the receding liquid as the surface is altered by the advancing liquid.

The reproducibility of measurements is here time dependent as chemical reaction times may play a role in the effective alteration of the solid-surface.

### 4.4.4 Dynamic Contact Angle

Whenever a contact line (triple point: solid-liquid-gas intersection) is in movement the contact angle can no longer be seen as a static quantity. The angle becomes dependent on the speed at which the line moves over the solid: the angle is dynamic<sup>5</sup>.

When the contact line is moving the force balance incorporated in the Young equation Eq. (4.1) is no longer satisfied because, among other things, viscous stresses in the liquid (Probstein [2]). This property hints the importance of the capillary number  $Ca$  (recall Sec. 3.6) in the description of the dynamic contact angle  $\theta_d$ .

A description and understanding of the dynamic contact angle requires detailed hydrodynamics and to some extent theory for molecular interactions. The problem is not anymore based solely on thermodynamics and energy considerations as for the Young equation. A key element in the description is a proper description and definition of the boundary condition at the contact line. Where the length scale requires the use of a so-called slip condition.

A classical model with a no-slip condition yields a singularity at the moving contact line. For the classical model to hold, an infinite force would be required to sink an object into a liquid (Ramé and Garoff [18]), because it predicts an infinite drag force. Several steps and approaches have been made to solve this problem:

**1:** The first procedure (already introduced in 1976 by Dussan V. [17]) used to remove the singularity is having a slip condition at the solid-liquid interface (mathematically a Green condition):

$$b \frac{\partial v}{\partial z} = v_0 \quad \text{at} \quad z = 0. \quad (4.21)$$

Where  $v_0$  is the extrapolated velocity and  $b$  is the so-called slip length (Sec. 1.10 in Smith and Højgaard Jensen [14]), see Fig. 4.5. The physical interpretation of the condition is the sliding motion of the molecular layer closest to the solid. Another way of interpreting Eq. (4.21) is through the linear relation between the velocity along the surface and the shear stress (Newton's formula:  $\tau = \mu \frac{dv}{dz}$ ). The proportionality constant  $b$ , the slip length, is a phenomenological parameter and describes the intermolecular interaction between solid and liquid. The parameter

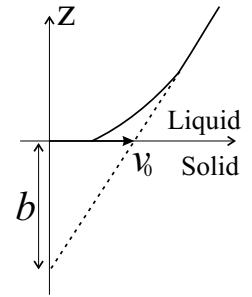


Figure 4.5: The definition of the slip length  $b$ .

<sup>5</sup>In any slow motion of bubbles having contact with a solid (a liquid-gas interface motion) in, say, a microchannel the contact angle is dynamic. As this quantity plays a key role in any model (numerical or analytical) and thus in the shape of the interface its understanding is essential. It is here assumed that the bubble wets the walls (see the next section), so that there is a triple point.

has to be small for the sliding effect only to be significant near the moving contact line, where the stresses are important. This method yields results on the form

$$Ca \equiv \frac{\mu U}{\sigma} = k\theta_d^3, \quad (4.22)$$

where  $k$  is a constant dependent on the approximations made. Generally the model yields good results for small contact angles and small capillary numbers  $Ca \ll 1$ , de Gennes *et al.* [15].

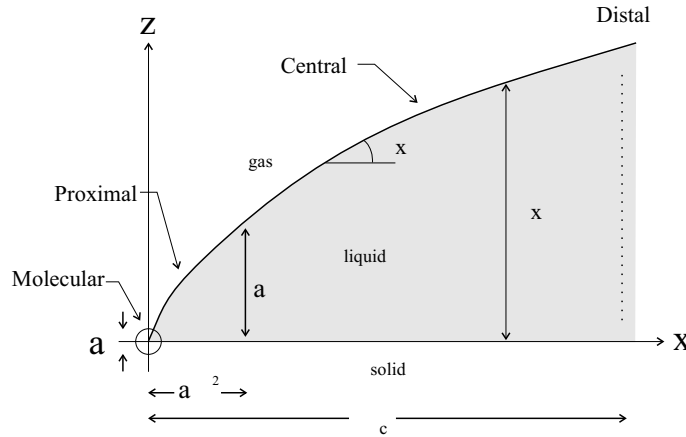


Figure 4.6: The four regions in the interface profile: 1. Molecular 2. Proximal (long range van der Waals forces are predominant) 3. Central (controlled by viscosity and surface tension) 4. Distal (controlled by viscosity and gravity). De Gennes *et al.* [15]

**2:** Secondly, more recent methods build upon dividing the area near the contact line into different regions. In each region different physical properties are prevailing characterized by the Bond number (see Sec. 3.6) and the limit of the continuum representation of a liquid characterized by the Knudsen number  $Kn$  (see Sec. 2.1). The relevant physical equations are solved in each region and equated at the boundaries by asymptotic methods. The slip boundary condition is therefore still used.

A very elaborate method divides the area into four regions shown in Fig. 4.6. The method is very detailed and uses a long-range van der Waals forces model in the region nearest the contact line (this prevents the appearance of a singularity). Though in theory quantum mechanics should be used on the molecular scale at the contact line itself. The method was presented in 1989 by de Gennes *et al.* [15] (abbreviated dGHL). Notice that in the distant region gravity is also accounted for. The model is here again restricted to low capillary numbers,  $Ca < 10^{-3}$ . Ramé and Garoff [18] have further elaborated a model for the central region accurate for capillary numbers up to 0.1.

The dGHL method expands the profile to first order in  $Ca$  around the static solution. In the central region where  $x \gg a/\theta^2$ , with  $\theta$  the static contact angle at equilibrium and  $a$  the molecular size, the local profile slope is readily given

as

$$\frac{d\zeta}{dx} = \theta(x) = \theta_e \left[ 1 + \epsilon \ln \left( \frac{2x\theta^2}{a} \right) \right], \quad \epsilon = \frac{3Ca}{\theta^3}. \quad (4.23)$$

Where  $\epsilon$  is the perturbation parameter. Note that in Eq. (4.23) there is a natural length scale  $a/\theta^2$ . It provides a measure for the length scales involving the long range van der Waals forces.

A commonly used expression for the dynamic contact angle is an expression obtained by O. V. Voinov in 1976. It relates the dynamic and the static contact angle through the capillary number,

$$\theta_d^3 = \theta^3 + 9Ca \ln \left( \frac{H}{L_s} \right) \quad (4.24)$$

where  $L_s$  is the slip length and  $H$  is a macroscopic dimension characteristic for the flow. Eq. (4.24) can be derived from Eq. (4.23) as we recognize  $L_s = a$  (de Gennes *et al.* [15]) and set  $x \approx \Delta_c$ . Taking the cube of Eq. (4.23) yields, to first order in  $Ca$ ,

$$\theta^3(\Delta_c) \simeq \theta_d^3 = \theta^3 + 9Ca \ln \left( \frac{2\Delta_c\theta^2}{a} \right) + \mathcal{O}(Ca^2). \quad (4.25)$$

The equation has exactly the same form as Eq. (4.24). The dynamic contact angle is hence the outcome of a game between wettability (the static contact angle) and a hydrodynamic contribution. Eq. (4.24) predicts a continuous change of  $\theta_d$  with increasing velocity, starting from  $\theta$ . Though experimentally the relation is only valid for  $Ca > Ca_{min}$ , where  $Ca_{min}$  can be found experimentally.

It is here important to notice that measurements yield a macroscopic so-called "visible" contact angle. This angle is different from the actual "true" or microscopic value. This is exactly why  $x \approx \Delta_c$  is chosen in Eq. (4.25). As  $\Delta_c$  is a macroscopic length characterizing the transition from surface tension to gravity dominated regions, thus Eq. (4.25) yields the macroscopic contact angle. It should be pointed out that the concept of a true contact angle itself is dangerous as it predicts a sharp interface at the contact line. For increasing capillary numbers (and hence speeds) the sharp interface vanishes and lubrication phenomena appear. These considerations are further developed in the next section.

**3:** Finally some extra work has been put into defining a proper slip like condition. The condition stated in Eq. (4.21) still leaves a logarithm term not defined on the contact line (see Eq. (4.23)). The first condition was a hydrodynamic slip condition involving the shear stress. Another version of the slip condition (Pismen and Rubinstein [20]) defines the slip velocity through the thermodynamic potential  $\Omega \equiv \Omega(T, V, \mu_c) = F - \mu_c N$ :

$$v = -\frac{D}{nk_B T} \nabla \Omega, \quad \text{at } z = 0. \quad (4.26)$$

Where  $D$  is the surface diffusivity,  $n = N/V$  the particle number density,  $k_B$  is Boltzmann's constant, and  $T$  is temperature. The condition Eq. (4.26) follows from physical kinetics; diffusion in the first molecular layers above the solid.

Using this kinetic slip condition and the same division into zones as described above, yields

$$\zeta(a) = \left( \frac{a^4 Ca}{3\lambda_b^2 r_0^2} \right)^2, \quad \lambda_b = \sqrt{\frac{\mu D}{nk_B T}}. \quad (4.27)$$

where  $\lambda_b$  is the effective slip length,  $r_0$  is the van der Waals length (collision diameter),  $a$  is the typical molecular diameter, and  $\mu$  is the dynamical viscosity. The dynamic (microscopic) contact angle is thus

$$\theta_d = \arctan \left[ \frac{\zeta(a)}{a} \right]. \quad (4.28)$$

## 4.5 Lubrication vs. Contact Angle

The notions of static and dynamic contact angles have been discussed thoroughly in the previous sections. It is thus obvious that a static bubble with sufficient volume will wet the walls of a capillary tube. Obviously given the liquid-gas interface has a finite contact angle with the specific solid. What happens at increasing flow rates should be considered in details.

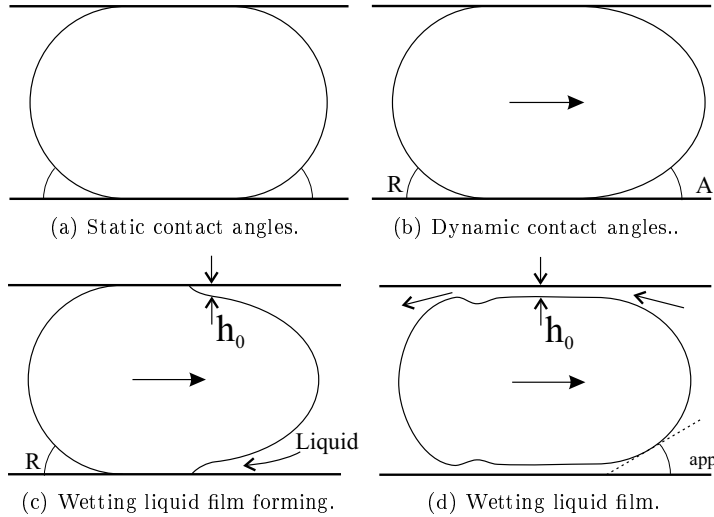


Figure 4.7: Schematic progress in the wetting behavior of bubbles at increasing capillary numbers.

Say that in the static position the interface has a given static contact angle  $\theta$  with the walls, Fig. 4.7(a). Whenever a sufficient external pressure is applied on the tube the bubble will start to move and the contact angles will change as a function of the capillary number (dynamic contact angle). There will be an advancing angle  $\theta_A$  and a receding angle  $\theta_R$  Fig. 4.7(b). The meniscus will deform. At still increasing capillary numbers the viscous forces become more important. A film of liquid starts to form at the front of the bubble (a lubrication process, Probstein [2]), Fig. 4.7(c). A final increase of the capillary number will create a wetting liquid film around the bubble, Fig. 4.7(d). In this last configuration there will still be an apparent contact angle  $\theta_{app}$  as the film generally is very

thin. At capillary numbers greater than some critical value, typically  $\approx 1$ , bubbles can undergo deformations and break into smaller bubbles.

The four steps described above are very schematic. Some of the aspects and problems involved are in the following discussed in relation to several articles [24, 25, 26, 27, 28, 29, 31, 32] and Gravesen [33].

The general trend in literature, when dealing with the motion of bubbles, is to adopt either the contact angle or the thin film lubrication model: Ransohoff *et al.* [24] use the contact angle model to determine conditions for snap-off of gas bubbles. Stark and Manga [26] only consider the motion of non-wetting bubbles in their simulation of bubbles in networks of tubes (an approximation to porous materials). Moreover when the wetting model is applied one should also take friction at the contact line into account. This is discussed in more detail in Sec. 5.2.

The classical reference in the non-wetting bubble (lubrication or thin film) model is from 1961 by Bertherton [28]. Further work is made by Parker and Homsy [29] in 1983, and Ratulowski and Chang [25] in 1989. The three articles focus on the hydrodynamic aspects of the travelling bubble problem. The later article also focus on surfactants leading to Marangoni effects. Summarized the pressure drop over the bubble is shown to be proportional to  $\frac{\sigma}{r}(3Ca)^{2/3}$  and the wetting film thickness  $h_0$  proportional to  $r(3Ca)^{2/3}$  where  $r$  is the tube radius. The relations are useful up to  $Ca \simeq 10^{-1}$ . When letting  $Ca$  tend to zero one should be aware when the theory predicts length scales at which non-hydrodynamic contributions take effect,  $\ell \approx 100$  nm. At these dimensions long range molecular forces exist between macroscopic objects (van der Waals dispersion forces, see Adamson and Gast [1] Ch. 6 or Atkins [6]).

The models for dynamic contact angle are generally restricted to  $Ca < 10^{-3}$ . Though Ramé and Garoff [18] found agreement with experimental results, for the so-called central region, for  $Ca < 10^{-1}$ . This could well be true as the bubble interface keeps an apparent contact angle, Fig. 4.7(d), when the wetting film forms. The two theories might very well predict the same physical behaviors in the transition  $Ca$  regimes. At present no literature has been found comparing the two theories.

Methods exist to handle the physical properties of the wetting film while keeping the apparent contact angle description. A so-called disjoined pressure  $\Pi(h)$  is introduced in the Young-Laplace equation, where  $h$  is the distance from the interface to the wall. The equation is called the augmented Young-Laplace equation. A thorough description is given by Wong *et al.* [36].

The problems involved in the transition from the wetted bubbles to the non-wetted bubble is not here treated in detail. However, here is a list of things to consider:

- The transition back and forth could show hysteresis and hence have a nonlinear behavior.
- What are the dynamics involved when the bubble dries the surface (the gas bubble wetting the wall).
- As mentioned, what happens when the film becomes of the same length scales as, e.g., the surface roughness.

- Can pools of liquid appear/form on the solid surface within a dried region.

The theory of wetting films is investigated thoroughly in courses given by an assembly of scientist in Les Houches, France in 1988 [31, 32]. Both thermodynamical, mean field, and microscopic theories are presented and discussed in relation to experimental results. Lubrication and wetting is also discussed by Adamson and Gast [1] Ch. 12-13. Finally, work on the stability of wetting films investigating nucleation and capillary waves is made by Schulze *et al.* [27].

## 4.6 Notes on Pressures and Energy

This section firstly introduces some short notions about driving pressures when a bubble is present in a capillary tube. The emphasis is especially put on the sign and actual pressure drops involved. Only pressure drops due to interface curvature, given by the Young-Laplace equation, are considered. Friction is in the following neglected. Secondly to supplement the first pressure part an energy consideration is made.

### Pressures

First of all the sign convention used in the Young-Laplace equation, Eq. (3.9), is illustrated in Fig. 4.8. The pressure over a curved interface  $\Delta P_i$  is always given as the internal (concave side) pressure minus the external (convex side) pressure (all curvatures are positive). This convention actually results from the definition of positive work in the derivation of the equation. It is also evident that the pressure is highest in a bubble (on the concave side).

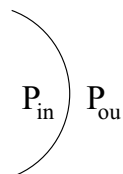


Figure 4.8: In the Young-Laplace equation Eq. (3.9) the pressure difference  $\Delta P_i$  is a positive quantity and is always defined as:  $\Delta P_i = P_{in} - P_{ou}$  where  $P_{in} > P_{ou}$ . The position of  $P_{in}$  and  $P_{ou}$  is always defined in the same manner.

To ease the understanding of the next sections and chapters a few conventions are presented in relation to Fig. 4.9.

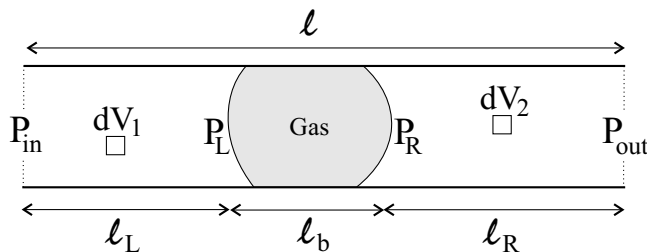


Figure 4.9: A gas bubble with length  $l_b$  in a tube of length  $l$ . Inlet pressure  $P_{in}$ , outlet pressure  $P_{out}$  and pressures to the right and left of the bubble  $P_L$  and  $P_R$ , respectively.

The pressure over the bubble is defined as:  $\Delta P_b = P_R - P_L$ . The externally imposed pressure is:  $\Delta P_e = P_{\text{out}} - P_{\text{in}}$ . Having the pressures defined in such a way one can find the driving pressure gradient  $\Gamma$  of the system. In view of Fig. 4.9 and assuming that the two fluid elements  $dV_1$  and  $dV_2$  are moving at the same speed. They experience the same gradient

$$dV_1 : \quad \Gamma_1 = \frac{P_L - P_{\text{in}}}{\ell_L} \quad (4.29)$$

$$dV_2 : \quad \Gamma_2 = \frac{P_{\text{out}} - P_R}{\ell_R} \quad (4.30)$$

the fact that  $\Gamma_1$  is equal to  $\Gamma_2$  yields

$$\Gamma = \frac{\Delta P_e - \Delta P_b}{\ell - \ell_b}, \quad (4.31)$$

where  $\ell$  and  $\ell_b$  are the tube and bubble length, respectively. The part  $\Delta P_b$  is the pressure that sustains the bubble and is thus not available to drive a flow. Hence if  $\Delta P_b$  is positive the effective pressure gradient driving the flow is smaller than expected. When bubbles clog a capillary channel one need at least a  $\Delta P_e$  higher than  $\Delta P_b$  to initiate flow. The expression for  $\Gamma$  in Eq. (4.31) can, e.g., be used in a Poiseuille flow model where bubbles are present in a cylindrical tube.

Moreover with no externally applied pressure and wall friction neglected a bubble will move by it self if  $\Delta P_b \neq 0$ . The sign of the pressure gradient  $\Gamma = -\Delta P_b/(\ell - \ell_b)$  will determine the direction. For  $\Gamma < 0$  the flow is towards the right and vice versa. This last notion naturally leads to an energy consideration.

### Minimizing Energy

Consider the 2D gas bubble in Fig. 4.10 in a given geometrical constrain. There are no externally applied driving pressures.

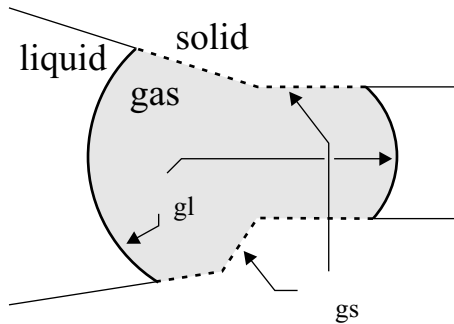


Figure 4.10: An example of a 2D gas bubble in a given geometry. The setup is used to illustrate an energy argument comparable to the driving pressure concept.

The direction of movement predicted by  $\Gamma$  will comply with an energy minimizing path. In the present case the energy of interest is the total surface energy  $E_{tot}^s$  of the bubble. In the present 2D example it is given as

$$E_{tot}^s = \sigma \Lambda_{gl} + \sigma_{gs} \Lambda_{gs}, \quad (4.32)$$

where  $\sigma$  is the gas-liquid interfacial tension,  $\sigma_{gs}$  is the gas-solid interfacial tension,  $\Lambda_{gl}$  is the length of gas-liquid interface, and  $\Lambda_{gs}$  is the length of gas-solid contact. The system will drive  $E_{tot}^s$  continuously to the local minimum. For real

3D bubbles the energy is obviously given as area times interfacial surface tension.

Even though the energy description is more physically intuitive the pressure description will be in focus in the following chapters. The so-called clogging pressure of a system is introduced.

## Chapter 5

# Capillarity and Examples

Capillary phenomena can be defined as physical behavior of liquids resulting from a finite or zero contact angle. More generally capillary motion are flows governed to some extent by surface tension. The precise nature of the flows is characterized by the bond number  $Bo$ , the capillary number  $Ca$ , and so forth.

In this chapter the subject of capillary rise is first introduced. It is a classical example of capillary motion and it illustrates some of the phenomena quite well. Secondly, and more in the scope of this thesis, a simple method to illustrate clogging of microchannels (capillary tubes) by bubbles is introduced<sup>1</sup>. The bubbles are here static or very slow moving ( $Ca \ll 1$ ) so represented by a contact angle and a hemispherical interface. Finally bubble motion in capillary tubes, at higher capillary numbers, is discussed. Marangoni effects are also taken into account. The lubrication approximation is discussed.

### 5.1 Capillary Rise

Capillary rise is the classical example of capillary motion. If a capillary tube of radius  $a$  is introduced vertically into a pool of liquid, the liquid will rise or fall due to the pressure drop over a curved interface, see Fig. 5.1 and 5.2. In the following the surface tension  $\sigma$  is assumed constant at the meniscus. The equilibrium height  $H_0$  is in the following found using an approximation and secondly the exact solution is described.

#### Simple Solution

When the tube is circular in cross section the meniscus may be approximated by a hemispherical shape. It will have constant radii of curvature  $R = R_1 = R_2 = a/\cos\theta$  where  $\theta$  is the contact angle and  $a$  is the tube radius. Deviations from hemisphericity is associated with pressure drop over the meniscus height  $h$  due to gravity, deforming the meniscus (surface tension alone will yield a hemispherical surface). The measure of the gravitational forces to surface tension is given by

---

<sup>1</sup>This example is also the basis for some of the numerical simulations of the following chapters.

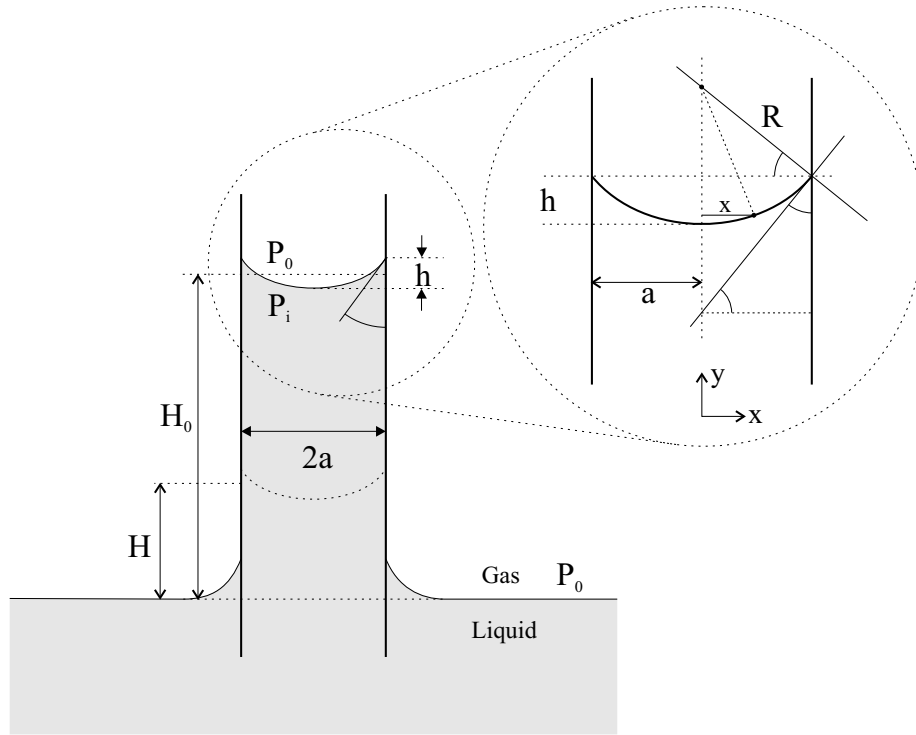


Figure 5.1: Capillary rise in a circular tube of radius  $a$ . The liquid has a contact angle  $\theta < 90^\circ$ , and a curvature  $R = \frac{a}{\cos \theta}$ . The equilibrium height of the water column is  $H_0$ .

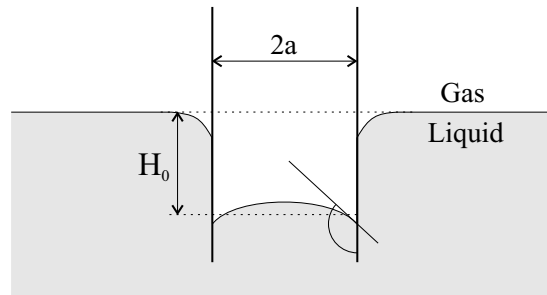


Figure 5.2: Capillary "fall" of mercury (Hg) having a contact angle  $\theta \approx 140^\circ > 90^\circ$ . The pressure drop over the meniscus here needs to be balanced by a negative pressure in the liquid.

the Bond number ( $Bo = \rho gh^2 / \sigma$ ). The condition for hemisphericity is hence

$$Bo \ll 1 \Rightarrow h \ll \left( \frac{\sigma}{\rho g} \right)^{1/2} \equiv \Delta_c, \quad (5.1)$$

where  $\Delta_c$  is the capillary length, previously mentioned.

The equilibrium height  $H_0$  is found by requiring the pressure drop due to

the curvature of the meniscus to be equal the pressure drop due to a change in water column height (at equilibrium). Hence

$$\begin{aligned}\Delta P &= P_0 - P_i \Leftrightarrow \\ 2\sigma \frac{1}{R} &= P_0 - (P_0 - \rho g H_0) \Leftrightarrow \\ 2\sigma \frac{\cos \theta}{a} &= \rho g H_0 \Leftrightarrow \\ H_0 &= 2 \frac{\sigma \cos \theta}{\rho g a} = 2 \frac{\Delta_c^2}{a} \cos \theta.\end{aligned}\quad (5.2)$$

Note that the equation is very general and accounts for the capillary "fall" whenever  $\theta > 90^\circ$ . This is the case for mercury where  $\theta \approx 140^\circ$  and is illustrated on Fig. 5.2. When  $\theta > 90^\circ$  then  $\cos \theta < 0$  resulting in the necessary sign change, i.e.,  $\Delta P = P_i - P_0$ . For small capillary tubes (small  $a$ )  $H_0$  can become relatively large: 4 cm for water in a tube with radius 0.1 mm.

It is also possible from this simple theory to predict the velocity at which the water column rises as well as the time it takes. Assuming a Poiseuille flow in the tube (Appendix B) and the meniscus to rise with the mean velocity yields

$$U = \frac{dH}{dt} = \frac{a^2 \Delta P}{8\mu H}, \quad (5.3)$$

where  $H$  is the instantaneous position of the meniscus. The pressure difference  $\Delta P$  is the unbalanced pressure difference at the interface, i.e.,

$$\Delta P = \frac{2\sigma \cos \theta}{a} - \rho g H. \quad (5.4)$$

The two equations Eq. (5.3) and Eq. (5.4) are easily integrated. The actual time to rise is

$$t = \tau \left( \ln \left( \frac{1}{1 - H_0/H} \right) - \frac{H}{H_0} \right), \quad \tau = \frac{8\mu H_0}{\rho g a^2} \quad (5.5)$$

where  $\tau$  is the characteristic time.

The relation shows that  $H \rightarrow H_0$  only if  $t \rightarrow \infty$  which is a consequence of the approximations made. Eq. (5.5) can be expanded for  $H/H_0 \rightarrow 1$  yielding

$$\frac{H}{H_0} = 1 - \exp \left( -\frac{t}{\tau} \right). \quad (5.6)$$

It should here be mentioned that capillary rise is the basis for one of the most accurate and most used methods to measure surface tensions, Probstein [2]. Further it is instructive to see how the pressure drop over a curved interface has to be balanced by an "applied" pressure drop.

### Exact Solution

The capillary rise problem can also be solved exactly (to some extent). The tube is cylindrical so that the meniscus can be represented by a surface of revolution with two main curvatures given in Appendix A. The balance of pressure at equilibrium yields

$$\rho g y = \sigma \left( \frac{1}{R_1} + \frac{1}{R_2} \right) = \sigma \left( \frac{y''}{(1+y'^2)^{3/2}} + \frac{y'}{x(1+y'^2)^{1/2}} \right), \quad (5.7)$$

where  $y = y(x)$  is the elevation to the meniscus from the flat liquid surface at every point  $y' = dy/dx$ ,  $y'' = d^2y/dx^2$ , and  $x$  is the radial distance, see Fig. 5.1. The total weight  $W_T$  of the water column is found by introducing the new coordinates  $b = y'$  and hence  $y'' = bdb/dy$ . Eq. (5.7) is thus rewritten

$$\rho gy = \sigma \left( \frac{bdb/dy}{(1+b^2)^{3/2}} + \frac{b}{x(1+b^2)^{1/2}} \right). \quad (5.8)$$

The total weight is hence by use of Eq. (5.8) given as

$$\begin{aligned} W_T &= \int_0^{2\pi} \left[ \int_0^a (\rho gy)x \, dx \right] d\varphi \\ &= 2\pi\sigma \int \left[ \frac{xdb}{(1+b^2)^{3/2}} + \frac{b dx}{(1+b^2)^{1/2}} \right] \\ &= 2\pi\sigma \left[ \frac{xb}{(1+b^2)^{1/2}} \right]_{x=0, b=0}^{x=a, b=\tan\phi} \end{aligned} \quad (5.9)$$

since  $dx/dy = 1/b$  generally and  $b = dy/dx = \tan\phi$  at  $x = a$ . Inserting the limits yields

$$W_T = 2\pi a \sigma \cos\theta. \quad (5.10)$$

It is very interesting to note that Eq. (5.10) is exactly what is expected from physical considerations: Assuming the meniscus to be "hanging" from the walls of the tube and its weight to be supported by the vertical component of the surface tension (force per length),  $\sigma \cos\theta$ , times the circumference,  $2\pi a$ .

Where the solution Eq. (5.10) is exact it is not possible to solve Eq. (5.7) explicitly. Only numerical solutions are available with the contact angle given as one of the boundary condition  $y' = \tan\phi = \tan(\pi - \theta)$  at  $x = a$ . The equation has to be solved, e.g., by the shooting and trial method as it is a nonlinear boundary value problem. This has been made in Appendix C. As expected the simple solution, Eq. (5.2), turns out to be a very good approximation whenever  $h \ll \Delta_c$ .

## 5.2 Clogging of Contracting Microchannels

The clogging of microchannels is a common problem in microfluidics and is caused by either: precipitation of materials due to chemical reactions, solid particles getting stuck or by bubbles. The clogging by bubbles is a central topic of the thesis it is discussed in this section and further studied by use of simulations in Chap.9.

The clogging by bubble is related to the specific geometry of the microchannel. A bubble might get stuck because of sharp angles or contractions of the channel. To illustrate the clogging of contracting channels two simple cases are discussed: a sudden contraction and a tapered channel, Figs. 5.4 and 5.5. Both cases are rotational symmetric and are treated using the contact angle description. The situations discussed are hence static. The clogging pressure of a system is the externally applied pressure necessary to balance the bubble when it

is clogged in a microchannel. Two main factors affect the clogging pressure: the curvature of an interface and friction at the contact line. The two factors are here discussed separately.

The tapered channel geometry has previously been investigated by MIC and Danfoss. It is the simplest alternative to a sudden contraction channel geometry. The geometry is thoroughly analyzed in Sec. 9.3 where it is found to exhibit advantages regarding the clogging phenomenon.

### Curvature (Young-Laplace)

The problem is handled in the contact angle picture, which is valid at zero or very low capillary numbers. In this limit the front and rear interfaces of a bubble are nearly static profiles and are spherical, Ratulowski and Chang [25]. This is true as the spherical shapes provide a minimal pressure drop and thus a minimum surface energy. The minimum is attained within the given geometrical and contact angle restrictions, Ranshoff *et al.* [24].

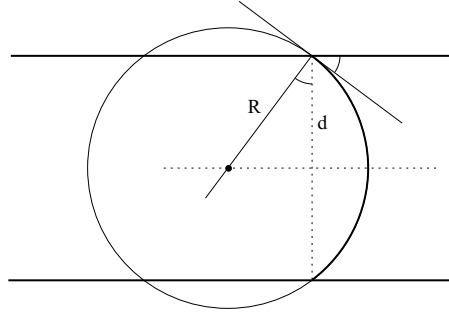


Figure 5.3: Curvature ( $1/R$ ) of a bubble in a channel of diameter  $d$ . The meniscus is assumed spherical.

Before applying the Young-Laplace Eq. (3.9) to the case illustrated in Figs. 5.5 and 5.4 the radius of curvature is determined for the simple straight channel geometry shown in Fig. 5.3. It is easily seen that

$$\cos \theta = \frac{d}{2R} \quad \Leftrightarrow \quad R = \frac{d}{2 \cos \theta}. \quad (5.11)$$

The curvature yields a pressure drop over the interface given by the Young-Laplace equation as

$$\Delta P_i = \sigma \left( \frac{1}{R_1} + \frac{1}{R_1} \right) = 4\sigma \frac{\cos \theta}{d}, \quad (5.12)$$

as symmetry of rotation implies that the two main curvatures are identical,  $R_1 = R_2 = R$ . In a straight channel the total pressure drop, due to curvature, over the bubble is obviously zero.  $\Delta P_i$  is identical with different sign at each end of a bubble.

The total pressure over the bubble  $\Delta P_b$ , in the sudden contraction geometry, is found by applying Eq. (5.11) to the case depicted in Fig. 5.4. The pressure

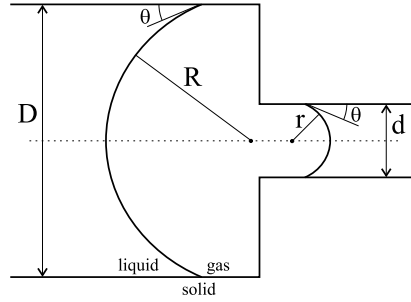


Figure 5.4: A bubble passing through a sudden contraction. The curvatures at both ends are different and constant while the bubble is in the contraction.

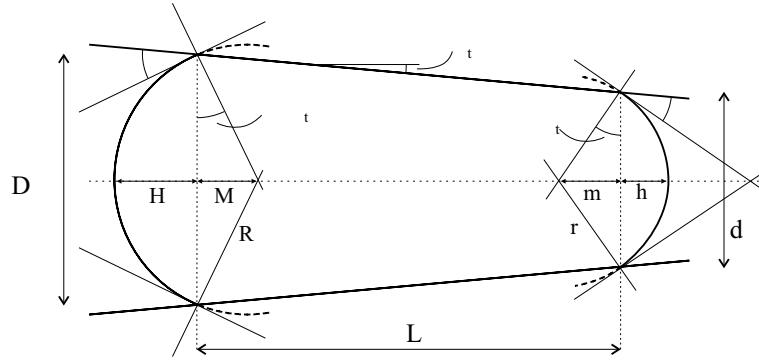


Figure 5.5: A bubble in a tapered channel. Appropriate names have been given to different lengths and angles in use. The curvatures depend on the position of the bubble because of the tapering.

drop over the bubble is

$$\Delta P_b = 2\sigma \left( \frac{1}{R} - \frac{1}{r} \right) = 4\sigma \cos \theta \left( \frac{1}{D} - \frac{1}{d} \right). \quad (5.13)$$

Similarly the total pressure difference over a bubble in a tapered channel is found by applying Eq. (5.11) to the case depicted in Fig. 5.5. All in all the total pressure difference over the bubble is

$$\Delta P_b = 2\sigma \left( \frac{1}{R} - \frac{1}{r} \right) = 4\sigma \left( \frac{\cos(\theta - \theta_t)}{D} - \frac{\cos(\theta + \theta_t)}{d} \right) \quad (5.14)$$

where  $\theta_t$  is the tapering angle and  $\theta$  is the contact angle. In this case  $D$  and  $d$  are function of position, tapering angle, and bubble volume.

It is here important to keep track of the sign conventions.  $\Delta P_b$  is as described in Sec. 4.6 the right pressure minus the left pressure ( $\Delta P_b < 0$  represents a pressure drop, etc.). The pressures are taken just outside the bubble in the bulk of the liquid.

When working with a 2D model the equations should be divided by a factor 2 as there is only one curvature for each interface. 2D models generally impose  $R_2 = \infty$ . In practice the two diameters  $d$  and  $D$  are found by requiring conservation of the total bubble volume (or area) of say an initial bubble. In Appendix D a MATLAB program analyzing the tapered channel example is presented.

### Friction

Experiments show that the liquid-solid-gas contact line in a capillary system has a definite resistance against being moved along the solid surface. The static friction of this line is accounted for through the empirical formula

$$\alpha = \frac{aP_0}{2} \quad \Leftrightarrow \quad P_0 = \frac{2\alpha}{a} \quad (5.15)$$

where  $\alpha$  is an empirical frictional surface tension parameter,  $P_0$  the minimum pressure required to initiate flow, and  $a$  the capillary radius in a cylindrical tube. Experimental data suggest that  $10 < \alpha < 100 \text{ mJ m}^{-2}$ , Schwartz *et al.* [23]. For water in a polymer tube  $\alpha \approx 10 \text{ mJ m}^{-2}$ . Though these values may be lower as  $\alpha$  is dependent on many parameters.

Work by Tenan *et al.* [21] characterize the friction through an increase in work of adhesion caused by the deformation of the meniscus. They establish a one parameter model where  $\alpha$  is defined through a "friction angle"  $\xi$ .  $\xi$  is characteristic for the specific solid (chemical nature, roughness, etc.) and is independent of the specific liquid. Using simple macroscopic theory (work of adhesion, the Young-Laplace equation, and conservation of volume) they obtain the following functional relation between  $\alpha$  and the contact angle  $\theta$  in a cylindrical tube

$$\frac{\alpha}{\sigma} = \sin \left| \theta + \xi^2 \frac{\sin^2 \theta \cos \theta}{1 + \sin \theta} \right| \sin |\xi \sin \theta|, \quad (5.16)$$

$\xi$  normally never exceeds  $\approx 0.3$ . From Eq. (5.16) it is evident that given the friction angle,  $\xi$ , of a solid the liquid-solid friction can be predicted for any liquid simply knowing the surface tension properties of the liquid, i.e.,  $\theta$  and  $\sigma$ . Similar equations to Eq. (5.16) can be derived for any geometry.

Moreover Eq. (5.16) also predicts that low friction is to be predicted at high ( $\approx 180^\circ$ ) and low ( $\approx 0^\circ$ ) contact angles since the surface tension remains finite. Finally Eq. (5.16) shows that  $\alpha$  is symmetrical about a contact angle  $\theta = 90^\circ$ , as seen in Fig. 5.6.

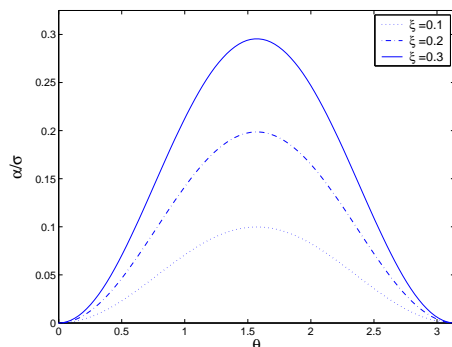


Figure 5.6: Relative friction  $\frac{\alpha}{\sigma}$  versus the contact angle,  $\theta$ , for different values of the friction angle,  $\xi$ , according to Eq. (5.16).

The friction term Eq. (5.15) is quite important in capillary flows as it is of the same order of magnitude as pressures due to the curvature of the interface. Though the friction parameter  $\alpha$  is found as a static friction parameter some papers (e.g., Matsumoto and Colgate [22]) also include the term as a dynamic friction. This makes sense, but no data is available to corroborate this.

A tentative explanation of the friction parameter might be that it basically represents all microscopic interactions with the contact line, i.e., interactions that are not accounted for in the macroscopic Young-Laplace equation. An interface between say a gas and a liquid typically has a thickness comparable to a few molecule diameters ( $< 1$  nm). The interface interacts with, e.g., roughness or chemicals on the solid surface, at the triple point, and hence induces a friction. The interactions force a deformation of the interface resulting in the energy dispersion (extra work) responsible for the friction. These interactions are also present while the line is moving and should be accounted for. Though the friction parameter,  $\alpha$ , might change from a static to a dynamic value as other effects play a role in the dynamic case (e.g., thin liquid films).

### The Clogging

The total external pressure (applied on the left hand of the channel) needed to balance a bubble in the sudden contraction is thus found from Eqs. (5.13) and (5.15), i.e., the pressure drop due to interface curvature and friction, with appropriate signs:

$$P = 4\sigma \cos \theta \left( \frac{1}{d} - \frac{1}{D} \right) + 4\alpha \left( \frac{1}{d} + \frac{1}{D} \right). \quad (5.17)$$

Similarly, the total external pressure needed to balance a bubble in the tapered capillary channel is thus found from Eq. (5.14) and Eq. (5.15) as

$$P = 4\sigma \left( \frac{\cos(\theta + \theta_t)}{d} - \frac{\cos(\theta - \theta_t)}{D} \right) + 4\alpha \left( \frac{1}{d} + \frac{1}{D} \right). \quad (5.18)$$

In this last "tapered" case the contribution from the first term can be negative because of the tapering angle,  $\theta_t$ . Note that in both cases there is a friction contribution from both end of the bubble. This theoretical approximation is compared with data from numerical simulations in the later Chap. 9.

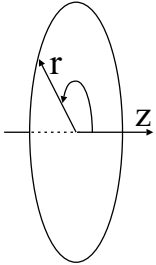


Figure 5.7: Cylindrical system of co-ordinates.

## 5.3 Non-Cylindrical Tubes

In the previous subsections the channels considered were rotational symmetric, i.e., all cross sections in the  $r, z$ -plane are circles, Fig. 5.7. Within these geometrical restrictions the bubble interface is as mentioned spherical. The resulting interfacial mean curvature  $H$  yields a minimum surface energy configuration (remember  $\Delta P_i = \sigma 2H$ , Eq. (3.9)).

Even when the cross sections are no longer circles an expression for the pressure drop over the interface  $\Delta P_i$  can be derived. In this situation wetting liquid in corner regions appear for  $0 < \theta < \theta_c$  where  $\theta_c$  is a critical contact angle, see Fig. 5.8. Whenever the contact angle  $\theta$  is greater than the critical value  $\theta_c$  the interface is still part of a generalized sphere, i.e., an ellipsoid with main curvatures  $R_1$  and  $R_2$ , Ranshoff *et al.* [24].  $R_1$  and  $R_2$  are defined by geometry and the given contact angle. For a square capillary  $\theta_c$  can be found by requiring the ellipsoid shaped interface (actually a sphere as  $R_1 = R_2$ ) to circumscribe the square cross section, i.e.,

$$\frac{a}{\cos \theta_c} = a\sqrt{2} \quad \Leftrightarrow \quad \theta_c = \frac{\pi}{4}. \quad (5.19)$$

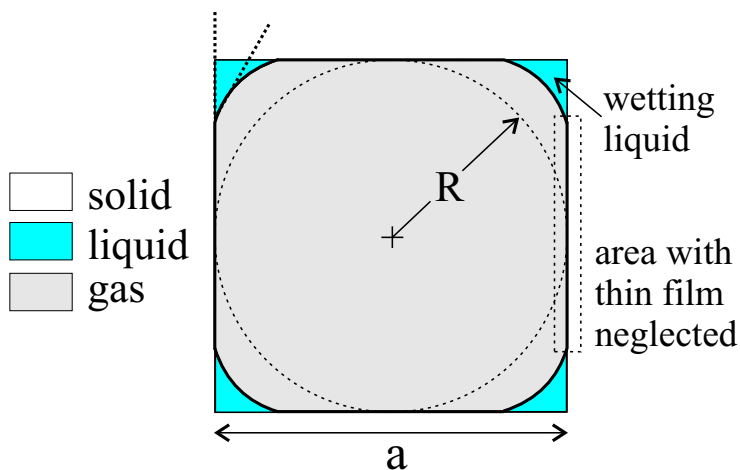


Figure 5.8: Cross section of a square capillary tube. Gas is introduced into a tube filled with liquid. The cross section is taken away from the interface front at the contact line. The liquid has a finite contact angle  $\theta < \theta_c$ . The wetting liquid and thin film regions are shown.

The first term is the diameter of the sphere (as found in Eq. (5.11)) the second the diagonal of the square. For a more details discussion see Appendix E.

The volume of liquid in the corner regions is much more important than the volume in eventual thin wetting films, see Fig. 5.8. The dynamics of the liquid in the corner regions should therefore be accounted for in dynamic models.

The method for finding the curvature, and hence the pressure drop, builds on the contact angle formulation (neglecting the thin films). The mean curvature of the interfaces  $H$  is related to a dimensionless curvature  $C_m$  through the radius  $R$  of the largest inscribed circle of the capillary tube by

$$C_m = \frac{R\Delta P_i}{\sigma} = 2RH, \quad (5.20)$$

where  $\Delta P_i$  is the pressure over the curved interface. In the case depicted in Fig. 5.8,  $R = a/2$ . Values of  $C_m$  for different geometries can be calculated by solving the Young-Laplace equation numerically in the given 3D geometry with given contact angle, Wong *et al.* [36]. The method is applicable for static menisci and solves a boundary value problem (a given contact angle) by tuning on the pressure drop (conceptually the same method as for the capillary rise problem described in Appendix C). Thus  $C_m$  depends on the specific geometry and contact angle. Values of  $C_m$  are given in Table 5.1.

The data presented in the table can be used to make static quantitative calculations of clogging pressures as was done for the circular case in Sec. 5.2.

For the case of tubes having near constant cross sections a cunning formulation by Mayer and Stowe [37] was made to determine  $C_m$  and hence  $\Delta P_i$ . The idea is to minimize the pressure drop over the interface which is the same as minimizing the surface energy. The problem is condensed to a 2D situation that can be handled analytically to great extent.

Shape	Aspect Ratio	Contact Angle	$C_m$	Ref.
Circle	-	$\theta$	$2 \cos \theta$	-
Square	-	$0^\circ$	1.886	[36]
Square	-	$15^\circ$	1.846	[36]
Square	-	$30^\circ$	1.699	[36]
Square	-	$40^\circ$	1.527	[36]
Rectangle	2	$0^\circ$	1.425	Appendix E
Rectangle	2	$20^\circ$	1.364	Appendix E
Rectangle	2	$40^\circ$	1.146	Appendix E

Table 5.1: Data for the non-dimensional curvature of menisci as function of cross section shape and contact angle.

By considering the work associated with an infinitesimal displacement of the contact line, balancing the surface free energy, and assuming the meniscus in front of the contact line to be unchanged, it is readily found that

$$\Delta P_i = \sigma \left( \frac{L_{gl} + L_{gs} \cos \theta}{A} \right)_{\min}. \quad (5.21)$$

Here  $L_{gl}$  and  $L_{gs}$  are portions of the total cross-sectional perimeter of the gas bubble  $L = L_{gl} + L_{gs}$  (e.g., the perimeter of the gas in Fig. 5.8),  $A$  is the cross-sectional area of the gas, and  $\theta$  the static contact angle.  $\Delta P_i$  can be found by making  $L_{gl}$ ,  $L_{gs}$ , and  $A$  functions of a parameter (e.g., an angle or a radius of curvature) deriving the right hand side of Eq. (5.21), and minimizing with respect to that parameter. The results from Table 5.1 are found to agree. Eq. (5.21) is derived and applied on an example in Appendix E.

The theory for these non-circular capillary tubes has mainly been derived in relation to flow in pores and is widely investigated by e.g., Mayer and Stowe [37], Ranshoff *et al.* [24], Man and Jing [34], and Reeves and Celia [35].

## 5.4 Lubrication/Thin-Film Theory

The results obtained for the motion of bubbles in circular capillary tubes at low Reynolds numbers when applying the so-called lubrication theory are here shortly presented. It is not in the scope of this thesis to derive all the equations, but some of the aspects involved are here shortly summarized. The first theoretical treatment on a steadily moving bubble at velocity  $u$  in a circular capillary tube was done by Bertherton [28] in 1960. Later in 1983 Parker and Homsy [29] formalized Bertherton's approach with use of perturbation and asymptotic matching theory. The governing equations were still mean field equations (Navier-Stokes and the Young-Laplace equations). Later more work has been done in describing the thin film region including among other things intermolecular forces. Marangoni effects resulting from surfactant on the bubble interface is discussed by Probst [2] or Schwartz *et al.* [38]. In 1989 Rutalowski and Chang [25] extend the previous discussions to shorter bubbles by an introduction of arc length coordinates measured on the bubble interface.

To solve the steady state bubble problem for low Reynolds numbers ( $Re < 1$ ) one applies the creeping flow equation of motion with appropriate boundary conditions. These are no-slip condition on the walls and the pressure given by the Young-Laplace equation on the bubble interface. Further, appropriate shear stress conditions are given on the bubble liquid interface whenever gradients in the surface tension are present (the Marangoni effect). The most important and relevant results from literature are summarized in the following two paragraphs.

### Non-Wetting Bubbles

For non-wetting bubble, in a cylindrical capillary tube of radius  $r$ , moving with speed  $u$  the pressure drop over the bubble is given as (Ratulowski and Chang [25])

$$\Delta P_b \simeq \frac{\sigma}{r} [9.40 Ca^{2/3} - 12.6 Ca^{0.95}], \quad Ca < 0.1 \quad (5.22)$$

where the capillary number is defined by the bubble speed:  $Ca = \mu u / \sigma$ . Eq. (5.22) is valid for bubbles with volumes  $V_b$  larger than the critical volume  $V_c$ :

$$V_b > V_c = \frac{4}{3} \pi r^3. \quad (5.23)$$

$V_c$  is the volume of the maximal spherical bubble possible. An important feature of the theory is that the pressure drop  $\Delta P_b$  in Eq. (5.22) is independent of the bubble length. This results from the zero shear stress condition at the liquid-gas interface. The fluid in the thin film region slips by the bubble with no drag forces. All the pressure drop results in the difference in curvature of the front and rear of the bubble.

The speed of the bubble  $u$  exceeds the average speed of the fluid  $v$  by an amount  $uw$ .  $u$  is related to  $v$  through  $w$  as

$$v = (1 - w)u, \quad w \simeq 1.29 (3Ca)^{2/3}, \quad Ca < 0.1. \quad (5.24)$$

It has been shown numerically that the last equation is valid for  $V_b > 0.95V_c$ , Stark and Manga [26]. Eq. (5.24) shows that the net back flow of liquid within the wetting films increase the velocity of the bubble. This can be understood easily by a volume conservation consideration.

At last the thickness,  $h_0$ , of the wetting film is given by

$$h_0 \simeq 0.643 r (3Ca)^{2/3}. \quad (5.25)$$

Note that non-hydrodynamic forces such as long range van der Waals, typically become important for length scales less than about 10 – 100nm, Stark and Manga [26].

### Marangoni Effects

When a surface-active material (a surfactant) is introduced in the bulk liquid the flow around the bubble, in the thin film, will cause a non-uniform distribution on the interface. This will in turn create gradients in the surface tension and hence a surface shear stress,  $\tau_s = d\sigma/dz$ . A general analysis of the problem should include a transport equation for the surface excess concentration  $\Gamma_s$ . Though a simplified model is described by Probstein [2].

The surfactant dramatically increases the shear stress in the film (it is not anymore zero on the interface). Employing a simple force balance in the film yields

$$\Delta P_b = 0.942 Ca^{1/3} \frac{\ell_b \sigma}{r^2}, \quad (5.26)$$

where  $\ell_b$  is the length of the bubble and  $r$  is the tube radius. Note that Eq. (5.26) is a first order expansion in  $Ca$  and not valid for as large capillary numbers as Eq. (5.22). Combining the Young-Laplace equation and Eq. (5.26) yields

$$\frac{1}{\sigma} (\sigma_{\text{front}} - \sigma_{\text{rear}}) = 0.471 Ca^{1/3} \frac{\ell_b}{r}. \quad (5.27)$$

Where  $\sigma_{\text{front}}$  and  $\sigma_{\text{rear}}$  are the apparent front and rear surface tensions, respectively.

The main conclusion to draw is that the introduction of surface active materials dramatically increases the pressure needed to drive a bubble. The pressures can be from two to four orders of magnitude larger than those in the absence of surfactant, Probstein [2].

## 5.5 Bubble Motion in a Capillary Tubes

Generally the description of a moving bubble in a capillary system is very complicated as it involves the handling of the free surface at the gas-liquid interface. Moreover it may be complicated by the presence of a moving contact line as is investigated in Sec. 4.4.4 or by use of lubrication theory. The task normally involves numerical methods to great extent.

Some simple geometries and cases can be treated partly analytically. As described above, the lubrication description has been investigated in great detail. One other method is to utilize the driving pressure gradient of a system presented in Eq. (4.31), in a given hydrodynamical model. Note that in the dynamic contact angle and the wetting film description the pressure over the bubble depends on the velocity ( $Ca$  number) which in turn influences the pressure drop. The system is recursive in nature.

As an example and for simplicity the capillary tubes are here assumed of circular cross section and the flow having low Reynolds numbers, i.e., Poiseuille flow theory applies (see Appendix B).

In a straight channel of length  $\ell$  the total flow rate when bubbles are present is approximated by

$$Q = \frac{\pi r^2}{8\mu(\ell - \ell_b)} \left[ \Delta P_e - \sum_{\text{bubbles}} \Delta P_b(Q) \right]. \quad (5.28)$$

Where  $\ell_b$  is the total length occupied by bubbles,  $\Delta P_b(Q)$  is the pressure drop over the bubble, and  $\Delta P_e$  is the externally imposed driving pressure.  $\Delta P_b(Q)$  is depending on the flow rate  $Q$  through the capillary number.

# Chapter 6

## Bubbles in General

The principles behind the formation of bubbles are very important especially in microfluidics where bubbles generally are to be avoided. The topic is very broad and is out of the scope of this thesis. Some of aspects are however presented shortly in this chapter. The pressure effects are very illustrative and interesting. Firstly the solubility of gases is discussed in relation to an empirical formula.

### 6.1 Solubility of Gas in Liquids

The solubility of a gas in a liquid is governed by empirical Henry's law. It describes how the solubility of gas is dependent on external pressure. The solubility is also decreasing with increasing temperature. For a solution of gases in water the equilibrium constant is denoted  $K_h$ . For a gas  $A$  in equilibrium with water (a saturated solution), i.e.,  $A_g \rightleftharpoons A_{aq}$ , Henry's law states:

$$K_h = \frac{[A_{aq}]}{p(A_g)} = \frac{\text{molar concentration of gas in liquid}}{\text{partial pressure of the gas}} \quad (6.1)$$

Typical values for a solution in water are given in Table 6.1.

gas	$K_h$		$t/^\circ C$
Cl <sub>2</sub>	0,77	M/bar	25
H <sub>2</sub>	0,790	M/bar	25
O <sub>2</sub>	2,18	mM/bar	0
O <sub>2</sub>	1,71	mM/bar	10
O <sub>2</sub>	1,38	mM/bar	20

Table 6.1: Values of the equilibrium constant in Henry's law, with  $M$  the molar mass (mass per mole of substance).

The form of the equilibrium constant, Eq. (6.1), shows that the concentration of a solute gas in a solution is directly proportional to the partial pressure of that gas above the solution. Henry's law is found to be an accurate description of the behavior of gases dissolving in liquids when concentrations and partial

pressures are reasonably low, which is normally the case. As concentrations and partial pressures increase, deviations from Henry's law become noticeable. This behavior is very similar to the behavior of gases, which are found to deviate from the ideal gas law as pressures increase and temperatures decrease. For this reason, solutions which are found to obey Henry's law are sometimes called ideal dilute solutions.

## 6.2 Formation of Bubbles

An introduction to the phenomenon of bubble formation is presented in the following section. Firstly, and in more detail, the pressure aspects are discussed. Secondly, general remarks on other physical and thermodynamical causes is made.

### 6.2.1 Pressure Effects (cavitation)

The formation of bubbles (or cavitation) is an everyday phenomenon. Whenever liquid is present and is agitated in some manner bubbles might appear. Take, e.g., a ship propeller where cavitation is a problem as erosion reduces the life-span of the blades<sup>1</sup> and energy loss decreases efficiency (stalling).

The study of cavitation is somewhat similar to the measurement of tensile strength of solids. Suppose water is put into a cylinder sealed at one end with a piston. If the piston is pushed towards the liquid, with a force  $F$ , it will be under a positive pressure  $P = F/A$  where  $A$  is the area of the piston. By sign convention (see Fig. 6.1) forces on a fluid element are defined as

$$d\mathbf{F} = -Pds, \quad (6.2)$$

where  $ds$  is the surface element vector. In this 2D case  $ds = \hat{\mathbf{n}}dx$  or  $ds = \hat{\mathbf{n}}dy$  where  $\hat{\mathbf{n}}$  is the unit normal to a surface. A positive pressure in a fluid corresponds to a force pushing on liquid elements and vice versa.

Imagine as sketched in Fig. (6.1) that the piston is pulled. There is a force  $\mathbf{F} = (-F, 0)$  acting on the piston, the result of this action depends highly on the specific situation. If there is an air bubble present in the water it will expand and the piston will move (fall). As  $F$  increases the pressure in the bubble drops,  $P = P_0 - \frac{F}{A}$ , towards zero. The ideal-gas law

$$PV = nRT \quad (6.3)$$

predicts that the bubble volume will expand (a reasonable assumption is that  $nRT$  is constant) without limit.

Now, if there is no air bubble present in the water, the piston might for a small force  $F$  move a little distance down, and stay there. This displacement happens as the liquid can expand, it has a bulk viscosity  $\zeta$ , see Sec. 2.2. Normally the bulk viscosity is of little consequence because most fluids behave as if they

<sup>1</sup>Whenever the bubbles implode on the surface of the blades the influx of water (small jet) erodes the blades at the given place.

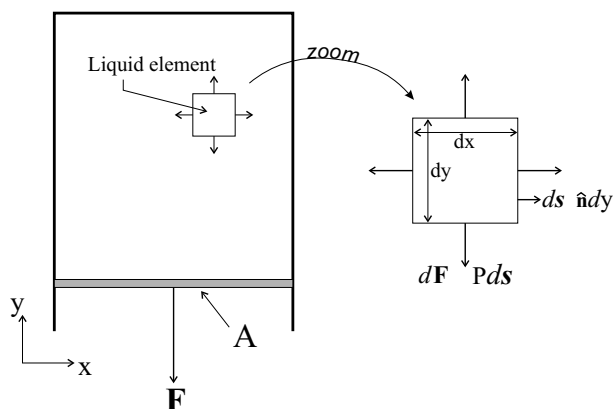


Figure 6.1: Negative pressure in a liquid  $P < 0$  results in a positive force on liquid elements, i.e., a positive normal stress as  $ds$  and  $d\mathbf{F}$  are pointing in the same direction.

were incompressible. Compressibility is introduced in the governing equations through the so-called dynamic pressure

$$P = P_0 + \zeta \nabla \cdot \mathbf{u}. \quad (6.4)$$

$P_0$  is the static pressure and  $\mathbf{u}$  is the velocity field in the liquid, see Chap. 2. For an incompressible fluid the conservation of volume requires  $\nabla \cdot \mathbf{u} = 0$  so that  $P = P_0$ . Hence, after the small expansion the liquid stays in a state of tension: there is a negative pressure ( $P = -\frac{F}{A}$ ) and hence positive normal stress in the liquid,  $\tau_{ii} = -P \hat{\mathbf{n}} = \frac{F}{A} \hat{\mathbf{n}}$ . As shown in Fig. 6.1 the normal stresses on a volume element are directed outwards (positive stress and negative pressure).

The state described above is only meta stable. If the force is increased further (still without the presence of an initial bubble) a bubble might form and lower the energy of the system (the piston falls). Before such a bubble can form the system has to overcome an energy barrier. Some simple physical considerations regarding the formation are presented in the following.

The bubble forms after nucleation, i.e., formation of a cluster of enough gas molecules being stable (generally about 10 molecules in diameter, Atkins [6]). The cluster should be big enough to withstand diffusion from its surface. It is very general that there is an energy barrier associated with nucleation. In our case the barrier arises as the liquid-gas transition is discontinuous (of "first order"). The barrier exists as the liquid-gas interface has a finite energy per unit area, the surface tension  $\sigma$ . The formation of a bubble with radius  $R$  hence costs

$$\Delta E_S = 4\pi R^2 \sigma \quad (6.5)$$

that is surface tension times area. And the work of the negative pressure over the bubble volume is

$$\Delta E_{PV} = \int_0^R P A dR = \int_0^R P 4\pi R^2 dR = \frac{4\pi}{3} R^3 P. \quad (6.6)$$

The total energy of formation being

$$\Delta E = \Delta E_V + \Delta E_S = 4\pi R^2 \sigma + \frac{4\pi}{3} R^3 P. \quad (6.7)$$

At negative pressures ( $P < 0$ ) in the liquid Eq. (6.7) has a global maximum for a critical radius  $R_c = \frac{2\sigma}{|P|}$ . The energy at  $R = R_c$  establishes an energy barrier (see Fig. (6.2))

$$\Delta E_B = \frac{16\pi\sigma^3}{3P^2}. \quad (6.8)$$

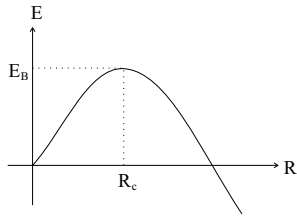


Figure 6.2: Energy barrier,  $\Delta E_B$ , the critical radius  $R_c$  needed to be overcome in order to create and expand a bubble.

At a given temperature  $T$  thermal fluctuations may enable the system to overcome the energy barrier  $\Delta E_B$ . The probability of such an occurrence is governed by the Boltzmann distribution

$$f(\Delta E_B) = \exp\left(-\frac{\Delta E_B}{k_B T}\right), \quad (6.9)$$

where  $k_B$  is the Boltzmann constant, Guénault [7]. This is the case as the Helmholtz free energy can be calculated by the Boltzmann distribution. Note that from Eqs. (6.8) and (6.9) a constant probability for decreasing temperatures would require the pressure to drop proportionally to  $-\frac{1}{\sqrt{T}}$ . But this is not physically correct, as there is a limit to the force with which one molecule can act on another. When the pressure reaches the finite "spinodal pressure" the fluid will stretch without limit.

After these considerations it is obvious that at only slightly negative pressures the liquid can exist a long time in a state of tension. The energy barrier  $\Delta E_B$  is large and the chance of formation is small. Though this state of negative pressure requires the liquid to be very clean. If the liquid contains dissolved gases the formation is much more likely. Bubbles also tend to form preferentially on walls or on dirt particles in the liquid (nucleation is easier). Bubble formation on walls or associated with dirt is called heterogenous nucleation. Whereas formation in the bulk of an ideal liquid is called homogenous nucleation.

### 6.2.2 Other Causes

The bubble formation due to pressure drops was presented in the previous subsection. The bubbles might also form due to chemical electrolysis effects at electrodes. Electrodes are, e.g., present in electroosmotic (EO) pumps used in microfluidic devices. Finally, heating of devices may cause bubbles to form: liquid might evaporate or dissolved gases condensate and expand.

## Chapter 7

# A Short Review of Microchannels

The previous chapters have developed many aspects of the bubble phenomenon. Focus has been put on liquid gas interfaces as well the physics of triple points. The theory has to some extent been applied to contracting channels (sudden and tapered). So far it has only been hinted that the surface tension effects actually are the prevailing forces when dealing with two-phase flows at microscale. The present chapter is meant as a link between the studied theory, actual channels used in microfluidic devices, and the simulations later discussed in Chap. 9 and Chap. 10. The chapter shortly reviews some basic characteristics as well as presents the bubble related problems described in this thesis. Obviously the short review nature of this chapter does not cover all aspects of the very wide subject of "Microchannels". Extremes such as highly viscous liquids, non-Newtonian liquids, specialized geometries, special fabrication methods, special materials, etc., may very well differ from the following generalities.

### 7.1 Dimensions

Dimensions of actual microfluidic devices vary over a broad range. Channel widths vary from a few micrometers to tenth of millimeters and depths from a few hundred nanometers up to a millimeter. The small devices are generally fabricated by etching silicon whereas the larger devices may be made as polymer structures.

At Mikroelektronik Centret (MIC) polymer structures are made in PMMA (polymethylmethacrylate) using laser ablation and hot embossing. This technique is fast, quite efficient, and cheap. The smallest channels are about  $10\ \mu\text{m}$  deep and  $50\ \mu\text{m}$  wide whereas large channels may easily be  $1000\ \mu\text{m}$  deep and several millimeters wide. One problem is that the small channels generally have Gaussian-like cross sections see Fig. 7.1. Wider channels are made up of several smaller channels cut side to side as illustrated in Fig. 7.2. Thus the channel cross section is more or less rectangular. The open channels are closed by bonding a lid on top.

Roughness appearing in polymer channels may have length scales up to 10% of the actual channel width/height (information most kindly provided by

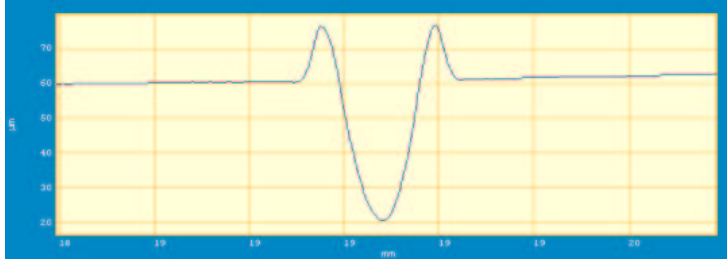


Figure 7.1: A scanned cross section of an actual microchannel made in PMMA. The channel is  $50 \mu\text{m}$  deep and  $200 \mu\text{m}$  wide. The figure is most kindly provided by Martin F. Jensen, MIC and Teknologisk Institut, [46].

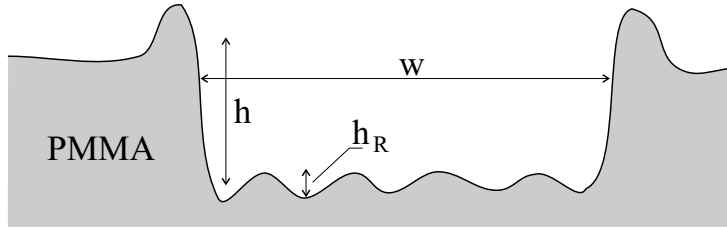


Figure 7.2: Cross section of a wide microchannel. The channel width  $w$ , channel height  $h$ , and roughness scale  $h_R$  are shown.

Teknologisk institut, [46]). Hence  $h_R < 0.1 h$  in Fig. 7.2. The specific nature of the roughness and the quality of the channel structures depend on the material properties of the polymer used.

## 7.2 Physical Characteristics

Flows in microfluidic devices are driven by pumps (e.g., electro osmotic or mechanical) delivering pressures from a few Pascals to several thousand Pascals. Typical mean flow velocities vary from a few millimeters per second to many centimeters per second. Corresponding to volumetric flow rates of, e.g., 1 to  $10 \mu\text{l s}^{-1}$  in channels with  $50 \times 200 \mu\text{m}^2$  cross sections, Chang *et al.* [47].

To illustrate the properties of microflows, regimes for the dimensionless numbers, introduced in Sec. 3.6, are presented in the following. The case of water at 300K ( $\sigma = 0.0725 \text{ J m}^{-2}$ ,  $\rho = 10^3 \text{ kg m}^{-3}$  and  $\mu = 10^{-3} \text{ Pa s}$ ) is used as an example,

$$10^{-5} < Ca \equiv \frac{\mu U}{\sigma} < 10^{-2} \quad \text{with} \quad 10^{-3} \text{ ms}^{-1} < U < 10^0 \text{ ms}^{-1} \quad (7.1)$$

$$10^{-2} < Re \equiv \frac{UL}{\nu} < 10^1 \quad \text{for} \quad L = 10^1 \mu\text{m} \quad (7.2)$$

$$10^0 < Re \equiv \frac{UL}{\nu} < 1000 \quad \text{for} \quad L = 10^3 \mu\text{m} \quad (7.3)$$

$$10^{-5} < Bo \equiv \frac{\rho g L^2}{\sigma} < 10^{-1} \quad \text{with} \quad 10^1 \mu\text{m} < L < 10^3 \mu\text{m} \quad (7.4)$$

$$\text{and } \Delta_c \equiv \sqrt{\frac{\sigma}{\rho g}} \approx 2.5 \times 10^{-3}. \quad (7.5)$$

The above characteristic  $Bo$  and  $Ca$  numbers confirm that the surface tension related forces are dominating gravity and viscous forces, respectively. Moreover the Reynolds number confirms that flows in microchannels generally are laminar. Transitional Reynolds numbers are classically about 2000 or 2300, but in the microfluidic case new assumptions have to be made, Gravesen *et al.* [48].

### 7.3 Problem Areas

As illustrated above, but also mentioned earlier, the presence of bubbles in microchannels may be problematic as surface tension related forces are dominating. If they do not have a specific purpose bubbles should be avoided. From the theory discussed in Chap. 5 it is evident that the pressures needed to move a bubble in a channel of radius  $r$  is geometry (curvature) and friction related. The friction part is proportional to  $\alpha/r$  where  $\alpha$  is a material specific parameter. The geometry related part is non-zero as soon as the tube radius changes (given by the contact angle description and the Young-Laplace equation). This last part is proportional to  $\sigma/r$ . The resulting blocking or clogging pressures may be of several thousand Pascals.

Even if gas bubbles can be totally avoided in operational microfluidic devices the surface tension effects still have a practical relevance in the initial filling of the device.

Investigating geometrically related properties of devices is thus very important. A microsystem might be ruined by only one problematic geometric feature. Analytical work and simulations hence play key roles in the development of actual devices. It is far less expensive and less time consuming to make a simulation than to fabricate and test a possible defect device.

### 7.4 Removing Bubbles

If bubbles are present in microfluidic devices several active methods may be used to remove them. They are here listed and shortly commented:

- Degassing: Removing bubbles or dissolved gasses by chemical or physical means.
- Control of surface tension: Influencing the behavior of bubbles by influencing their interfacial surface tension by use of electric fields, temperature gradients or surfactants.
- Vibrations: Methods involving the use of high frequent sound induced vibrations have also been suggested as means of dealing with clogging bubbles.
- Bubble traps: During the work with the thesis a passive method to handle the bubble problem was devised. The idea is to trap the bubbles at specific locations within the given microsystem. The pressure drop associated with more or less curved surfaces, described by the Young-Laplace equation, is utilized in a positive way.

Basic ideas behind the passive bubble trap are further discussed in Sec. 9.5, where a specific bubble trap device is modelled using the commercial CFD-ACE+ software. The trap is used as one of the simulation examples of Chap. 9.

## Chapter 8

# Commercial Software

The problems and envisioned solutions described in the previous chapter will, in the following parts of the thesis, be addressed using the commercial simulation program CFD-ACE+ [53] in combination with theoretical results and home designed MATLAB programs. It is thus important to have an understanding of CFD-ACE+ as it is going to be utilized to investigate/illustrate physical phenomenon related to flows in microchannels in the presence of bubbles. The present chapter presents the actual software and models whereas actual examples of phenomenon are given in the following simulation chapters.

CFD-ACE+ is a commercial multi-physics program package providing geometry, grid generation, solver, and visualization facilities all on a graphical user platform. The package includes the following applications:

- CFD-GEOM: geometry and grid generation.
- CFD-GUI: solver set-up interface.
- CFD-ACE(U): the solver/engine.
- CFD-VIEW: results viewer (post processing).

The CFD-ACE(U) solver includes several physical modules for, e.g., heat flow, turbulence, plasma, etc. In the current thesis only the flow and the free surface VOF (Volume-Of-Fluid) modules are used. The later VOF module is of special interest in this thesis as it enables the simulation of gas bubbles within a given liquid. Thus it is important with an insight in its implementation and especially its handling of the surface tension effects as well as solid boundary conditions, e.g., specification of contact angle.

Manuals are, of course, provided with the software. They are describing the applications (user interfaces, etc.) as well as including some numerical and physical considerations. The specific physical models are presented and relevant references are provided. Moreover the CFD-ACE+ license provides a support facility where an e-mail correspondence with the program developers is possible.

The two following sections present the flow and VOF modules and point out problems and issues where to be cautious. The third presents a small listing of bugs. At last the CFD-ACE(U) solver is tested on several cases.

## 8.1 The Flow Module

The flow module is the core element of the CFD-ACE(U) solver and is generally used in most applications of the CFD-ACE+ package. The module is intended for simulating almost any gas or liquid flow within a certain geometry. It finds the velocity and pressure field by solving the relevant momentum and mass conservation equations, i.e., the continuity equation and the Navier-Stokes equations. The equations are solved within the geometrical restraints with appropriate boundary conditions. CFD-ACE(U) solves the equations by a finite volume method, which consists of the following steps:

- Formal integration of the governing equations over all grid cells (control volumes).
- Discretization of the integrated equation involving finite difference like schemes. Each type of flow term in the equations are handled specially, i.e., transient (evolution in time), convection, diffusion, and source terms. The integral equations are hereby converted into a system of algebraic equations.
- Solution of the algebraic equations by iterative methods and ensuring correct linkage between pressure and velocity field.

It is here worth noticing that the first formal integration step results in an exact expression for the conservation of relevant physical quantities. This clear relation between numerics and underlying physical conservation laws is one of the main strengths of the finite volume method<sup>1</sup>. Hence the rate of change of a quantity in a control volume is the sum of the net flux due to convection and diffusion into the control volume, and the creation of the quantity in the volume. The velocity-pressure coupling is carried out through the mass conservation equation in an iterative procedure. In CFD-ACE(U) the so-called SIMPLEC<sup>2</sup> correction algorithm is used for the iterative purpose.

### Solver Settings

In the CFD-GUI it is possible to tune on several numerical parameters influencing the solution convergence. Additionally several output options are available. The numerical parameters are:

- Maximum iterations: The number of iterations allowed.
- Convergence criterion: The minimum reduction in residual for each variable (e.g., 0.0001 is four orders of magnitude).
- Minimum residual: A minimum residual at which to brake the iteration procedure (if previous criterion is not applied).
- Inertial relaxation: Under-relaxation parameters for the velocity and pressure correction equations. Increase the value adds stability at the cost of slower convergence.

---

<sup>1</sup>This concept of clarity is very clearly presented in a very good introductory book on the subject by Versteeg and Malalasekera [39]

<sup>2</sup>Semi-Implicit Method for Pressure-Linked Equations Consistent

- Linear relaxation: Under-relaxation for the linear pressure scheme. Decreasing the value adds stability at the cost of slower convergence.

The residuals are discussed below. The under-relaxation parameters are used to constrain the change in a variable from iteration to iteration, preventing divergence of the solution. Generally the default parameters are suitable though experience shows that when including the VOF module the inertial relaxation should be increased. The maximum iterations should at least be set to 40 or 50.

Furthermore it is possible to choose the specific numerical spatial difference schemes used. It is also possible to choose the given solver, e.g., preconditioning method, pressure-velocity coupling method, etc.

### Residuals

The convergence of a solution can be assessed by monitoring the residuals during the iteration process. In the present case the relevant parameters are pressure and velocity field. In a time dependent simulation the development of the residuals are presented at every time step. The rate of change of a residual  $R$  is in the CFD-GUI plotted as function of the iteration count  $i$ . The residual  $R_i^n$  at iteration  $i$  and time step  $n$  (that is time dependent) of a generic variable  $\phi$  is defined as,

$$R_i^n = \sum_{\text{all cells}} |\phi_i^n - \phi_{i-1}^n|. \quad (8.1)$$

The residuals are in CFD-ACE(U) not normalized by, e.g.,  $\phi_i^n$ . Convenient convergence criterion are thus given in the rate of change of a residual (the number of decades it decreases) and not by a given lower bound. The definition of the residual is unfortunately not given in the CFD-ACE+ manual, but was obtained through the e-mail support facility.

## 8.2 The VOF Module

The VOF module includes free surface capabilities in the CFD-ACE(U) engine. It allows for the simulation of a mixture of two incompressible and immiscible fluids including surface tension effects. The basis of the VOF interface tracking method was presented in 1980 by Hirt *et al.* [40], but recently extended in 1995 by Rider *et al.* [41]. Latest in 1996 Rider *et al.* [42] have made great progress in including the surface tension effects in a more consistent manner. The VOF method used in CFD-ACE+ is mainly based on these last two articles. The research made in the VOF algorithms has a great history and is still in progress at the Los Alamos National Laboratory in the US. The performances of the VOF method compared to other surface tracking models are presented in an article by Rider and Kothe [43]. It is made clear that the latest VOF algorithms are very powerful tools and are still extendable.

Now, assuming that the two fluids involved are a liquid (e.g., water) and a gas (e.g., air) the essential features of the VOF interface tracking method are as follows: the distribution of liquid and gas within the computational grid is accounted for using a single valued scalar variable  $F$ .  $F$  specifies the volume fraction of liquid in gas in a given computational grid cell. Hence if  $F = 1$  a cell is full of liquid, if  $F = 0$  a cell is full of air, and in a cell containing an interface  $0 < F < 1$ .

In a computation an initial prescribed interface topology (initial condition) is first used to compute fluid volume fractions  $F$  in each computational cell. This requires a calculation of the volumes divided by the interface in each cell. The exact interface information is then neglected in favor of the scalar information lying in  $F$ . The evolution of  $F$  is then governed by a transport equation,

$$\frac{\partial F}{\partial t} + \nabla \cdot (\mathbf{u}F) = 0, \quad (8.2)$$

being solved together with the momentum and continuity equations. The new interface topology is then inferred and reconstructed solely based on the local information lying in  $F$ . Several reconstruction schemes are available. Though the effects of surface tension require the use of the most advanced scheme: the piecewise linear interface construction (PLIC) method. In the PLIC scheme the liquid-gas interface is assumed to be linear (planar in 3D) and can take any orientation within a cell. In Fig. 8.1 approximate  $F$  values are given in every cell together with the linear surface approximation. The reconstruction is required at every time step to include the necessary back-coupling of surface forces to the momentum equations as well as flux calculations. The use of the VOF surface tracking together with the PLIC reconstruction method maintains the interface completely in a one cell layer, Rider *et al.* [41].

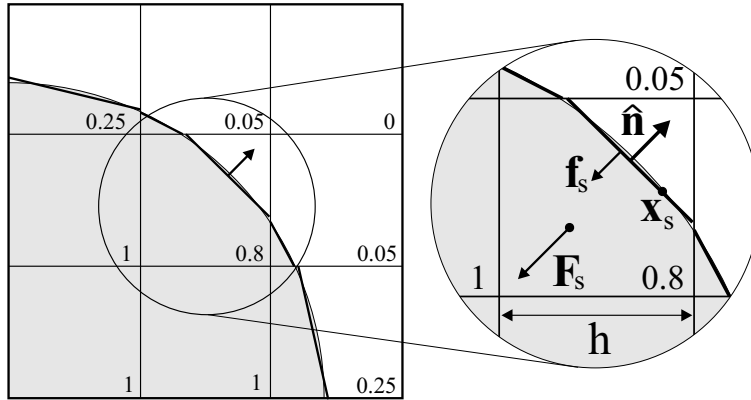


Figure 8.1: An example of a reconstruction of a circular arc (grey region) using the PLIC approximation of piecewise linear interfaces in each computational cell. Further a zoom is made of one cell where the components of the CSF surface physics model are included: surface force  $\mathbf{f}_s$ , CFS volume force  $\mathbf{F}_s$ , surface normal  $\hat{\mathbf{n}}$ , cell dimensions  $h$ , and surface point  $\mathbf{x}_s$ .

The physical effects localized at the fluid interface are modelled by the continuum surface force (CSF) method. This part of the VOF module is of significant interest in relation to the bubble problems at hand. The CSF method can in principle handle all surface processes, e.g., surface tension (of course), gradients in surface tension (Marangoni effects), phase changes, etc.<sup>3</sup> The given

<sup>3</sup>The CSF method was originally developed for surface tension. However the basic approach of the CSF method lends itself well to interface physics in general, i.e., surface phenomenon other than surface tension can be encapsulated in the CSF model, Rider *et al.* [41].

surface process is applied to all surface cells and replaced by a volume process having an integral reproducing the desired effect.

As an example of the CFS model, surface tension forces are reformulated as a volume force  $\mathbf{F}_s$  satisfying,

$$\lim_{h \rightarrow 0} \int_{\Delta V} \mathbf{F}_s(\mathbf{x}) dV = \int_{\Delta S} \mathbf{f}_s(\mathbf{x}_s) dS, \quad (8.3)$$

where  $\mathbf{x}_s$  is a point on the surface,  $\Delta S$  is the portion of the surface lying within the small volume  $\Delta V$ , and  $h$  the grid size. See the "zoom" on Fig. 8.1 for details. The surface tension force  $\mathbf{f}_s$  is given as

$$\mathbf{f}_s(\mathbf{x}_s) = 2\sigma H(\mathbf{x}_s) \hat{\mathbf{n}} + \nabla_s \sigma, \quad (8.4)$$

where  $\nabla_s$  is the surface gradient. The first term is the normal force and the second is the tangential force, i.e., Marangoni effect. In CFD-ACE+ the tangential forces occur when  $\sigma$  is made temperature dependent by use of the heat transfer module. The surface mean curvature is given through the surface normal as

$$H(\mathbf{x}_s) = -\nabla \cdot \hat{\mathbf{n}}. \quad (8.5)$$

The above formulation of the surface tension reduces to

$$\mathbf{F}_s = \mathbf{f}_s \delta_s \quad (8.6)$$

where  $\delta_s$  is a delta function.  $\delta_s$  is basically a function being zero in all cells not containing an interface and introduces a suitable weighting in cells containing an interface. As the product  $H h \rightarrow 0$  the line integral of  $\mathbf{F}_s(\mathbf{x}_s)$  should yield the Young-Laplace pressure jump  $2\sigma H$ . As Rider *et al.* [42] point out it remains an open question whether or not the CSF should be coupled to the momentum equations exactly as a body force.

Some issues in the current state of development of the CSF method need to be addressed further. The exact definition of the surface delta function and the proper discretization of  $H$  and  $\hat{\mathbf{n}}$  are still open questions. Within the area of this thesis the correct definition of triple points at solid boundaries should be investigated in further details. Still, the CSF formalism presents characteristics that surely allow for interesting developments in the future.

The VOF and CSF models in the current CFD-ACE+ version are mainly based on the work presented by Rider *et al.* [41, 42]. Incorporation of surfactants in the CSF model is, e.g., presented in an article from 2001 by Renardy *et al.* [44]. Improved techniques for handling the surface tension and especially for determining the curvature are also available, e.g., by higher order polynomial approaches.

### Solid boundaries

Of great interest are the boundary conditions at the contact line on solid walls. In the current CFD-ACE+ version it is only possible to specify a given static contact angle. This is implemented numerically by specifying a given surface normal  $\mathbf{n}_b$  in the computational cells at the boundaries. The effects of moving contact lines, i.e., dynamic contact angles and wetting phenomenon are not modelled properly with this lone condition, Rider *et al.* [42, 41]. Furthermore

neither local solid boundary conditions (roughness and surface chemistry) nor local flow conditions (velocity, viscosity) are currently properly incorporated.<sup>4</sup>

The limitations in the specification of the wall condition can also create problems in simulations. Whenever a liquid-gas interface approaches a solid wall and enters a wall cell the surface normal  $\mathbf{n}_b$  is defined in that cell. This may give rise to false wall adhesion effects. Moreover problems arise at solid wall when the Marangoni effects are incorporated. A false gradient in  $\sigma$  appear in wall cells;  $\sigma$  is set to zero within the wall.

A positive aspect of the VOF model lies in its capability of indirectly having a high resolution of wall wetting films. This is the case when a non-wetting wall condition is chosen. Because of the way the  $F$ -function defines an interface it is possible to have an effective higher resolution than the grid dimension  $h$ . An illustrative example is given in Figure 8.2 where a wetting layer of thickness  $h_0 = Fh < h$  is presented.

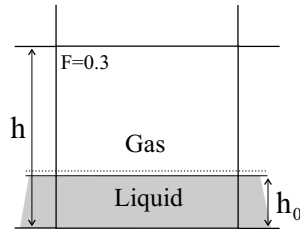


Figure 8.2: The VOF model is capable of an effective higher resolution than the grid dimension  $h$ . The liquid layer has a thickness  $h_0 = Fh$ .

Still the flow in the film is only represented by one velocity over the thickness  $h_0$ . More comments and examples of these effects are given in the following simulation chapters.

### Time-Stability

There are two time step stability conditions related to the VOF module. First of all stability of the solution algorithm requires that an interface does not cross more than one cell in a time step  $\delta t$ . The so-called CFL number, for a given cell, defined by

$$\text{CFL} = \frac{|v|\delta t}{h}, \quad (8.7)$$

specifies the distance crossed by an interface travelling at velocity  $v$ , as a fraction of local cell length scale  $h$ . Time-steps should thus be chosen as,

$$\delta t < \delta t_c = \text{CFL} \frac{h_c}{|v_c|}, \quad \text{CFL} < 1, \quad (8.8)$$

where  $c$  runs over all interface cells in the computational grid. Generally it is necessary to choose the CFL number less than 0.2. In the CFD-ACE(U) solver an automatic time step option automatically ensures stability.

Secondly the introduction of surface tension in the CSF model having the explicit back coupling to the momentum equations yields another restriction. The maximum allowable time step  $\delta t_\sigma$  to resolve the propagation of capillary waves requires

$$\delta t < \delta t_\sigma \propto \frac{h^{3/2}}{\sigma}. \quad (8.9)$$

<sup>4</sup>The new 2002 version of CFD-ACE+ is expected to include a surface chemistry package.

The above factor is defined by Rider *et al.* [42]. The factor is related to the oscillation period of capillary waves. By use of the simple dispersion relation given in the later Eq. (8.12) it is found that  $\delta t_\sigma \propto \sqrt{\rho/\sigma}h^{3/2}$ ; numerical practice states that the maximally allowed wave number  $k_w$  is given by  $k_{w,\max} = \pi/h$  where  $h$  is the grid size. Typically  $\delta t_\sigma$  is a little smaller than  $\delta t_c$ . Though  $\delta t_c$  can be kept as upper bound for  $\delta t$  by introducing some numerical damping of capillary wave. The viscosity is increased artificially in cells adjacent to surface cells.

### Grid

The generation and choice of the calculation grid (made with CFD-GEOM) are generally of great importance in CFD, but especially when using the VOF free surface module.

Firstly, a general rule-of-thumb when increasing the grid resolution in every direction by a factor 2 the calculation time will, in a 2D grid, increase by a factor  $2 \times 2 \times 2 = 8$ . This is because the number of cells increase by  $2 \times 2$  and as the cell dimensions decrease by a factor 2 the time step does too, following Eq. (8.8).

Secondly, an implication of the geometric handling of the surface (PLIC reconstruction), the grid quality will influence the solution quality. In regions where the interface pass the influences are:

- Orthogonality: Directly affects the accuracy of flux calculations.
- Smoothness and Aspect Ratios: Affects the accuracy of the surface reconstruction.

According to the CFD-ACE+ manual aspect ratios above 10 should be totally avoided. The ideal grid is hence a square or cubic grid. The number of cells needed to resolve the shape of interfaces is also important. Likewise CFD-ACE+ recommends a minimum of 8 cells to resolve a gap. The restrictions given on the grids and the fact that merged grids are not handled by the VOF module yield some limitations. It is hard to increase the resolution of some parts of the calculation area without increasing the overall resolution.

Grid considerations and grid dependency of solutions are of course going to be discussed in the simulation chapters and specially in the test case section below.

### VOF-Solver Settings

When using the VOF module it is possible to activate two "numerical" options. Firstly, a removal of flotsam and jetsam, i.e., removal of small erroneous gas or liquid droplets that may arise in excessively skew grids. Secondly, the surface capillary waves damping option can be activated. This option is quite useful when un-physical initial conditions are stipulated, e.g., square bubbles. It prevents long term oscillations of the liquid surface as it deforms to a physically correct bubble.

## 8.3 Bugs

During the course of the project a few bugs and minor errors have been noticed in the CFD-ACE+ package. In the following they are listed:

1. When the VOF module is in use problems can arise when specifying the initial liquid-gas distribution. If two geometries overlap in the specification, e.g., a square and a circle gas area in a liquid, small liquid droplets appear within the gas region. This behavior arises because of the way surfaces are defined through the volume fraction  $F$ -function. Specification of more physically correct initial conditions are hereby complicated. When the solver deforms a non-physical geometry to a physical one numerical errors might appear in the  $F$  distribution (so-called flotsam and jetsam) moreover the transformation can be time consuming.
2. In the initial conditions menu in the CFD-GUI it is possible to import previously simulated data as a new initial condition. It is however not possible to change the boundary conditions. The solver keeps the old boundary conditions, even though the user seems to change them.
3. If the Marangoni effect option is selected together with partial wetting conditions ( $0^\circ < \theta < 180^\circ$ ) erroneous tangential effect appear at solid walls. This last bug is discussed further in the static meniscus test case below.

Together the first two bugs are quite inconvenient as it would, e.g., be nice to create a "natural" bubble and use it as an initial condition in several different runs.

## 8.4 Test Cases

It is good CFD practice to test the reliability of the solver/engine on simple test cases. Firstly, the CFD-ACE(U) solver is tested on a 2D and a 3D pure flow example. The numerical results are compared to theoretical results and a grid analysis is carried out. Furthermore a simple static 2D interface is examined. All relevant data is presented in Excel sheets in Appendix H.

### 8.4.1 2D Couette Flow

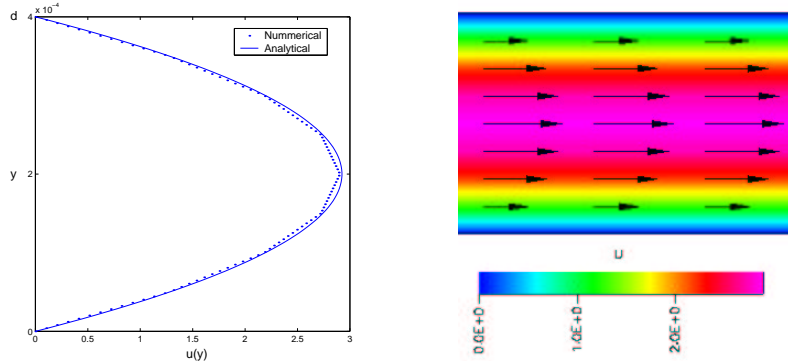
To introduce the test cases the simple 2D pressure driven flow between two stationary parallel plates is investigated (Couette flow). The plates are at a distance  $d$  and the pressure drop  $\Delta P$  is over the length  $L$ . The parabolic velocity profile of the flow is presented in Appendix B. The problem is steady state. The solution dependency with respect to grid resolution and convergence criteria (residual) is investigated.

$$\text{Data: } d = 400 \mu\text{m}, L = 1600 \mu\text{m}, \Delta P = 200 \text{ Pa}, \rho = 1003 \text{ kg m}^{-3}, \\ \mu = 8.55 \times 10^{-4} \text{ kg(sm)}^{-1}.$$

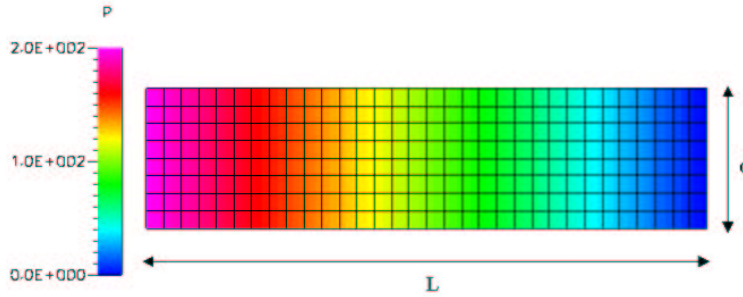
An example of the simulation results is presented in Fig. 8.3.

#### Conclusion

The simulations show good agreement with the theoretical results. Using the finest grid and the strongest convergence criterion the deviation in the mean velocity  $U$  is less than 1%. Though the simulation time was about 50 minutes. The results show the typical grid dependency and convergence behavior. The



(a) Theoretical and simulated velocity profile. (b) Simulated velocity profile as a scalar. The data is imported in MATLAB using the "line- vector plot (snapshot from CFD-VIEW). plot" command in CFD-VIEW.



(c) The figure shows the coarsest calculation grid (Grid 1) and the pressure profile. The pressure is linearly decreasing in the flow direction.

Figure 8.3: An example of simulations results of the Couette flow. The results are for the coarsest grid ( $8 \times 32$  cells and  $h = 50 \mu\text{m}$ ), but finest residual condition ( $R < 10^{-4}$ ).

solution is more exact for finer grids though the number of iterations needed to reach the convergence criterion is higher. It should be pointed out that the grid cells are chosen square as this is required when using the VOF module.

### 8.4.2 Poiseuille Flow

As a second test the Poiseuille flow in a cylindrical tube of radius  $a$  and length  $L$  is chosen. The theoretical description is presented in Appendix B. Even though this flow is not as relevant as the above 2D case it is used to illustrate some of the properties of CFD-GEOM and CFD-ACE(U), and as a reliability test. Grids with three different orthogonality properties are used to mesh the circular cross section of the pipe. The properties of the three grids in Fig. 8.4 are listed on the Poiseuille flow Excel sheet in Appendix H.

$$\text{Data: } a = 150 \mu\text{m} \quad L = 900 \mu\text{m}, \quad \Delta P = 100 \text{ Pa}, \quad \rho = 1003 \text{ kg m}^{-3}, \\ \mu = 8.55 \times 10^{-4} \text{ kg(sm)}^{-1}.$$

An example of a simulation using grid 1 is presented in Fig. 8.5. Note the positioning of the  $r$ -axis. It is placed where data, for the comparison in velocity profiles, is collected.

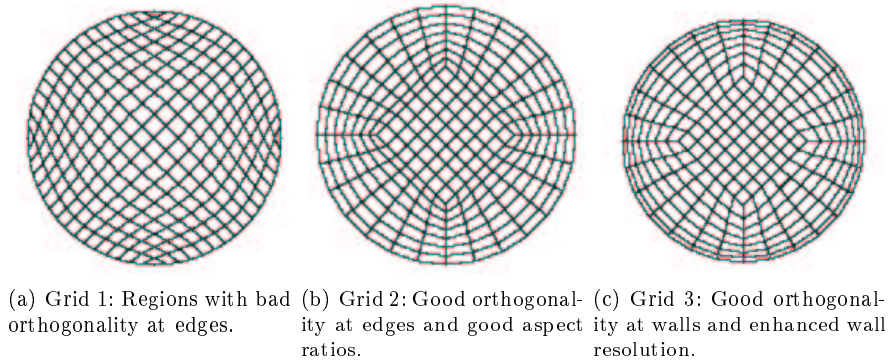


Figure 8.4: The three grids used in testing CFD-ACE(U) on the Poiseuille flow.

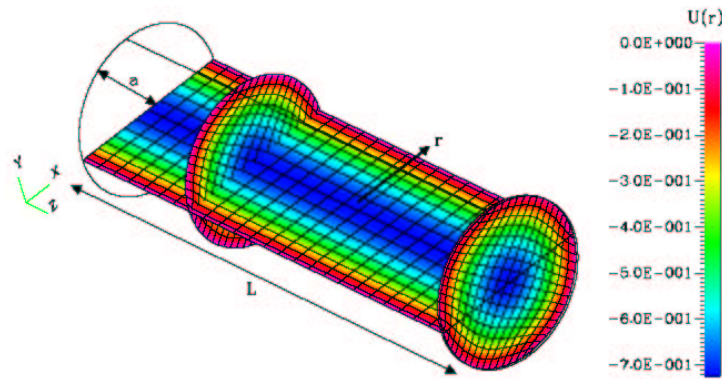


Figure 8.5: Simulation of the flow in a cylindrical tube of length  $L$  and radius  $a$ . Three cut planes are placed where the axial velocity,  $u_z(r)$  represented.

**Conclusion**

Generally all three grids reach the desired solution, within an acceptable margin of error ( $\approx 3\%$ ), in a small number of iterations. However, it is important to be aware that with an increasing number of iterations the solution seems to worsen. The measure given by the mean and maximal velocity are not solely indicative of the correctness of a solution. The overall measure of the residuals should also be considered. They decrease drastically with an increasing number of iterations. Firstly, it is important to determine the quantity being representative of a correct solution. Secondly, a seemingly correct solution may be due to luck.

In the present case it should be remarked that grid 1 has a lower number of cells than grid 2 and 3. Identical number of iterations are hence not directly comparable. The results are generally speaking satisfactory and comply with theory. It is here already clear how numerical results should be apprehended with a certain amount of scepticism.

### 8.4.3 2D Static Interface

This third test case is very relevant in relation to the thesis. The VOF module is activated and a free surface is introduced. A flat interface is initiated and set to reach a natural static position with a given static contact angle  $\theta$  as wall condition, see Fig. 8.6. The dynamics of the problem are only controlled by the surface tension as no external driving pressures or velocities are applied. The test is intended to give insight in some of the basic numerical problems that may arise when using the VOF module.

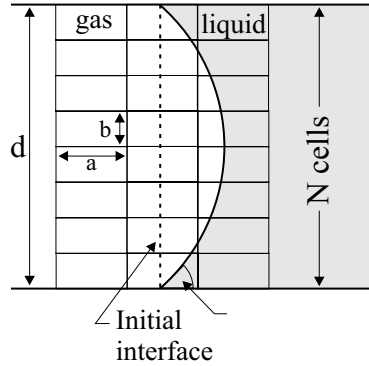


Figure 8.6: Simulation set-up where the initial interface is represented as a dotted line. Static contact angle  $\theta$ , cell dimensions  $a$  and  $b$ , channel width  $d$ . The cell aspect ratio is defined as  $a/b$  and the resolution over the channel width is  $N$ .

The pressure jump over the interface  $\Delta P_i$  is used for means of evaluating the simulation and is compared to simple theoretical results. Three contact angles  $\theta = 30^\circ$ ,  $\theta = 50^\circ$ , and  $\theta = 70^\circ$  are used. Focus is set on the solution dependency with respect to the grid and especially surface damping of interface capillary waves. All relevant data is found in the 2D Static Interface Excel sheet in Appendix H. Track of  $\Delta P$  is kept in time using the "Monitor Point" option in CFD-GUI, the data is stored in a .MON file. The pressure over the liquid-gas interface is readily found using the Young-Laplace equation,

$$\Delta P_i = \sigma \left( \frac{1}{R_1} + \frac{1}{R_2} \right) = \sigma \frac{2 \cos \theta}{d}, \quad (8.10)$$

where the 2D nature of the problem imposes  $R_2 = \infty$ .

$$\begin{aligned} \text{Data: } d &= 300 \mu\text{m}, \rho_{\text{liquid}} = 1003 \text{ kg m}^{-3}, \rho_{\text{gas}} = 1.16 \text{ kg m}^{-3}, \\ \mu_{\text{liquid}} &= 1.00 \times 10^{-3} \text{ kg(sm)}^{-1}, \mu_{\text{gas}} = 1.85 \times 10^{-5} \text{ kg(sm)}^{-1}, \\ \sigma &= 7.25 \times 10^{-2} \text{ N m}^{-1}. \end{aligned}$$

#### Grid and Aspect Ratio

As the surface is deforming towards the natural position capillary waves on the interface appear (discussed further below). To decrease these oscillatory effects extra numerical viscosity is added around the surface. Oscillations persist after many time steps as seen in Fig. 8.7.  $\Delta P_i$  is found as an average over a number of time steps and the standard deviation determined.

For the lowest recommended resolution of  $N = 8$  cells the discrepancy between theory and simulations is less than 13%. With an increasing resolution the error drops. The error is seen to depend on the aspect ratio  $a/b$ , but also on the contact angle. This might be caused by some geometric implications: how

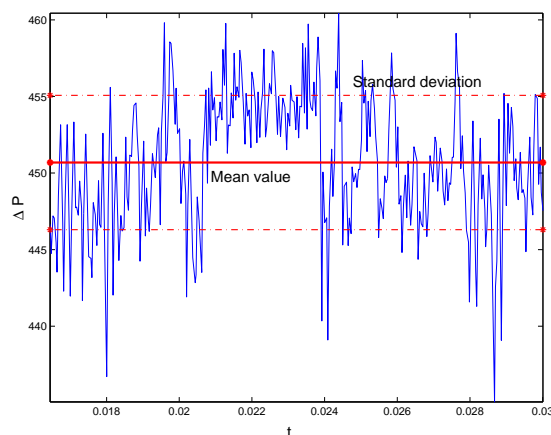


Figure 8.7: Time evolution of  $\Delta P_i$  for  $1.6 \times 10^{-2} \text{ s} < t < 3.0 \times 10^{-2} \text{ s}$  with  $N = 16$ ,  $a/b = 1$ . The mean value is found to be 451 Pa with a deviation of  $\pm 4$  Pa.

the interface lies in a given boundary cell, etc. The best results compared to calculation time are obtained for  $N = 16$  and  $a/b = 1$  with the use of extra damping. The calculation time was less than 25 min. An example of the final static meniscus is presented in Fig. 8.8.

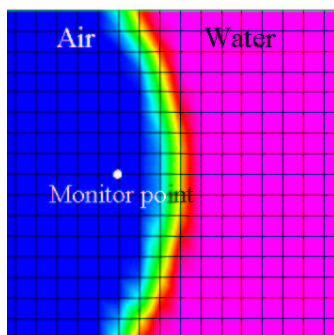


Figure 8.8: The static meniscus presented as a contour-like plot of the the  $F$ -function. Even though CFD-ACE(U) internally reconstructs the interface, as a piecewise linear curve, at every time step it is not possible to retrieve the information into CFD-VIEW. The smeared out aspect of the interface: it is only a contour plot of the  $F$  values. The point where the pressure data is collected is displayed.

### Capillary Waves

As mentioned the deformation of the meniscus gives rise to an oscillatory behavior of the interface, namely, surface tension induced capillary waves. These oscillations are in turn reflected in the time development of  $\Delta P_i$  as shown in Fig. 8.7. Moreover the calculation time is increased as the CFL condition, Eq. (8.8), reduces the time steps because of rapid oscillations of the interface. The oscillations are prevented by including the extra numerical viscosity around the interface. On a high resolution grid,  $N = 40$ , the actual calculation time varies from 45 min to 3 h for high and low damping, respectively.

To investigate the capillary waves on the interface their oscillation period  $T_n$  is compared with the simple sinusoidal theory period  $T_s$ . The dispersion relation for non-damped sinusoidal pure surface tension driven capillary waves,

Probstein [2], is given as

$$\left(\frac{\omega}{k_w}\right)^2 = k_w \frac{\sigma}{\rho}, \quad (8.11)$$

where  $\omega$  is the angular velocity,  $k_w$  the wave number,  $\sigma$  the surface tension and  $\rho$  the density of the liquid. Rearranging Eq. (8.11) yields

$$T_s = 2\pi \left( \left( \frac{2\pi}{\lambda_w} \right)^3 \frac{\sigma}{\rho} \right)^{-\frac{1}{2}}, \quad (8.12)$$

where  $T_s$  is the period and  $\lambda_w$  the wavelength. The wavelength is taken as the meniscus length

$$L_m = (\pi - 2\theta) \frac{d}{2 \cos \theta}. \quad (8.13)$$

In order to be thorough two different simulations with no surface damping are made: (1) keeping the original physical data, and (2) increasing the  $\sigma/\rho$  ratio by a factor 4. This should in turn yield a period half the original. The period is indirectly determined through the time evolution in the pressure jump. The two cases are shown in Fig. 8.9.

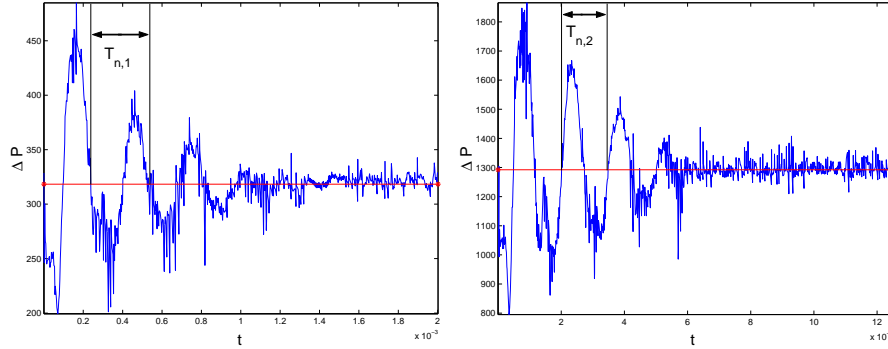


Figure 8.9: Time evolution of  $\Delta P_i$ . On the right figure the ratio  $\sigma/\rho$  has increased by a factor 4 compared to the left. The first period is named  $T_{n,1}$  and the second  $T_{n,2}$ .

In the first case the period was read of to be  $T_{n,1} \approx 3.1 \times 10^{-3}$  s and the theory showed  $T_{s,1} = 2.8 \times 10^{-3}$  s. In the second case  $T_{n,2} \approx 1.5 \times 10^{-3}$  s and  $T_{s,2} = 1.4 \times 10^{-3}$  s. Theory and numerics are seen to concorde rendering probable that the oscillations are of capillary nature. The large oscillations are hence physically predictable whereas the smaller high frequency oscillations might be caused by numerical instabilities. Via the introduction of the extra numerical viscosity the long period oscillations are reduced drastically. A better value for  $\Delta P_i$  is hence obtained faster. The numerical damping is thus very important as it is not very often possible to initiate the flow with physically correct liquid-gas interface shapes.

### Marangoni Bug

The present simple test was used in a last checkup on the VOF module. A simulation was started with the normal amount of surface damping and the

initial data however the Marangoni effect option was selected. In theory the results should not be affected as the surface tension remains constant. The simulation did nevertheless show a 100% deviation from theory and the previous results. The problem arises at the solid walls. Because no value for  $\sigma$  is given outside the liquid-gas region a large gradient appear in  $\sigma$  at the wall. This in turn introduces a large erroneous tangential force. This bug is of importance as the Marangoni effect option cannot be used when wetting wall conditions are being applied.

## Chapter 9

# 2D Simulations

Aspects of 2D two-phase flows and geometries are studied and compared with theory. The simple 2D nature ease the construction of examples and highly decrease computation time. Some of the cases investigated in the following have a nature of "numerical experiments". The intent is to gain insight into some of the features of the commercial CFD-ACE+ software. The 2D simulations do also yield a high amount of insight into specific bubble phenomenon and geometries. The simulations specifically provide knowledge needed for the formulation of design rules related to channel contractions.

The chapter deal with: (1) The dynamical behavior of bubbles moving in a straight channel is used to investigate capabilities of the free surface VOF module. (2) Generalized geometric features of channel contractions are illustrated by the sudden contraction and the tapered contraction. (3) A geometry having knobs at walls in used to model roughness. (4) Finally CFD-ACE+ is utilized to investigate the properties and efficiency of a novel bubble trap design.

In the subsequent sections a superscript  $N$  on a variable corresponds to the numerical/simulated value, e.g., the theoretical film thickness  $h_0$ , and the simulated film thickness  $h_0^N$ .

### 9.1 Straight Channel

The possibilities offered by the VOF module to simulate moving bubbles at relatively high capillary numbers are investigated in the following. Bearing in mind, as mentioned in Chap. 8, that the specification of boundary conditions at triple points is very limited in the CFD-ACE+ package. Basically it is only possible to prescribe a static contact angle  $\theta$ . The specific local or global flow conditions cannot influence on the solid wall condition. In turn it is important to be careful when handling simulations with great variety of flow conditions.

For a bubble in a straight channel the influence of the contact angle and especially the case of non-wetting bubbles ( $\theta = 0^\circ$ ) is investigated. The dependence, of the pressure drop over the bubble  $\Delta P_b^N$  as well as the thickness of the

wetting film layer  $h_0^N$ , with respect to the capillary number

$$Ca = \frac{\text{viscous forces}}{\text{surface tension forces}} = \frac{\mu U}{\sigma} \quad (9.1)$$

is of interest. Where  $U$ , in the following, is the speed of the bubble,  $\mu$  is the dynamical viscosity, and  $\sigma$  the surface tension. Moreover, the transient/convergence behavior of the solutions is an important factor from a computational point of view.

Firstly, the behavior of a non-wetting bubble is examined. A rather rough grid is utilized as it is intended to investigate the effective higher wall resolution described in Chap. 8. Secondly, the dependency on the choice of contact angle for a given flow regimes is investigated.

### 9.1.1 Wall Resolution and Flow Regimes

#### Initial Conditions and Set-Up

The behavior of a non-wetting bubble,  $\theta = 0$ , in a 2D channel of thickness  $d = 300 \mu\text{m}$  and length  $L = 4200 \mu\text{m}$  is considered. The initial set-up is depicted in Fig. 9.1.

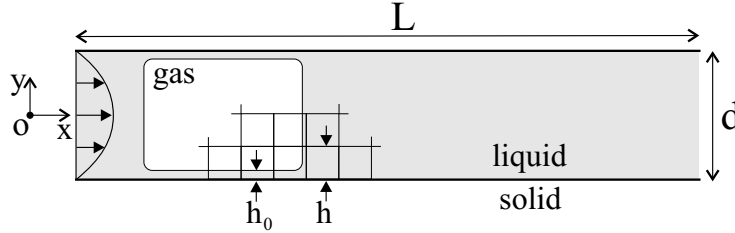


Figure 9.1: Geometry and initial setup for the wall resolution simulation. Grid dimensions  $h = 25 \mu\text{m}$ , approximate wetting layer thickness  $h_0 < h$ , tube length  $L = 4200 \mu\text{m}$ , and tube diameter  $d = 300 \mu\text{m}$ .

An initial un-physical square gas area is placed at the end of the tube. The surface damping property is chosen as the gas bubble obviously will deform drastically in the beginning of the simulation. A parabolic Couette flow velocity distribution is used as the left boundary condition (see Appendix B). The use of a well defined velocity distribution has several advantages. (1) The transient development of a pressure driven velocity profile is avoided. (2) The mean flow velocity of the liquid  $v$  is known in advance rendering the data collection simpler.

#### Grid and Cell Choice

The present simulations include capillary numbers  $Ca < 0.02$ . In order to illustrate the effective wall resolution effects the cell dimension  $h$  should be greater than the wetting film thickness. An initial run was made for  $Ca \approx 0.02$  where it was found that  $h_0 < 20 \mu\text{m}$ . Cells are made square and the number of cells over the channel  $N$  is set to 12 implying  $h = 25 \mu\text{m}$  with a total number of  $12 \times 168 \approx 2 \times 10^3$  cells.

#### Data and Transient Behavior

A series of eight simulations is made with the mean flow velocity  $v$  varying

from  $0.01 \text{ m s}^{-1}$  to  $1 \text{ m s}^{-1}$ .<sup>1</sup> For each simulation  $\Delta P_b^N$ ,  $u^N$ ,  $h_0^N$ , and  $Ca$  are found. All the data is presented in the "2D Bubble in Tube" Excel sheet found in Appendix H, section 4.

The data is retrieved when a steady state solution is reached. The solution is defined as converged when  $\Delta P_b^N$  does not vary in time. In the worst case the simulation took about 40 min the actual calculation time depends on  $v$ . For small  $v$  and hence small pressure drops the situation is delicate: variations in  $\Delta P_b^N$  due to capillary wave oscillations are of the same order of magnitude as the actual expected pressure drop ( $\approx 5 \text{ Pa}$ ).

For the case of the wetting layer thickness  $h_0^N$  the situation is however simpler. Remember,  $h_0^N$  is found as the cell dimension  $h$  times the volume-of-fluid function value in the given wall cell  $F_{\text{wall}}$  (previously illustrated in Fig. 8.2). The  $F_{\text{wall}}$  values stabilizes much faster than  $\Delta P_b^N$ . Basically, the near wall interface is quite restricted in moving. The problematic wall boundary conditions force the interface to be parallel to the wall in wall cells. Continuity defines the film thickness: the liquid area swept away by the bubble plus the flux in the film must equal the average speed  $v$  in front and behind the bubble times the channel width  $d$ . Assuming  $h_0 \ll d$  yields

$$1 - w = \frac{v}{u} = \frac{d - 2h_0}{d}. \quad (9.2)$$

where the amount  $wu$  corresponds to the excess speed of the bubble compared to the mean flow velocity  $v$ .

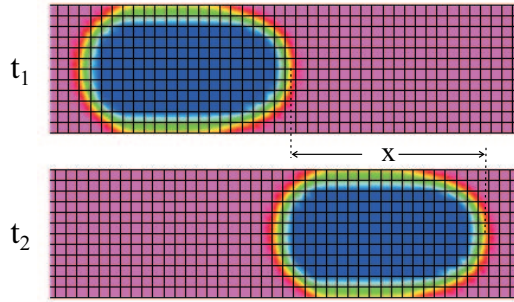


Figure 9.2: Example of a moving bubble displaced  $\delta x$  during the time  $\delta t = t_2 - t_1$ . The figure depicts the  $F$ -function values. Blue is  $F = 0$  and purple is  $F = 1$ .

The bubble speed  $u$  is defined as  $\delta x / \delta t$  where  $\delta x$  is the change in bubble position from time  $t_1$  to  $t_2$  and  $\delta t = t_2 - t_1$ , see Fig. 9.2. The error associated with this "manual" method to find  $u$  is about  $\pm 5\%$ .

## Results

The motion of the bubble shows the right characteristics in view of the 3D theory presented in Chap. 5. Even though the film is located within one cell, and the flow profile hence is highly simplified, a correct behavior is obtained. Moreover, the velocity  $u$  of the bubble is seen to exceed the mean flow velocity in the fluid  $v$ . The pressure over the bubble does likewise exhibit correct behavior.

<sup>1</sup>Mean velocities of  $0.01 \text{ m s}^{-1}$  and  $1 \text{ m s}^{-1}$  correspond to flow rates of  $0.7 \mu \text{ L s}^{-1}$  and  $70 \mu \text{ L s}^{-1}$  in cylindrical tubes of radius  $r = d/2$ . The upper bound might be a little larger than normal flow rates used microfluidic devices.

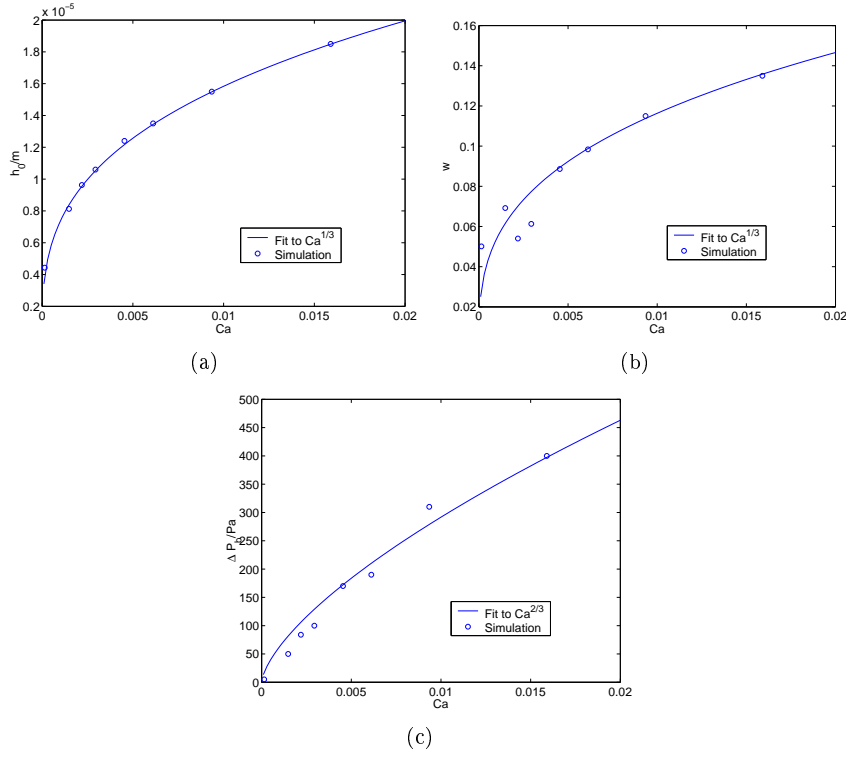


Figure 9.3: The simulated data for  $h_0$ ,  $w$ , and  $\Delta P_b$  plotted as function of  $Ca$  is presented as  $\circ$  marks while the fitted curves are full lines.

The collected data is found to depend on the capillary number  $Ca$ . The film thickness  $h_0^N$  is proportional to  $Ca^{1/3}$ ,

$$h_0^N \approx 0.49 \frac{d}{2} Ca^{1/3}, \quad (9.3)$$

and the velocity excess parameter  $w^N = (u - v)/u$  is also roughly proportional to  $Ca^{1/3}$ ,

$$w^N \approx 0.54 Ca^{1/3}. \quad (9.4)$$

From Eq. (9.2) it is obvious that  $h_0$  and  $w$  must depend on  $Ca$  in an identical manner. Finally, the pressure is found to be roughly proportional to  $Ca^{2/3}$ ,

$$\Delta P_b^N \approx 13 \frac{2\sigma}{d} Ca^{2/3}. \quad (9.5)$$

All the numerical factors are found by numerical fit. The simulated data and the fitted curves are presented in Fig. 9.3.

One simulation is further made using a finer mesh  $N = 24$  for  $v = 1$ . The values for  $h_0^N$  and  $w^N$  differ about 10% from the rough grid simulation ( $N = 12$ ), Table. 9.1. Because of the finer grid,  $h$  is here less than  $h_0$ , a slightly more detailed flow pattern is hence at hand in the wetting film. Though the VOF

$N$	$v/(\text{m s}^{-1})$	$u/(\text{m s}^{-1})$	$Ca$	$\Delta P_b^N/\text{Pa}$	$h_0^N/\mu\text{m}$	$w^N$
12	1.00	1.16	$1.59 \times 10^{-2}$	400	18.5	0.135
24	1.00	1.18	$1.63 \times 10^{-2}$	400	20.0	0.152

Table 9.1: Data for low ( $N = 12$ ) and high ( $N = 24$ ) resolution grid in moving bubble simulation.

model enables a partially higher resolution at walls the detail level of the velocity profile can only be increased by a "true" resolution of the wetting layer.

The values for  $\Delta P_b^N$  found in the two simulations concur. The pressure curvature routine in the VOF package exhibit robust properties. In the case of the rough grid the pressure drop is nearly proportional to  $Ca^{2/3}$  as 3D theory predicts. Whereas the dependence of both  $h_0$  and  $w$  differ from the 3D case. This discrepancy might be related to the two following properties: (1) The description of the wetting layer is highly simplified. (2) The continuity described by Eq. (9.2) that relates  $h_0$  to  $u$  is given in terms of lengths in 2D, whereas it is given in terms of area ratios in the 3D case,

$$\frac{u}{v} = \left( \frac{r - h_0}{r} \right)^2, \quad (9.6)$$

$r$  being the radius of a cylindrical capillary tube.

An interesting lesson to draw is that the specific details of the wetting layer eventually might be neglected. The specific behavior of a moving bubble with defined static contact angle is investigated in the next section.

### 9.1.2 Contact Angle and Flow Regimes

As emphasized earlier the boundary condition at the solid wall yield problems. The specification of a finite contact angle is not physically correct for bubbles moving above certain speeds, whereas it for clogged or static bubbles is meaningful. From a numerical point of view the grid size  $h$  is seen to play an important role. The specific transition speed, from wetting to contact angle description, is depending on specific surface properties. These facts actually impose restrictions on the problems that can be treated. Say a bubble is moving in a straight channel and suddenly encounters a contraction. It is here difficult to define the appropriate conditions for the simulation. In this subsection a few simulations dealing with the above described problems are discussed.

Firstly a bubble with finite contact angle  $\theta = 50^\circ$  is sent through a 2D channel at relatively high speed  $v = 0.6 \text{ m s}^{-1}$ . Channel width  $d = 300 \mu\text{m}$ , length  $L = 4200 \mu\text{m}$ , and a grid resolution of  $N = 12$ . Six snapshots of the rear end of the bubble are presented in Fig. 9.4.

The simulation exhibited several strange effects. First of all the pressure over the bubble is highly oscillatory  $300 \text{ Pa} \pm 150 \text{ Pa}$ . The liquid-gas interface did separate from the solid wall to some extent. Strange adhesion like effects then

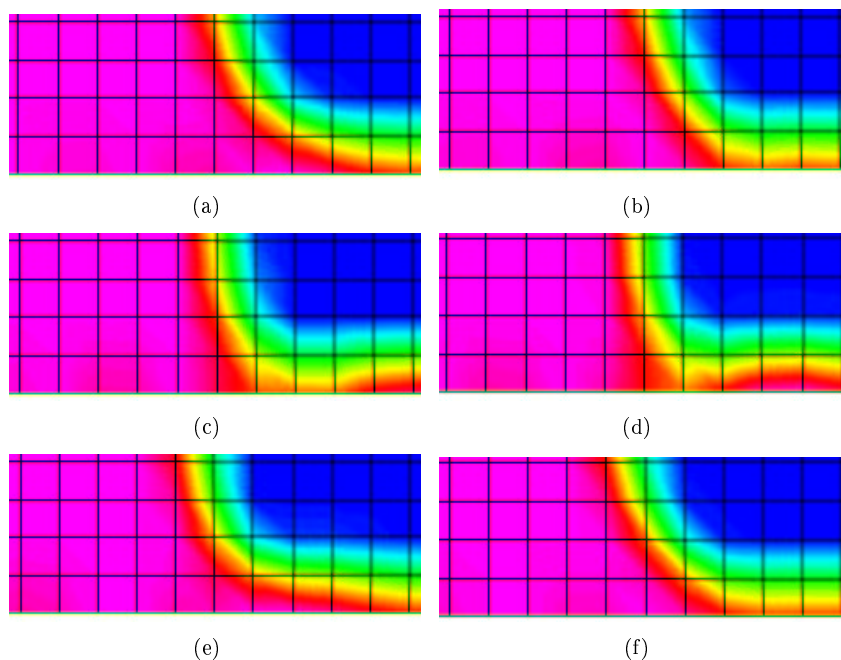


Figure 9.4: Time series of the rear of a wetting bubble. Small gas "droplets" are ejected from the rear where the bubble adheres to the solid wall periodically. The droplets are seen as lighter regions in the pink liquid area.

appear at the rear of the bubble; they are illustrated in Fig. 9.4. These effects are discussed thoroughly later. Small gas droplets are ejected from the bubble rear, they are in the figure seen as discolorations near the solid boundary. These artificial effects are most probably created as the solver influences the interface normal in wall cells. Runs were also made with  $\theta = 30^\circ$  and  $\theta = 70^\circ$  exhibiting the same conduct.

The same situation is simulated again, but in this case using a finer grid resolution  $N = 24$ . The liquid-gas interface once more separates from the solid wall and the adhesion-like effects are avoided. As the grid is finer the wall cell does not any more contain the interface ( $F_{\text{wall}} = 1$ ). This means that the interface is free to move in accordance with the governing flow equations. Compared to the simulation carried out with  $\theta = 0^\circ$  the bubble is seen to move slightly faster, about 2%. However the pressure drop over the bubble and the wetting film thickness are off with about 20%.

The placements of the relevant pressure and  $F$ -function plots on a bubble (after transient behavior) are depicted on Fig. 9.5. Note especially for the case in Fig. 9.5(b) how the  $F$  values are erroneous. Obviously  $F = 1$  in all of the wall cell and does not decrease as hinted in the figure. The CFD-VIEW data handling program does not provide adequate facilities to display the interface related data.

At last a simulation is run for  $v = 0.06 \text{ ms}^{-1}$  and  $\theta = 50^\circ$ . In this case no wetting film develops. The bubble does nonetheless exhibit a dynamical behavior: there is a pressure drop over the bubble resulting from different curvature

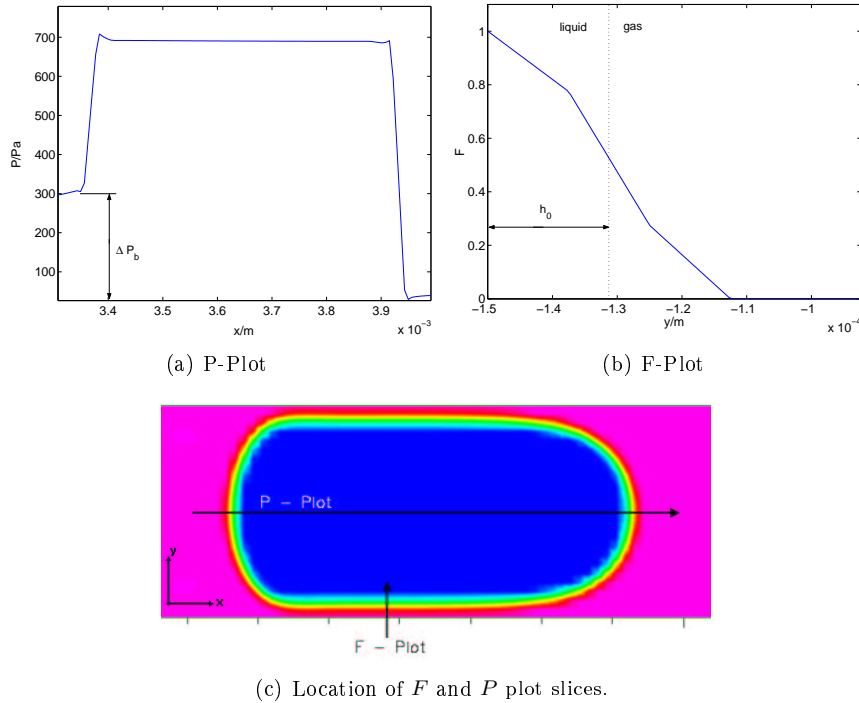


Figure 9.5: (a) Pressure as function of  $x$  plotted over the bubble length, and (b) the volume-of-fluid function  $F$  plotted over the wetting layer. (c) The actual slices where data is collected are marked on the figure.

of the rear and front interface.

The flow behavior in front of a moving bubble, having partial wetting condition  $0 < \theta < 180^\circ$ , is capable of creating a wetting film. The bubble front deforms because of the parabolic Couette flow profile. For sufficiently high capillary numbers the interface deformation in combination with a relative back flux of liquid near the wall enables a separation. It is paramount to remember that the wall condition for the interface does not directly change  $F$  values in wall cells. Only the interface normal  $\mathbf{n}_b$  is controlled, see Fig. 9.6(b). When an interface lies within a wall cells the described conditions can introduce the adhesion like effects.

The situation depicted on Fig. 9.6 is meant to illustrate the numerical adhesion effects taking place as a thin liquid layer form and move between the gas and the solid. The actual wetting layer thickness is represented by  $F$ -values as in Fig. 9.6(a). However, the solver engine CFD-ACE(U) internally places the interface as shown in Fig. 9.6(b). This numerical handling of wall cells results in the previously mentioned adhesion like effects.

Despite the numerical problems arising at the walls the CFD-ACE(U) solver showed promising dynamical properties. Regarding the wetting layer the ratio  $h_0/h$  is of special importance as it influences on possible numerical adhesion effects. After a thorough investigation of the basic dynamic capabilities of the VOF module the clogging phenomenon discussed in Sec. 5.2 is presented in the

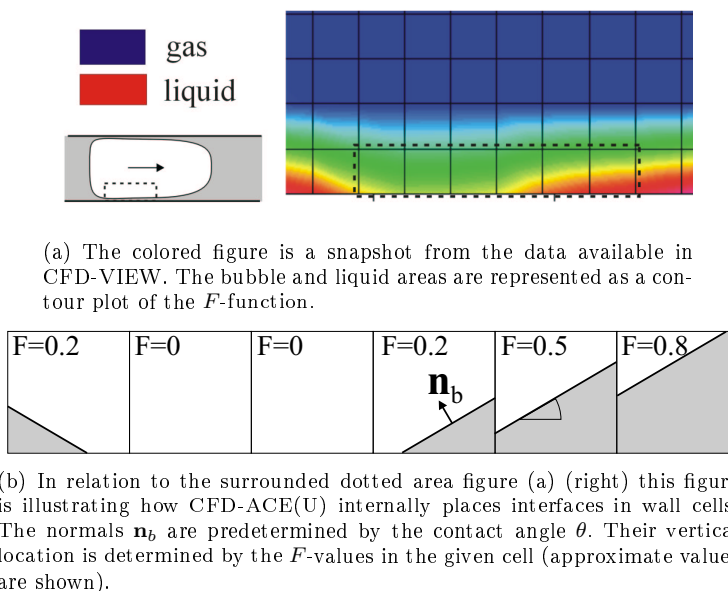


Figure 9.6: The numerical adhesion effects observed in simulations are in this figure sketched out. The difference between (a) the available  $F$ -data, and (b) the actual internal use of  $F$ -values is emphasized.

following.

## 9.2 Sudden Contraction

The theoretical results regarding the sudden contraction geometry discussed in Sec. 5.2 are here compared with simulations. Even though all free surface simulations are time dependent the basic outcome after a transient period is here static. As mentioned earlier CFD-ACE(U) has a robust internal pressure/curvature routine. The outcome of the simulations are at forehand expected to be good even for rough computational grids.

A sudden contraction having dimensions  $D = 260 \mu\text{m}$  and  $d = 100 \mu\text{m}$  is depicted on Fig. 9.7. The narrow channel has a rather rough vertical resolution of  $N = 9$ , all grid cells are square and identical.

The counter pressure predicted by Eq. (5.13) for  $\theta = 73^\circ$  and  $\sigma = 0.0725 \text{ J m}^{-2}$  is applied to the inlet (left side of the channel). In the 2D case  $P = 260.9 \text{ Pa}$  as the simulations do not account for friction. The gas plug is as expected seen to be stable and static. A simulation with both inlet and outlet pressures equal to zero showed that the gas bubble moved towards the left. This corroborates the prediction given by the "driving pressure gradient" concept described in Sec. 4.6.

## 9.3 Tapered Channel

The tapered channel geometry is the final simple, but important 2D geometry to be analyzed. Results obtained from simulations are compared with theory. The

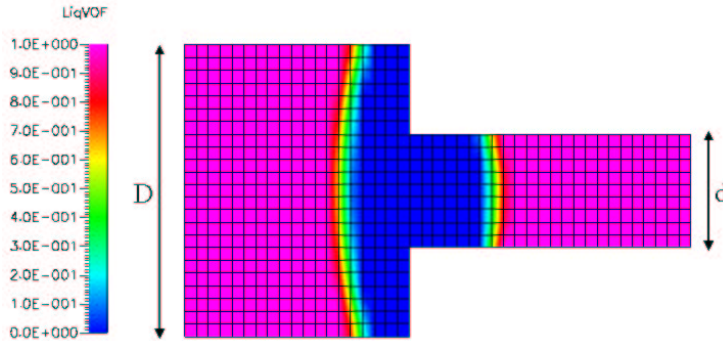


Figure 9.7: A static gas plug in a sudden contraction geometry  $D = 260 \mu m$ , and  $d = 100 \mu m$ . The liquid-solid contact angle is set to  $73^\circ$  and  $\sigma = 0.0725 \text{ J m}^{-2}$  representing water in a PMMA structure. The plug is static when the correct counter pressure is applied at the left.

results, treating of static bubbles, produced by the MATLAB clogging program are hence of prime interest as they build upon the theory presented in Sec. 5.2. The program made by the author and is presented in Appendix D.

**Set-up and Geometry**

Compared to the sudden contraction the tapered channel geometry contracts from an initial width  $D_i$  to the a narrower width  $d_i$  over the length  $L_i$ . The contraction has a so-called tapering angle defined as

$$\theta_t = \arccos\left(\frac{D_i - d_i}{2L_i}\right), \tag{9.7}$$

the dimensions and  $\theta_t$  are presented in Fig. 9.8.

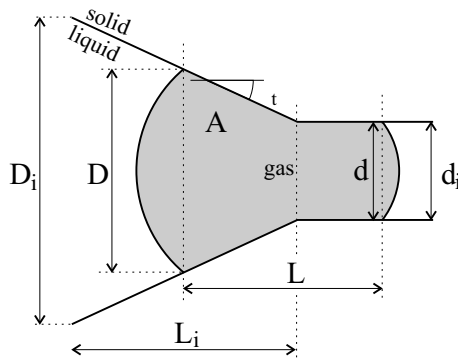


Figure 9.8: The geometry of the tapering channel problem is defined through the lengths  $D_i$ ,  $d_i$ , and  $L_i$ . Dynamically varying lengths defining the bubble are  $D$ ,  $d$ , and  $L$ . As the bubble is planar it has an area named  $A$ .

A bubble entering the contraction is furthermore defined through the lengths  $D$ ,  $d$ , and  $L$ . Where  $D$  is the left meniscus height,  $d$  the right meniscus height (on the figure  $d = d_i$ ), and  $L$  is a measure of bubble length. They are obviously varying as the bubble moves into the tapering. The total gas/bubble area  $A$  is constant as the gas is modelled as incompressible. The conservation of area  $A$  obviously plays a key role in the MATLAB clogging program.

Assume that no external pressures are applied and that no friction is present. A wetting bubble placed in the purely tapered region may under these assumptions move either in or out of the tapering. The direction is defined by the sign of the driving pressure gradient  $\Gamma = -\Delta P_b / (L_i - L)$  (recall Eq. (4.31)) where  $\Delta P_b$  is defined in Eq. (5.14). If  $\Gamma > 0$  the movement is towards the left while for  $\Gamma < 0$  it is towards the right. The specific sign depends on the geometry and nature of the bubble, i.e.,  $A = A(D, d, L)$ .

• **Example**

As a function of the bubble length the transition from  $\Gamma < 0$  to  $\Gamma > 0$  happens at the critical length

$$L_c = D \frac{\cos \theta_t \sin \theta}{\cos(\theta - \theta_t)}. \quad (9.8)$$

The length can in turn be translated into an area (volume in 3D). The tapering angle  $\theta_t$  hence determines the efficiency of a contraction to move a bubble of a given area/volume. The geometry might hence ease the movement of bubbles into a contraction.

In the simulations the bubble is initiated as a plug at the left of the channel. No external pressures are applied. The bubble length  $L$  is chosen,  $L < L_c$ , such that the bubble moves into the tapering under its own driving ( $\propto \Gamma$ ). As the bubble is moving the curvature of the front and rear interfaces are thus expected to differ from the static solution modelled in the MATLAB program.

**Results**

Three representative cases are in the following studied using one tapering geometry. The physical parameters used represent an air (a) bubble in water (w) enclosed in a PMMA structure.

**Data:**  $D_i = 300 \mu\text{m}$ ,  $d_i = 100 \mu\text{m}$ ,  $L_i = 500 \mu\text{m}$ ,  $\theta_t = \arctan(1/5) \approx 11.5^\circ$ ,  
 $\rho_w = 1000 \text{ kg m}^{-3}$ ,  $\rho_a = 1.16 \text{ kg m}^{-3}$ ,  $\sigma = 0.0725 \text{ J m}^{-2}$ ,  $\mu_w = 10^{-3} \text{ Pa s}^{-1}$ ,  
 $\mu_a = 1.85 \times 10^{-3} \text{ Pa s}^{-1}$ , and  $\theta = 73^\circ$ .

**1:** The bubble is initiated  $100 \mu\text{m}$  from the left boundary with  $L = 100 \mu\text{m}$ . The bubble moves into the tapering while the relevant data is collected. A time series of four snapshots from CFD-VIEW is presented in Fig. 9.9. The initial gas plug achieves correct curvature after about 50 time steps that is  $\approx 5 \times 10^{-4} \text{ s}$ .

The pressure over the bubble  $\Delta P_b^N$  as well as the geometric parameters obtained from the simulation are presented in Fig. 9.10 together with the static results from the MATLAB program. All data is plotted as a function of  $D$ . Decreasing  $D$  values hence represent the bubble moving into the tapering and vice versa.

The geometric parameter are seen to comply well with theory. CFD-ACE(U) obviously respect the conservation of area as well as the geometric constrains. However, discrepancies are present in the pressure data because the bubble is moving instead of being static. The dynamic nature of the system deforms the curved interfaces.<sup>2</sup> The relative change in  $D$  and  $d$ , as the bubble elongates,

<sup>2</sup>For simulated data to be compared with theory the system should be quasi stationary. Several options are available: (1) Introduce a high amount of un-physical viscosity in the liquid. (2) Add friction at the walls if it were possible. (3) Apply a counter pressure. It is however only possible to measure one static data point with the third option.

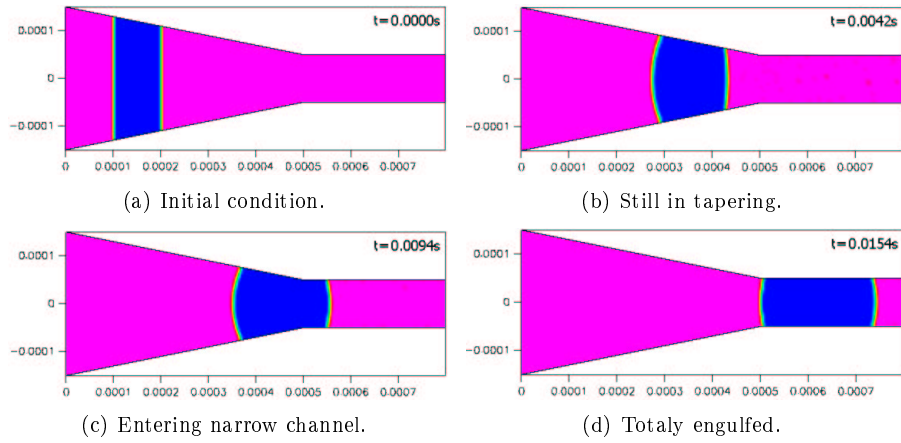


Figure 9.9: Four snapshots of a contour plot of the  $F$ -function taken at four characteristic positions of the bubble in the tapered channel. Blue areas represent gas ( $F = 0$ ) and pink areas liquid  $F = 1$ . The actual times since simulation start are shown on the figures.

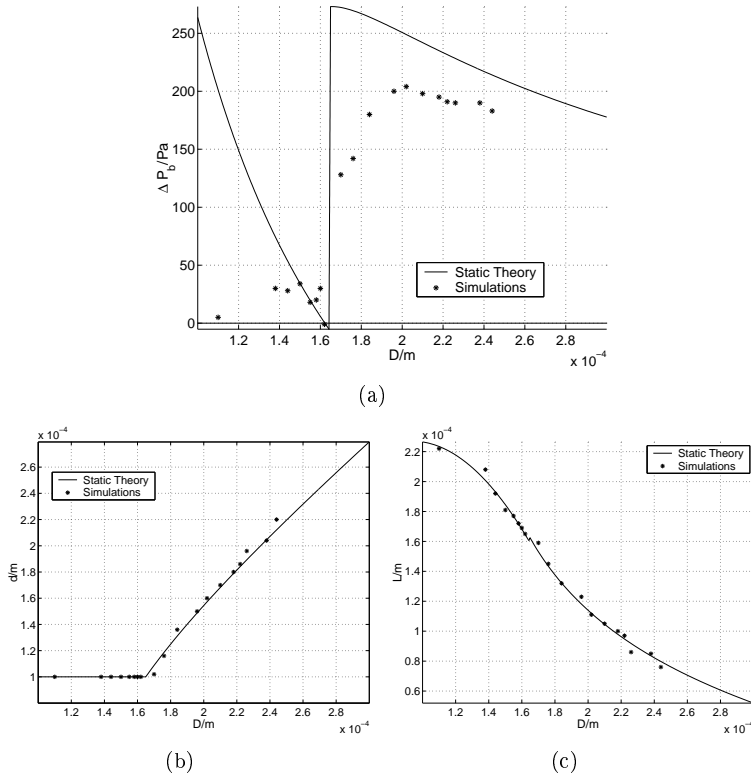


Figure 9.10: Simulations and static theory data for: (a) The pressure  $\Delta P_b$ , (b) the right meniscus diameter  $d$ , and (c) the bubble length  $L$ . All plotted as a function of the left meniscus diameter  $D$ .

further generates varying dynamics at the front and rear. This last characteristic is illustrated in Fig. 9.11. According to the theoretical curves the bubble should be stationary at the points where  $\Delta P_b = 0$ , however, this does not happen. The negative portion of  $\Delta P_b(D)$  is very small and is maybe overcome by numerical oscillations in  $\Delta P_b^N$ .

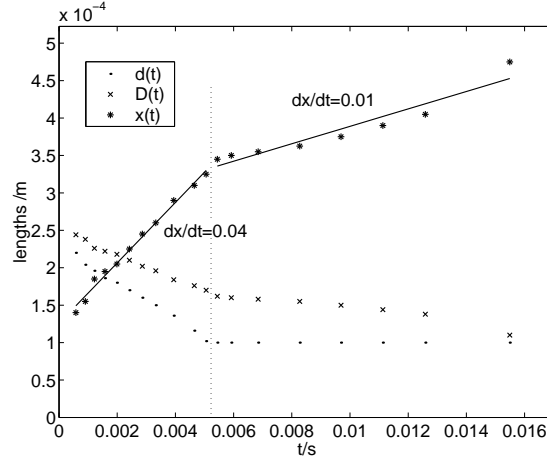


Figure 9.11: Distance from inlet to the bubble  $x$  and the bubble widths  $D$  and  $d$  plotted as function of time. The vertical dotted line marks the entering of the right interface into the narrow channel. The speed  $dx/dt$  (in m/s) of the bubble is found by use of linear fits.

In relation to Fig. 9.11 the speed of the bubble is determined via the introduction of a new variable  $x$ . It measures the distance between the bubble and the inlet (left side). Observe that the position  $x(t)$  of the self propelled bubble is nearly piecewise linear in time  $t$ . The speed  $dx/dt$  of the bubble varies from  $0.04 \text{ ms}^{-1}$  to  $0.01 \text{ ms}^{-1}$  as the right interface enters the narrow channel. The speed will drop to zero when the bubble is completely located in the narrow channel.

The exact nature of the variations in  $dx/dt$  are not clear. The dependency with respect to tapering angle  $\theta_t$ , contact angle  $\theta$  and initial bubble area  $A$  are interesting topics. Changes in one of these parameters determine the character of the interplay between  $D$  and  $d$  and hence on the driving pressure gradient. Such a thorough investigation is very tedious especially in regard to the data collection in CFD-VIEW. Further an external driving pressure difference between inlet and outlet might be added.

**2:** By increasing the initial bubble area (increasing  $L$  to  $200 \mu\text{m}$ ) the part of the static pressure curve beneath zero increases, compare Fig. 9.10(a) with Fig. 9.12. This is made to render probable that the bubble will get stuck:  $\Delta P_b \leq 0$  yields  $\Gamma \geq 0$ .

Fig. 9.12 depicts how  $\Delta P_b^N$  actually goes to zero. The bubble gets stuck as the right interface enters the narrow channel. As mentioned in the previous discussion the actual bubble area plays an important role regarding the clogging properties of a tapered channel.

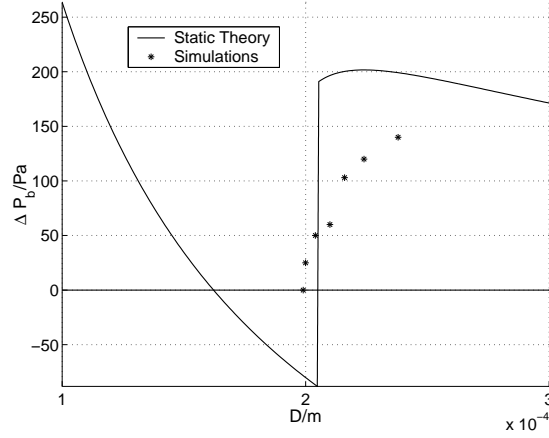


Figure 9.12:  $\Delta P_b$  theoretical and simulated data. The pressure over the bubble  $\Delta P_b^N$  goes to zero where static theory predict the bubble to be stuck.

**3:** Finally points on the theoretical curve are verified by applying an appropriate counter pressure and letting the bubble move to rest  $\Gamma = 0$ . The theoretical values predicted by the MATLAB program were confirmed, once more emphasizing the reliable and robust internal pressure/curvature routine of CFD-ACE(U).

### Conclusion

The tapered channel geometry exhibits interesting features both from an academic point of view, but certainly also from an application point of view. Depending on the bubble size and channel geometry a tapered contraction may actually ease the passage of bubbles from one channel diameter to another. The curvature contribution to the clogging pressure Eq. (5.18) may be negative.

#### • Example

A 2D air bubble is used as an example. The bubble of area  $\approx 200 \times 300 \mu\text{m}^2$  is placed in a water filled PMMA channel ( $\theta = 73^\circ$ ), contracting from  $D = 300 \mu\text{m}$  to  $d = 100 \mu\text{m}$ . The clogging pressure associated with the sudden contraction is

$$P^s = P_{\text{friction}} + 283 \text{ Pa} \quad (9.9)$$

whereas it for the tapered channel ( $\theta_t = 11^\circ$ ) is

$$P^t = P_{\text{friction}} + 90 \text{ Pa}. \quad (9.10)$$

The pressure due to friction  $P_{\text{friction}}$  is not geometry dependent. The difference is quite significant and not to be neglected in actual microchannel designs.

In light of the theoretical results derived in Sec. 5.2 and the simulations of the contracting channel, it becomes obvious that the tapered geometry is preferred to the sudden contraction. When designing actual micro systems sudden contractions and sharp edges should be avoided. This in turn represents a simple but yet evident design rule.

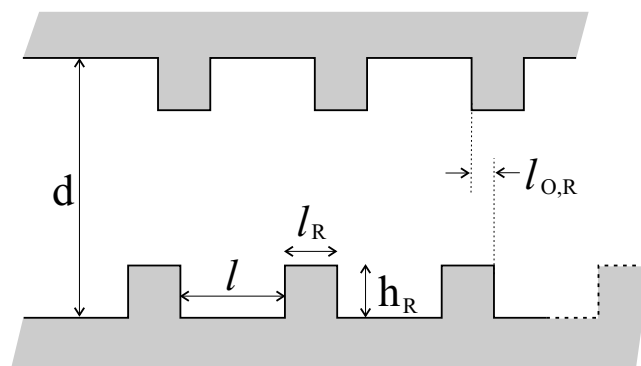


Figure 9.13: Geometry of a channel with roughness knobs at the walls. The knobs are rectangular with dimensions  $l_R$  and  $h_R$  and are placed at a distance  $l$ . Asymmetry of the system is defined through the off-set length  $l_{O,R}$

## 9.4 Roughness

It is in the CFD-ACE+ package not possible to include the friction effects experienced by the contact lines of moving bubbles. The effects are, in the theoretical study of Chap. 5, accounted for through the empiric frictional surface tension parameter  $\alpha$ . The parameter includes both friction effects due to chemical processes on the solid boundary as well as the friction due to knobs and other physical distortions of the solid surface.

### Set-up and Geometry

An investigation of direct simulation of simple idealized rough surfaces is here presented. Identical square knobs are added to the walls of a straight channel of width  $d$  as depicted on Fig. 9.13. The knobs are  $h_R$  high,  $l_R$  wide, and are placed at distance  $l$ . Asymmetry is introduced through the off-set length  $l_{O,R}$  also defined on the figure.

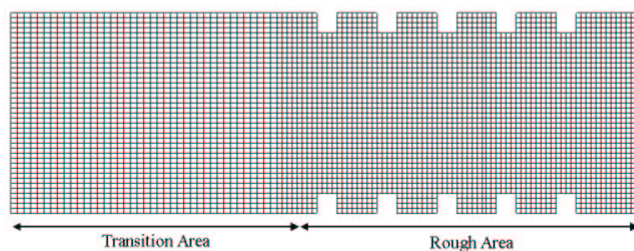


Figure 9.14: Actual computational domain and grid with transition and rough areas shown. The present case has a symmetrical roughness distribution, i.e.,  $l_{O,R} = 0$ .

The actual geometry is easily implemented and gridded in CFD-GEOM. To keep calculation time at a minimum the knobs are only resolved with a  $4 \times 4$  grid. Even though the grid is relatively coarse the number of cells is however a factor 4 to 5 larger compared to the simple straight channel previously discussed. There are approximately  $40 \times 100$  cells. Special care is further taken because of the transient nature of the simulation. A non-rough transition area where the

bubble is initiated is placed before the "Rough Area". The bubble thus has time to take up a natural shape. On Fig. 9.14 the computational domain and grid are depicted for  $l_{O,R} = 0$ . The transition area is quite large so that relatively large bubbles may be initiated.

### Theory

When the contact angle description is used in the simulations it is easy to make simple analytical considerations about the involved pressures. They are only based on the Young-Laplace equation, the contact angle  $\theta$  and the geometric constrains of the system.

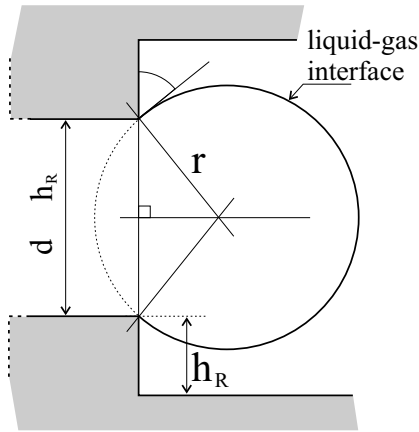


Figure 9.15: Distorted sketch of a liquid gas interface at the verge of crossing a knob of height  $h_R$ . The radius of curvature of the interface is  $r = d/(2 \cos(\pi/2 - \theta))$ .

An important information regarding the geometry depicted in Fig. 9.13 is the maximal possible pressure drop needed to sustain a bubble. The situation arises for  $l_{O,R} = 0$  if one end of the bubble is located at a wide part of the channel and the other is just about to cross a knob as shown in Fig. 9.15. The interface will deform continuously around the knob corner until it attains the predefined contact angle  $\theta$ . The maximal pressure to sustain a bubble is readily found as<sup>3</sup>

$$\Delta P_{b,\max} = 2\sigma \left( \frac{\cos \theta}{d} - \frac{\cos(\frac{\pi}{2} - \theta)}{d - 2h_R} \right). \quad (9.11)$$

Suppose a bubble is present in the idealized system depicted in Fig. 9.13 and it has a finite contact angle  $\theta$ . The pressure defined by Eq. (9.11) then corresponds to the maximal "friction" pressure. The value of the frictional surface tension parameter  $\alpha$  is hence known in advance, as defined by Eq. (5.15), and is given by

$$\alpha = \frac{d\Delta P_{b,\max}}{4}. \quad (9.12)$$

### Simulation Results

The roughness and channel have dimensions  $d = 300 \mu\text{m}$ ,  $l = 60 \mu\text{m}$ , and  $l_R = h_R = 30 \mu\text{m}$ . In the symmetric case  $l_{O,R} = 0$  the predicted maximal "intrusion"

<sup>3</sup>This pressure also represents the pressure needed to push a bubble out of a sudden contraction. That is from the shallow to the wide channel.

pressure defined by Eq. (9.11) is confirmed by varying  $\theta$  and the externally driving pressure gradient.



Figure 9.16: A wetting bubble nearly totally within the rough area. Dimensions:  $d = 300 \mu\text{m}$ ,  $l = 60 \mu\text{m}$ ,  $l_R = h_R = 30 \mu\text{m}$ ,  $l_{O,R} = 0 \mu\text{m}$ .

Only a few simulations were carried out. The variation of geometrical parameters is very tedious and basically does only confirm theoretical results. The ratios  $l/l_R$  and  $d/h_R$  as well as offset are important. They determine the minimal pressure needed to initiate flow in a rough capillary. Furthermore the ratio  $l/l_R$  determines if a bubble will jump over a crevasse and leave a pool of liquid as depicted on Fig. 9.16 or wet the channel wall completely.

The presence of roughness increases the travel time of a bubble and hence decrease its mean velocity. The deformation of the bubble due to the roughness requires energy. The externally imposed driving pressure gradient is diminished considerably as it has to sustain the bubble. A further investigation might include more realistic non-regular roughness. It should in CFD-ACE+ be possible to include the empirical roughness parameter  $\alpha$ . The direct simulation of roughness is not a realistic option especially regarding the grid generation and increased simulation time.

## 9.5 Passive Bubble Trap

Suppose a certain microfluidic device has an unavoidable tendency to create bubbles at a certain location. If the device moreover cannot include active bulky removal systems a solution may lie in passive so-called bubble traps. The novel idea of a bubble trap was discussed with supervisor G. Goranović during the thesis work. The basic design is based on two principles: (1) Trapping the bubble using the curvature effects described by the Young-Laplace equation. (2) Optimizing the geometry to allow for unhindered flow after trapping.

After different initial designs and tests a final version with two key features is developed by the author. The idea is that the trap diverts the bubble in the so-called offset region towards the trap region. The sketch of the final bubble trap is presented in Fig. 9.17.

The central task of the offset region is to make a wetting bubble detach from the upper channel wall before reaching the trapping region. When the bubble has detached the flow will drive the bubble towards the two contractions ( $l_t < d$ ) where it will get trapped. Depending on the size of the bubbles present in a system the offset length  $l_o$  should be varied. For the trap to work the bubble length should be about two or three times  $l_o$ . Note that the offset feature of the present

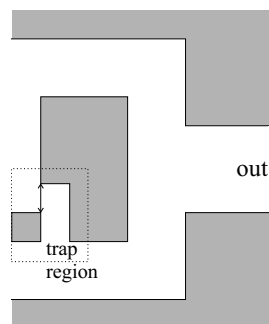


Figure 9.17: Geometry of the bubble trap. The offset region and specific length  $l_o$  as well as the trap region and length  $l_t$  are shown.

trap builds upon the assumption of a wetting bubbles. As the bubble enters the trap region the curvature effects created by the two narrow parts ( $l_t < d$ ) clogs the bubble according to the principles discussed in Chap. 5.

The bubble trap functions are in the following investigated computationally. The geometry depicted in Fig. 9.17 is used with  $d = 150 \mu\text{m}$ ,  $l_o = 50 \mu\text{m}$ , and  $l_t = 50 \mu\text{m}$ . The initial condition and full geometry within bounds is presented in Fig. 9.18 followed by four snapshots at selected times in Fig. 9.19 (a) to (d).

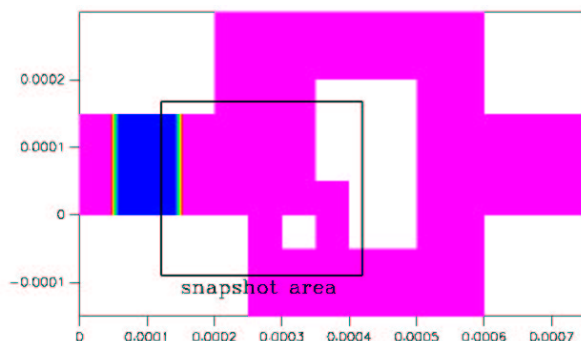


Figure 9.18: Initial condition and bounds of the bubble trap. The area illustrated by the following four snapshots is marked with a black box, Fig. 9.19.

The simulated bubble trap is only adequate for small bubbles. If larger bubbles are used they clog the system. In an actual microfluidic device several bubble traps with varying offset length should be placed in series to obtain maximal trapping efficiency. The simulation illustrates how the basic design features are efficient and work according to intend. However, the design is not perfect and is only here tested in 2D. The flow is still distorted by the bubble and especially is forced through sharp turns which is generally to be avoided in microfluidic devices. The basic concepts presented are interesting and should be included in future 3D models and further developments.

At last it should be noted that the trap is ineffective if non-wetting bubble conditions are used. The bubble ends up sitting as shown in Fig. 9.20. Liquid is passing on both sides of the bubble and holds it in a stable locked position. This

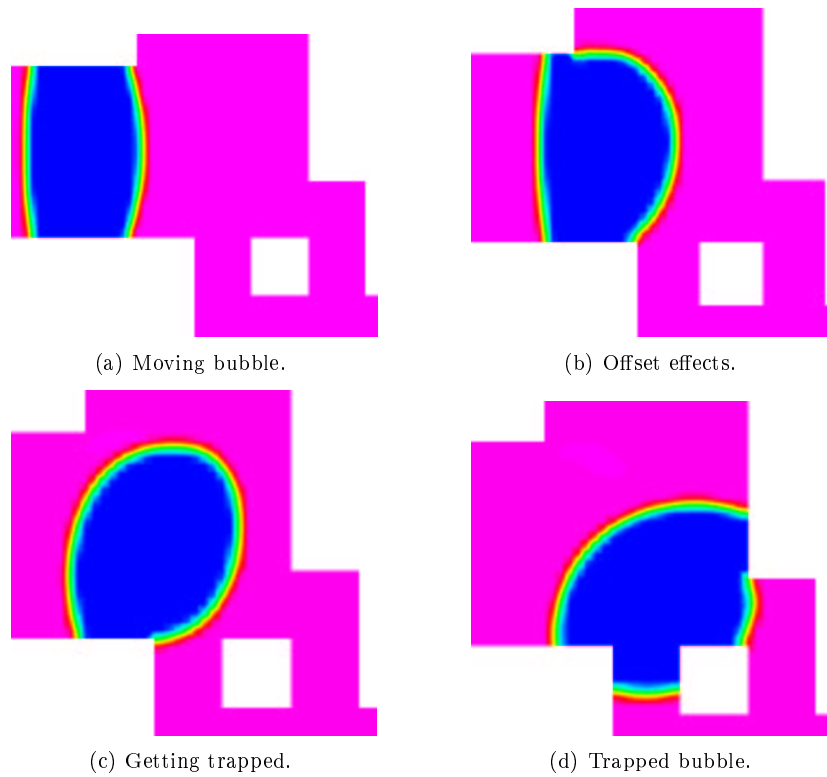


Figure 9.19: Four selected snapshots of a bubble getting trapped. Notice that the flow is free to pass the trapped bubble.

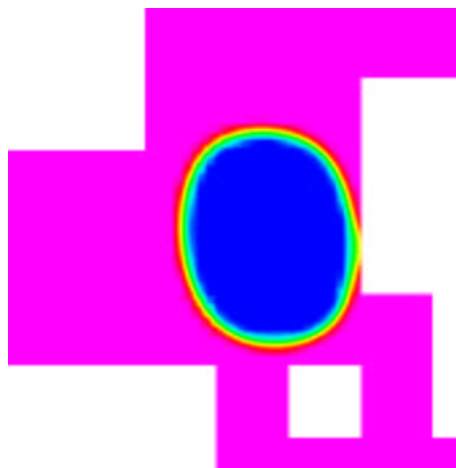


Figure 9.20: A non-wetting bubble,  $\theta = 0^\circ$ , stuck in a stable position and not entering the trap region as desired.

all leads back to the question about proper definition of boundary conditions.

**Outlook and Ideas**

In addition to the passive bubble trap presented above several other ideas con-

cerning the removal of bubbles where also discussed. Some of the ideas and areas needed to be investigated are shortly summarized:

- Use of different hydrophobic/hydrophilic regions in the channel structures was discussed with N. J. Petersen [52]. This principle is readily used in so called hydrophobic valves Man *et al.* [51].
- Use of special porous materials to extract gas bubbles from the liquid (e.g., goretex). Say, a bubble is localized in the "bug leg"-like structure depicted in Fig. 9.21. By coating the channel walls with a porous material it might be possible to extract/suck the bubble out of the flow. The ideas was discussed with supervisor G. Goranović.

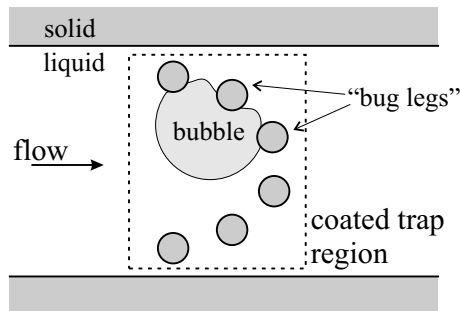


Figure 9.21: Trapping an localizing a bubble in a so called "bug leg" structure. Walls might be coated with, e.g., goretex having the property of removing the gas from the liquid.

- Study the specific surface energy induced properties of, e.g., porous materials.
- Investigate how to avoid that the flow in the bubble trap distorts eventual chemical plugs.



# Chapter 10

## 3D Simulations

The free surface capabilities of CFD-ACE+ are at last applied to two 3D cases. Calculation time is expected to increase drastically due to the increase in number of grid cells and because the surface reconstruction is slower in 3D.

### 10.1 Static Interface Shapes

The pressure drop over a static liquid-gas interface in a capillary tube of constant rectangular cross section is in Appendix E determined analytically. The pressure drop  $\Delta P_i$  is in Sec. 5.3 defined as

$$\Delta P_i = C_m \frac{\sigma}{R} \tag{10.1}$$

where  $C_m$  is the dimensionless curvature parameter,  $\sigma$  is the surface tension, and  $R$  is the radius of the largest inscribed circle of the cross section.

The full 3D static interface is in the following determined and the results are compared to theory. The time dependent simulations are initiated with an arbitrary flat interface. The resulting computation actually corresponds to solving the static problem with an iterative method. The time is then a measure comparable to a number of iterations. The interface will deform from an initial "guess" towards the static solution.

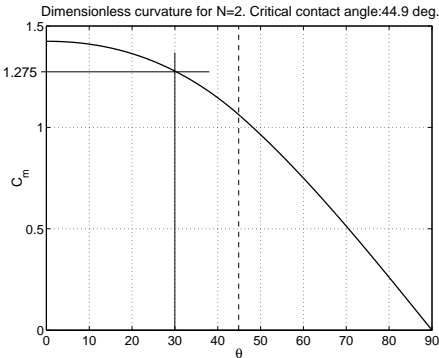


Figure 10.1: Dimensionless curvature as function of contact angle  $\theta$  for an aspect ratio of 2. The critical curvature is marked with a vertical dotted line. The figure is produced by the MATLAB program presented in Appendix E.

A rectangular capillary tube of height  $a = 100 \mu\text{m}$  and width  $b = 200 \mu\text{m}$  is investigated (hence an aspect ratio of 2). From the results obtained in Appendix E the critical contact angle is known to be  $\theta_c = 44.9^\circ$ . The dimensionless curvature  $C_m$  is in Fig. 10.1 plotted as function of static contact angle  $\theta$ .

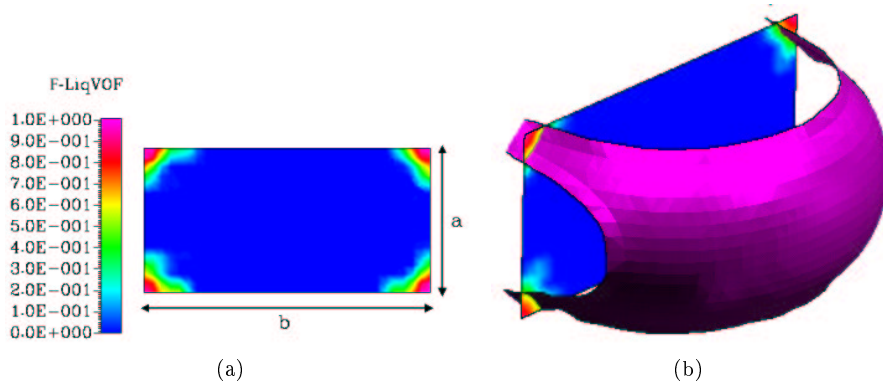


Figure 10.2: Static liquid-gas interface in a capillary tube of rectangular cross section. The contact angle is  $\theta = 30^\circ$ . Figure (a) depicts a contour plot of  $F$  in a cross section away from the curved interface. (b) contour surface of  $F$  illustrating the actual interface shape.

The meniscus of a liquid having a contact angle  $\theta = 30^\circ < \theta_c$  and surface tension  $\sigma = 0.0725$  is presented in Fig. 10.2. The corner wetting liquid areas described in Sec. 5.3 are depicted in Fig. 10.2(a) where a contour plot of  $F$  is presented in a cross section plane lying away from the interface front. In Fig. 10.2(b) the interface is presented as a contour surface of  $F$  for  $F = 0.5$ .

The theoretical pressure drop is  $\Delta P_i = 1860 \text{ Pa}$  with  $C_m = 1.28$  and  $R = 50 \mu\text{m}$ . The simulations yields  $\Delta P_i^N \approx 1930 \text{ Pa}$  corresponding to a relative error of only 3.5%.

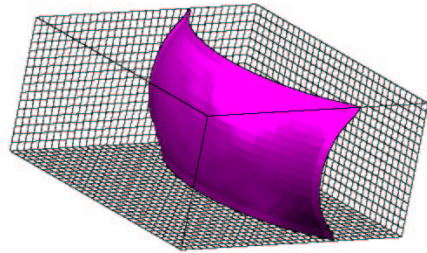


Figure 10.3: Static liquid-gas interface and computational grid for  $\theta = 50^\circ > \theta_c$ .

When a contact angle  $\theta$  is chosen greater than the critical value  $\theta_c$  the simulation correctly predicts that no wetting liquids form in the corner regions of the tube. Fig. 10.3 depicts the interface shape for  $\theta = 50^\circ$ . The computational grid of  $14 \times 28 \times 28$  cells is shown. The theoretically predicted pressure drop is  $\Delta P_i = 1398 \text{ Pa}$  and simulation yielded  $\Delta P_i^N \approx 1420 \text{ Pa}$  corresponding to a relative error of only 1.5%.

The theory and simulations are seen to agree. For the case of static interfaces analytical methods are seen to be powerful tools. The simulations also confirm

that the internal pressure/curvature routines of CFD-ACE(U) are efficient, also in the 3D case.

## 10.2 Circular Tube

The case of a non-wetting bubble moving in a cylindrical tube of radius  $a = 75 \mu\text{m}$  is investigated as a final 3D example. The pressure drop over the bubble  $\Delta P_b^N$  as well as the thickness of the wetting film layer  $h_0^N$  are compared to the theoretical results from Sec. 5.4 (Eqs. (5.22), (5.23), (5.24), and (5.25)).

The simulation is only carried out for one set of parameters as the computational time is extremely high. The run took about 5 days whereas simulation of the static interface only took about 4h. Even after 5 days the bubble had only moved about one third of the over all tube length  $L = 1500 \mu\text{m}$ . The grid is constructed with very cubical cells and contains 46800 cells.

$Ca \times 10^{-4}$	$u \times 10^{-2}$	Theory				Simulations		
		$v \times 10^{-2}$	$w \times 10^{-3}$	$\Delta P_b$	$h_0$	$w^N$	$\Delta P_b^N$	$h_0^N$
1.25	0.9	1.2	3.23	22.7	25.1	-	31	< 15

Table 10.1: Results from the numerical simulation. All velocities are measured in m/s, the wetting film thickness in m, and the pressures are in Pa.

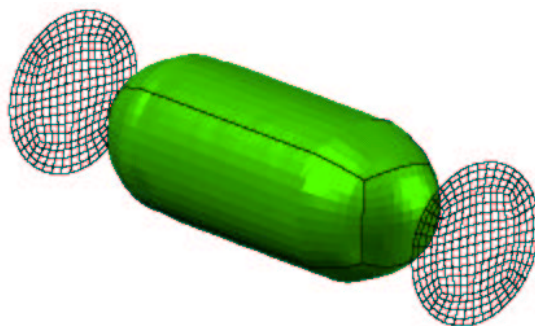


Figure 10.4: A contour surface of the  $F$  function for  $F = 0.5$  illustrating the 3D bubble in a cylindrical tube. Two cross section cuts are placed in front and behind the bubble illustrating the grid.

The theoretical and simulated data are presented in Table 10.1. The bubble and grid are illustrated in Fig. 10.4. The data from the simulation does not comply with theory. The bubble moves slower than the mean flow velocity moreover the predicted wetting layer is much larger than the maximal simulated. The discrepancies may be due to numerical errors or simply the fact that the static solution has not yet been reached: the bubble is still transient.



# Chapter 11

## Conclusion

To investigate the behavior of bubbles in microchannels a combined approach of both a theoretical study and numerical simulations is adopted. The procedure results in a thesis with a complete and thorough investigation of several phenomena.

The first part of the thesis thoroughly presents and discusses the important surface tension and contact angle related phenomena, in case of both static and moving bubbles. The static contact angle description is applied and used to characterize the behavior of static bubbles in two specific contracting geometries: the sudden contract and tapered channels. A MATLAB program is developed specifically to analyze clogging effects of bubbles in tapered channel geometries.

The theoretical study did, moreover, pinpoint some open questions that need to be addressed in the future. Especially the precise behavior of moving contact lines need to be clarified.

The second part of the thesis is dedicated to a numerical investigation of several bubble phenomena. For this purpose the commercial CFD-ACE+ software package is utilized. A great amount of knowledge about the program is gained, principally about the volume-of-fluid (VOF) free surface handling method.

The CFD-ACE(U) solver has good assets when handling, both 2D and 3D, static interfaces. After a transient phase numerical results agree with theory. The internal pressure/curvature calculation routines are robust. It is thus a pity that the internally reconstructed piecewise linear surfaces may not be exported to CFD-VIEW and visualized.

The dynamical behavior of moving 2D bubbles in a simple straight channel is analyzed in the view of previously discussed 3D theory. The pressure drop over the bubbles  $\Delta P_b$  as well as the wetting layer thickness  $h_0$  exhibit correct behavior. The indirect high wall resolution embedded in the VOF model is seen to work even though the flow profile is very simplified. The behavior of bubbles in the tapered channel geometry is compared to the theoretical predictions of the MATLAB program. As the bubbles move the interfaces deform the results thus differ. The driving pressure gradient concept developed is seen to be very useful. The static clogging program pinpoints critical positions where bubbles

get stuck. The simulations deliver the pressure effects due to curvature described by the Young-Laplace equation. Geometries may hence be optimized in that regard. Friction at the contact line is a material specific parameter. Comparing the tapered channel geometry to the sudden contraction geometry reveals that it decreases the pressure needed to move a bubble through a specific contraction. Depending on the bubble size and geometry the clogging pressure due to curvature may be from halved to totally removed.

During the numerical investigation the limitations of the VOF module are pinpointed. The specification of proper boundary conditions at solid walls is very limited and yield problems: (1) Erroneous numerical wall adhesion effects appear, (2) it is not possible to include friction effects, and (3) transition from contact angle to wetting regimes is not accounted for. The sharp identification of numerical errors illustrates how physical understanding is significant for good CFD practice.

As a result of combined CFD and theory a novel passive bubble trap geometry is developed and simulated. The geometrical properties are optimized so that bubbles get trapped while letting the flow continue unhindered.

---

MADS JAKOB JENSEN, c960853





# Bibliography

- [1] A. W. Adamson and A. P. Gast, *Physical Chemistry of Surfaces*, John Wiley & Sons, Sixth Edition, 1997.
- [2] R. F. Probstein, *Physicochemical Hydrodynamics: An Introduction*, John Wiley & Sons, Second edition, 1994.
- [3] A. W. Adamson, *Physical Chemistry of Surfaces*, John Wiley & Sons, Third Edition, 1976.
- [4] J. Fredsøe, *Hydrodynamik*, Den private ingeniør forening, DTU, 3. udgave, maj 1994.
- [5] R. S. Millman & G. D. Parker, *Elements of Differential Geometry*, Prentice Hall, 1977.
- [6] P. W. Atkins, *Physical Chemistry*, Oxford University Press, Fifth Edition, 1994.
- [7] T. Guénault, *Statistical Physics*, Chapman & Hall, Second Edition, 1994.
- [8] E. Both and G. Christiansen, *Termodynamik*, Den private Ingeniørfond, 3. oplag, 1995.
- [9] D. Y. Kwok and A. W. Neumann, *Contact Angle Interpretation: Combining Rule for Solid-Liquid Intermolecular Potential*, Journal of Physical Chemistry, B 2000, 104,741-746.
- [10] D. Y. Kwok and A. W. Neumann, *Contact Angle Interpretation in Terms of Solid Surface Tension*, Colloids and Surfaces. A: Physical and Engineering Aspects 161 (2000) 31-48.
- [11] S. Elliott, *The Physics and Chemistry of Solids*, John Wiley & Son, 1998.
- [12] B. Lautrup, *Continuum Physics; Exotic and Everyday Phenomena in the Macroscopic World*, The Niels Bohr Institute, Draft 5, 1999.
- [13] B. H. Bransden and C. J. Joachain, *Introduction to Quantum Mechanics*,
- [14] H. Smith and H. Højgaard Jensen, *Transport Phenomena*, Clarendon Press, Oxford, 1989.
- [15] P. G. de Gennes, X. Hua and P. Levinson, *Dynamics of Wetting: Local Contact Angle*, Journal of Fluid Mechanics 1990 vol. 212 pp. 55-63.

- [16] E. B. Dussan V., E. Ramé and S. Garoff, *On Identifying the Appropriate Boundary Conditions at a Moving Contact Line: An Experimental Investigation*, Journal of Fluid Mechanics 1991 vol. 230 pp. 97-116.
- [17] E. B. Dussan V., *The Moving Contact Line: The Slip Boundary Condition*, Journal of Fluid Mechanics 1976 vol. 77 p. 665.
- [18] E. Ramé and S. Garoff., *Microscopic and Macroscopic Dynamic Shapes and the Interpretation of Dynamic Contact Angles*, Journal of Colloid and Interface Science 1996 vol. 177 pp. 234-244.
- [19] R. Osserman, *A Survey of Minimal Surfaces*, Dover Publications, inc. third edition, 1986.
- [20] Len M. Pismen and Boris Y. Rubinstein, *Kinetic Slip Condition, van der Waals forces, and Dynamic Contact Angle*, Americal Chemical Society, 2001.
- [21] M. A. Tenan, S. Hackwood and G. Beni, *Friction in Capillary Systems*, Bell Laboratories, Journal of Applied Physics, 53, 1982.
- [22] H. Matsumoto and J. E. Colgate, *Preliminary Investigation of Micropumping Based on Electrical Control of Interfacial Tension*, Department of Mechanical Engineering R. R. McCormick School of Engineering and Applied Science, Northwestern University, 1990.
- [23] A. M. Schwartz, C. A. Rader and E. Huey, *Contact Angle, Wettability and Adhesion*, Advances in Chemistry series No. 43, p.250, Americal Chemical Society, 1964.
- [24] T. C. Ransohoff, P. A. Gauglitz and C. J. Radke, *Snap-Off of Gas Bubbles in Smoothly Constricted Noncircular Capillaries*, AIChE Journal Vol. 33, No. 5, May 1987.
- [25] J. Ratulowski and H.-C. Chang, *Transport of Gas Bubbles in Capillaries*, Physics of Fluids A 1 (10), American Institute of Physics, October 1989.
- [26] J. Stark and M. Manga, *The Motion of Long Bubbles in a Network of Tubes*, Transport in Porous Media No. 40, p.201-218, Kluwer Academic Publisher, 2000.
- [27] H. J. Schulze, K. W. Stöckelhuber and A. Wenger, *The Influence of Acting Forces on the Rupture Mechanism of Wetting Films - Nucleation or Capillary Waves*, Colloids and Surfaces A No. 192, p.61-72, 2001.
- [28] F. P. Bertherton, *The Motion of Long Bubbles in Tubes*, Journal of Fluid Mechanics No. 10, p.166, 1961.
- [29] C.-W. Parker and G. M. Homsy, *Two-Phase Displacement in Hele Shaw Cells: Theory*, Journal of Fluid Mechanics No. 139, p.291, 1984.
- [30] R. Evans, *Microscopic Theories of Simple Fluids and Their Interfaces, Liquids at Interfaces*, Les Houches 1988, Course 1, p.1.

- [31] M. Schick, *Introduction to Wetting Phenomena*, Liquids at Interfaces, Les Houches 1988, Course 9, p.415.
- [32] D. Beysens, *Study of Wetting and Adsorption Phenomena at Fluid and Fluid Mixture Interfaces*, Liquids at Interfaces, Les Houches 1988, Course 10, p.499.
- [33] Peter Gravesen, Danfoss, private communication.
- [34] H. N. Man and X. D. Jing, *Pore Network Modelling of Electrical Resistivity and Capillary Pressure Characteristics*, Transport in Porous Media No. 41, p.263-286, 2000.
- [35] P. C. Reeves and M. A. Celia, *A Functional Relationship Between Capillary Pressure, Saturation and Interfacial Area as Revealed by a Pore-Scale Network Model*, Water Resources Research, Vol. 32, No. 8, p.2345-2358, August 1996.
- [36] H. Wong, S. Morris and J. Radke, *Three-Dimensional Menisci in Polygonal Capillaries*, Journal of Colloid and Interface Science, No. 148, p.317-336, 1992.
- [37] R. P. Mayer and R. A. Stowe, *Mercury Porosimetry - Breakthrough Pressure for Penetration Between Packed Spheres*, Journal of Colloid and Interface Science, No. 20, p.893-911, 1965.
- [38] L. W. Schwartz, H. M. Princen and A. D. Kiss, *On the Motion of Bubbles in Capillary Tubes*, Journal of Fluid Mechanics, Vol. 172, p.259-275, 1986.
- [39] H. K. Versteeg and W. Malalasekera, *An Introduction to Computational Fluid Dynamics: The Finite Volume Method*, Addison Wesley Longman Limited, Third Edition, 1998.
- [40] C. W. Hirt, B. D. Nichols and N. C. Romero, *SOLA-VOF, A Solution Algorithm for Transient Fluid Flow with Multiple Free Boundaries*, Los Alamos Scientific Laboratory, 1980.
- [41] W. J. Rider, D. B. Kothe, S. J. Masso, J. H. Cerutti and J. I. Hochstein, *Accurate Solution Algorithms for Incompressible Multiphase Flows*, AIAA, Paper 95-0699, 1995.
- [42] W. J. Rider, D. B. Kothe, S. J. Mosso, J. S. Brock and J. I. Hochstein, *Volume Tracking of Interfaces Having Surface Tension in Two and Three Dimensions*, AIAA, Paper 96-0859, 1996.
- [43] W. J. Rider and D. B. Kothe, *Comments on Modelling Interfacial Flows with Volume-Of-Fluid Methods*, Los Alamos National Laboratory, 1995.
- [44] Y. Y. Renardy, M. Renardy and V. Cristini, *A New Volume-of-Fluid Formulation for Surfactants and Simulations of Drop Deformation Under Shear at a Low Viscosity Ratio*, Eur. J. Mech. B, Fluids 0, p.1-13, 2001.
- [45] Y. C. Fung, *A First Course in Continuum Mechanics*, Prentice Hall, Third Edition, 1994.

- 
- [46] Martin Frøhling Jensen, Ph.D. student at MIC and Center for overflade analyse, Teknologisk Institut, Tåstrup.
- [47] W. Chang, D. Trebotich, L. P. Lee and D. Liepmann, *Blod Flow in Simple Microchannels*, First annual International IEEE-EMBS Special topic Conference on Microtechnologies in Medecine & Biology, October 12-14, 2000, Lyon, France.
- [48] P. Gravesen, J. Branebjerg and O. Søndergård Jensen, *Microfluidics - a review*, J. Micromech. Microeng. 3, p.168-182, 1993.
- [49] CJ Kim, *Mems Devices Based on the use of Surface Tension*, Mechanical and Aerospace Engineering Department, University of California.
- [50] Y.-S. Leung Ki, M. Kharouf, H. T. G. van Lintel, M. Haller and Ph. Renaud, *Bubble Engineering for Biomechanical Valving Applications*, 1st Annual International IEEE-EMBS Special Topic Conference on Microtechnologies in Medicine & Biology, October 12-14, 2000, Lyon, France.
- [51] P. F. Man, C. H. Mastrangelo, M. A. Burns and D. T. Burke, *Micro-fabricated Plastic Capillary Systems with Photo-Definable Hydrophilic and Hydrophobic Regions*, Paper presented at the 199 Transducers Conference, Sendai, Japan, June. 7-10 1999.
- [52] Nickolaj J. Petersen,  $\mu$ TAS, Mikroelektronik Centret - MIC, DTU, private communication.
- [53] CFD Research Corporation, Cummings Research Park, 215 Wynn Drive, Huntsville, AL 35805. In the present thesis version 6.6 (release 2002) of the program is utelized.

# Appendix A

## Curvature in $\mathbb{R}^2$ and $\mathbb{R}^3$

### A.1 Curvature in General

Curvature is regarded on a regular (or simple) surface  $S$ . That is a one-to-one  $C^k$  function  $\mathbf{x} : U \rightarrow E^n$  where  $U$  is an open subset of  $\mathbb{R}^2$  with co-ordinates  $u^1$  and  $u^2$ , at each point of  $D$   $\mathbf{x}_1 \times \mathbf{x}_2 \neq \mathbf{0}$ . When differentiating with respect to  $u^i$ , the notation  $\mathbf{x}_i$  is used, etc. If the surface is regular this also means that  $\mathbf{x}_1$  and  $\mathbf{x}_2$  are linearly independent and that the normal at a point on  $\mathbf{x}$  is given as  $\mathbf{n} = \mathbf{x}_1 \times \mathbf{x}_2$ . From the theory of differential geometry (Millman and Parker [5]) two fundamental forms and the important Weingarten map matrix are given as:

- The first fundamental form,

$$\mathbf{G} = [g_{ij}] = \langle \mathbf{x}_i, \mathbf{x}_j \rangle \quad (\text{A.1})$$

also yielding the useful relation  $g = \det \mathbf{G} = |\mathbf{x}_1 \times \mathbf{x}_2|^2$ .

- The second fundamental form,

$$[L_{ij}](\mathbf{n}) = \langle \mathbf{n}, \mathbf{x}_{ij} \rangle \quad (\text{A.2})$$

where the unit normal vector,  $\hat{\mathbf{n}} = \frac{1}{\sqrt{g}}\mathbf{n}$ , often is used.

- The Weingarten map matrix

$$\mathbf{L} = \mathbf{G}^{-1}[L_{ij}] \quad (\text{A.3})$$

If the unit normal is used in deriving  $[L_{ij}]$  then at a given point on  $\mathbf{x}$  the eigenvalues of  $\mathbf{L}$  are the two principal normal curvatures ( $\kappa_1 = \frac{1}{R_1}$  and  $\kappa_2 = \frac{1}{R_2}$ ). The corresponding eigenvectors are the two principal directions with respect to the  $\mathbf{x}_1, \mathbf{x}_2$ -coordinate system, that is in the tangent plane at the given point.

Furthermore the following curvatures are defined as

$$K = \kappa_1 \kappa_2 = \det(\mathbf{L}) \quad (\text{A.4})$$

$$H = \frac{1}{2}(\kappa_1 + \kappa_2) = \frac{1}{2}\text{trace}(\mathbf{L}) \quad (\text{A.5})$$

where  $K$  is the Gaussian curvature and  $H$  is the mean curvature. The mean curvature is the one being of special interest for us, as it appears in the Young-Laplace equation.

Note that if  $H$  is equal to zero at all points on the surface  $S$ ,  $S$  is called a minimal surface. Eq. (A.3) then yields,

$$\begin{aligned} H = \frac{1}{2}(\kappa_1 + \kappa_2) = \frac{1}{2}\text{trace}(\mathbf{L}) = 0 &\Leftrightarrow \\ \text{trace}(\mathbf{L}) = 0 &\Leftrightarrow \\ g_{11}L_{22} - 2g_{12}L_{12} + g_{22}L_{11} = 0 &\quad (\text{A.6}) \end{aligned}$$

where we have used the complement method to find the inverse of  $\mathbf{G}$ . Eq. (A.6) is fundamental in the theory of minimal surfaces.

## A.2 Interpretation of curvature in $\mathbb{R}^2$

A easy way to determine and understand curvature on a plane curve is to approximate it with a circular motion at every point. Thus using the well known formulae from mechanics  $a = v^2/R$  from circular motion. The curve is described by a vector function (parametric representation)  $\mathbf{r}(t) = (x(t), y(t))$  with velocity  $\mathbf{v}(t) = (x'(t), y'(t))$  and acceleration  $\mathbf{a}(t) = (x''(t), y''(t))$  (a graph,  $y = y(x)$ , is parametrized by  $\mathbf{r}(x) = (x, y(x))$ , etc.).

The acceleration predicts the change in velocity both directional and in size. It is hence logic to divide into two components, a normal and a tangential, i.e.,

$$\mathbf{a} = \mathbf{a}_\perp + \mathbf{a}_\parallel \quad (\text{A.7})$$

As the velocity is always tangential to the curve we get by simple projection (on  $\mathbf{v}$  and  $\hat{\mathbf{v}}$ ),

$$\mathbf{a}_\perp = \frac{\mathbf{a} \cdot \hat{\mathbf{v}}}{\hat{\mathbf{v}}^2} \hat{\mathbf{v}} \quad \text{and} \quad \mathbf{a}_\parallel = \frac{\mathbf{a} \cdot \mathbf{v}}{\mathbf{v}^2} \mathbf{v}. \quad (\text{A.8})$$

The radii of curvature is hence

$$R = \frac{|\mathbf{v}|^2}{|\mathbf{a}_\perp|} = \frac{|\mathbf{v}|^3}{|\mathbf{a} \cdot \hat{\mathbf{v}}|}, \quad (\text{A.9})$$

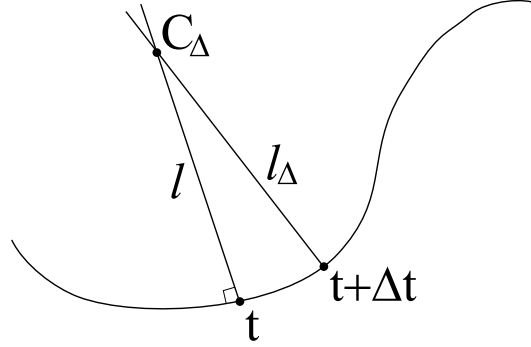
and for a graph  $y = y(x)$  it yields (as mentioned in Probstein [2] and Adamson [3])

$$R = \frac{(1 + y'(x)^2)^{\frac{3}{2}}}{y''(x)}. \quad (\text{A.10})$$

The same result is now obtained by a more strict differential approach, sketched in Fig. (A.1). The intersection of two normal lines "approaching" one another ( $\Delta t \rightarrow 0$ ) is the center of curvature.

For any point  $\mathbf{x}$  on the normal line,  $l$ , at time  $t$  we have the relation,

$$l: \quad \mathbf{v}(t) \cdot (\mathbf{x} - \mathbf{r}(t)) = 0 \quad (\text{A.11})$$

Figure A.1: Differential approach to curvature in  $\mathbb{R}^2$ .

In the same manner a point on the line  $l_\Delta$  at time  $t + \Delta t$ , with parameter  $s$ , is given by,

$$l_\Delta : \quad \mathbf{x} = \mathbf{r}(t + \Delta t) + s\hat{\mathbf{v}}(t + \Delta t) = (\mathbf{r}(t) + \Delta t\mathbf{v}(t) + \dots) + s(\hat{\mathbf{v}}(t) + \Delta t\hat{\mathbf{a}}(t) + \dots) \quad (\text{A.12})$$

where a Taylor expansion around  $t$  has been made to first order. The intersection of  $l$  and  $l_\Delta$  is found by inserting Eq. (A.12) into Eq. (A.11) yielding

$$\begin{aligned} \mathbf{v}(t) \cdot ((\mathbf{r}(t) + \Delta t\mathbf{v}(t) + \dots) + s(\hat{\mathbf{v}}(t) + \Delta t\hat{\mathbf{a}}(t) + \dots) - \mathbf{r}(t)) &= 0 \quad \Rightarrow \\ s &= -\frac{\mathbf{v}^2}{\hat{\mathbf{a}} \cdot \mathbf{v}} = \frac{\mathbf{v}^2}{\mathbf{a} \cdot \hat{\mathbf{v}}}, \quad \text{for } \Delta t \rightarrow 0 \end{aligned} \quad (\text{A.13})$$

The center of curvature is found, by inserting Eq. (A.13) into Eq. (A.12) with  $\Delta t \rightarrow 0$ , as

$$\overline{OC} = \mathbf{r} + \frac{\mathbf{v}^2}{\mathbf{a} \cdot \hat{\mathbf{v}}} \hat{\mathbf{v}} \quad (\text{A.14})$$

and hereby getting

$$R = \frac{\mathbf{v}^2}{|\mathbf{a} \cdot \hat{\mathbf{v}}|} |\hat{\mathbf{v}}| = \frac{|\mathbf{v}|^3}{|\mathbf{a} \cdot \hat{\mathbf{v}}|}. \quad (\text{A.15})$$

### A.3 Curvature of a Surface of Revolution

In many problems involving a liquid-gas interface the interface can because of symmetry be described as a surface of revolution. In that case the surface is described in one plane by a graph, say of a function  $y(x)$ , see Fig. (A.2). The two main radii of curvature are (see the first section) firstly  $R_1$  the curvature of  $y(x)$  in the  $xy$ -plane given by Eq. (A.10). Secondly  $R_2$  the curvature in a plane perpendicular to the  $xy$ -plane intersecting as the normal to the curve  $y(x)$ .  $R_2$  is hence given by extending the normal to the profile until it hits the axis of revolution as shown in Fig. (A.2).

Having Fig. (A.2) in mind simple geometry yields the relations

$$\begin{aligned} \sin \theta &= \frac{x}{R_2} \\ \tan \theta &= \frac{\sin \theta}{\cos \theta} = y' \\ \cos \theta &= \frac{1}{(1+y'^2)^{1/2}} \end{aligned}$$

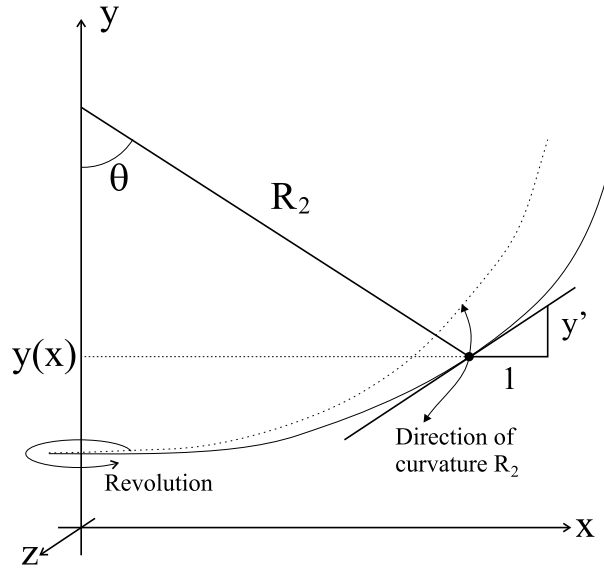


Figure A.2: Curvature of a surface of revolution.

inserting these expressions in one another easily yield

$$\frac{1}{R_2} = \frac{y'}{x(1+y'^2)^{1/2}} \tag{A.16}$$

The two curvatures could equally have been found using the theory from the first section setting

$$\mathbf{x}(s, t) = (s \cos t, y(s \cos t), s \sin t), \quad t \in [0, 2\pi], \quad s \in [0, x_{max}]. \tag{A.17}$$

# Appendix B

## Poiseuille and Couette Flow

The Couette and Poiseuille pressure driven steady state incompressible flows are here shortly presented. The flows are described by the incompressible form of the Navier-Stokes equation and the continuity equations, Eqs. (2.9a) and (2.9b).

### B.1 Couette Flow

The planar pressure driven flow, Fig. B.1, between two stationary plates is found by solving Eq. (2.9b) in 2D ( $\mathbf{u} = (u, v)$ ).

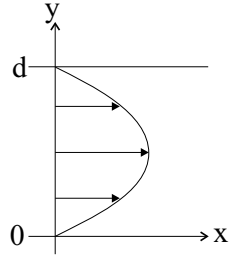


Figure B.1: Characteristic parabolic velocity profile of the planar pressure driven Couette flow.

$v = 0$  yields  $\partial P / \partial y = 0$  so that  $P = P(x)$  and Eq. (2.9b) reduces to,

$$\frac{dP(x)}{dx} = \mu \frac{d^2 u(y)}{dy^2}. \quad (\text{B.1})$$

Left and right side depend on  $x$  and  $y$ , respectively so they are equal a common value, say  $-\Gamma$ . Using no-slip conditions at  $y = 0$  and  $y = d$  readily yields,

$$P(x) = P_0 - \Gamma x \quad (\text{B.2})$$

$$u(y) = \frac{\Gamma}{2\mu} y(d - y) \quad (\text{B.3})$$

$$U = \frac{1}{d} \int_0^d u(y) dy = \frac{\Gamma d^2}{12\mu} \quad (\text{B.4})$$

$$Re = \frac{\rho U d}{\mu} = \frac{\rho \Gamma d^3}{12\mu^2}. \quad (\text{B.5})$$

Where  $P_0$  is a constant,  $-\Gamma$  is the pressure gradient,  $U$  the mean flow rate, and  $Re$  the Reynolds number of the system.

## B.2 Poiseuille Flow

The pressure driven flow in an infinitely long cylindrical tube of radius  $a$  is rotationally symmetric along its axis. In cylindrical coordinates the velocity field is:  $\mathbf{u} = (u_r, v_\theta, w_z)$ . By simple geometric considerations the velocity field in the tube must be on the form,

$$\mathbf{u} = u(r)\mathbf{e}_z = (0, 0, u(r)). \quad (\text{B.6})$$

It is supposed that there are no periodic solutions in  $\theta$ . Using the cylindrical form of the  $\nabla$  operator in Eq. (2.9b) and the velocity field given above the solution is readily found as,

$$u(r) = \frac{\Gamma}{4\mu}(a^2 - r^2), \quad \Gamma = -\frac{dP}{dz} = -\frac{\Delta P}{L} \quad (\text{B.7})$$

$$u_{max} = u(0) = \frac{\Gamma a^2}{4\mu} \quad (\text{B.8})$$

$$\begin{aligned} U &= \frac{1}{A} \int_A u(r) dA \\ &= \frac{1}{a^2\pi} \int_0^{2\pi} \int_0^a u(r) r dr d\theta = \frac{\Gamma a^2}{8\mu} \end{aligned} \quad (\text{B.9})$$

$$Re = \frac{\rho 2aU}{\mu} = \frac{\rho \Gamma a^3}{4\mu^2}. \quad (\text{B.10})$$

## Appendix C

# Exact Solution of Capillary Rise

The exact equation for a meniscus in a cylindrical capillary tube, Eq. (5.7) is here solved numerically with MATLAB using a simple shoot method combined with the Newton-Rapton formula.

### C.1 Method

The given parameters in the problem are radius  $a$ , surface tension  $\sigma$ , contact angle  $\theta$ , and density  $\rho$ . The goal is to determine  $H$  being the distance from still water to the meniscus apex as seen on Fig. C.1.

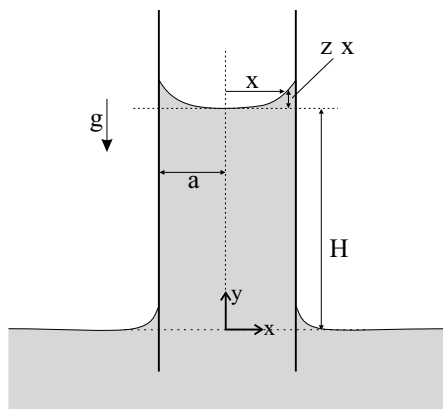


Figure C.1: Dimensions and definitions of the capillary rise problem. The distance from still water is  $y(x)$ . The relation  $y(x) = H + z(x)$  is used in solving the problem.

To simplify the numerical procedure the  $z(x)$  variable defined by  $z(x) = y(x) - H$  is introduced in Eq. (5.7) yielding

$$\rho g(z + H) = \sigma \left( \frac{z''}{(1 + z'^2)^{3/2}} + \frac{z'}{x(1 + z'^2)^{1/2}} \right). \quad (\text{C.1})$$

The idea behind the transformation is to make  $H$  the tuning parameter in the shooting procedure. Eq. (C.1) is a second order ODE with the boundary

condition,

$$z = 0 \quad \text{for} \quad x = 0 \quad (\text{C.2})$$

$$\frac{dz}{dx} = \tan(\pi/2 - \theta) \quad \text{for} \quad x = a. \quad (\text{C.3})$$

To solve the problem a set of correct initial conditions is introduced and  $H$  is used to tune in on the boundary condition at  $x = a$ . The initial conditions are

$$z = 0 \quad \text{for} \quad x = 0 \quad (\text{C.4})$$

$$\frac{dz}{dx} = 0 \quad \text{for} \quad x = 0. \quad (\text{C.5})$$

The initial condition problem is solved with the MATLAB `ode15s.m` function.  $H$  is varied to make the boundary conditions fit, i.e., finding the zero of the error function,

$$\varepsilon(h) = \tan(\pi/2 - \theta) - \left. \frac{dz}{dx} \right|_{x=a}. \quad (\text{C.6})$$

The zero point is easily found by using a Newton-Rapton iteration formula. The procedure converges satisfactory within 4 or 5 iterations. Note that the initial guess on  $H$  is given by the simple solution Eq. (5.2). The source code is located in the "Source Code" section.

## C.2 Example

As an example imagine water rising in a PMMA cylindrical tube, with parameters:  $\rho = 1000 \text{ kg/m}^3$ ,  $\sigma = 0.072 \text{ N/m}$ ,  $g = 9.82 \text{ m/s}^2$ ,  $\theta = 73^\circ$ , and  $a = 100 \mu\text{m} = 0.1 \text{ mm}$ . The problem yields a water column height of  $H \approx 4.3 \text{ cm}$ . The meniscus profile is presented in Fig. C.2, and the following data is presented:

```

Number of iterations: 4
Absolute error in dz/dx(a): 4.7155e-009
Capillary length D_c: 2.7078 mm
Meniscus height h: 0.015294 mm
Water column height H is: 4.2856 cm
Absolute deviation in H from simple theory: 0.017125 mm

```

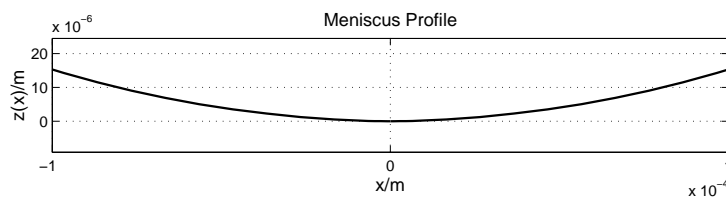


Figure C.2: The meniscus profile at equilibrium.

The exact solution does only deviate slightly from the approximative simple solution. This is obvious as the meniscus height  $h$  is much smaller than the capillary length,  $h \ll \Delta_c$ . Surface tension phenomenon are hence much more important than gravitation.

## C.3 Source Code

**Main Program** (`caprise.m`):

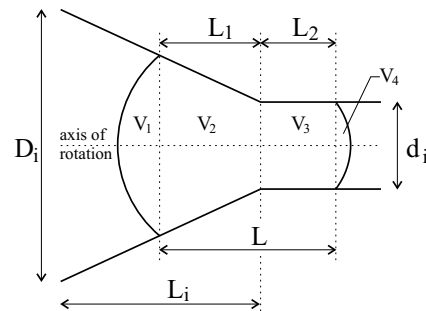
**Function 1** (`rhs.m`):



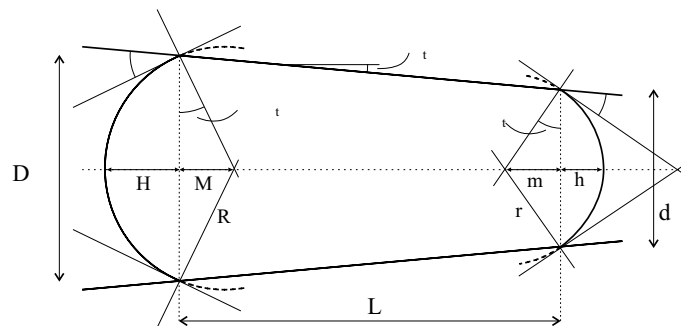
# Appendix D

## Clogging Program

To enable comparison of the tapered channel model (a slightly extended model of the one described in Sec. 5.2) with simulations a MATLAB program was implemented. Volume or area conservation of an initial bubble is utilized to find relevant bubble geometry and hereby determine relevant physical data (pressure, curvature, dimensions, area, etc.).



(a) Geometry of the extended tapered channel geometry with appropriate labeling.



(b) The bubble in a tapered channel Fig. 5.5 from Sec. 5.2.

Figure D.1: Full geometry of the tapered channel and labels used in the clogging program.

## D.1 Method and Discussion

The basic idea behind the program is to find the geometric relation between the left diameter  $D$ , the right diameter  $d$ , and the length  $L$  (see Fig. D.1), having a known initial bubble volume  $V_b$  or area  $A_b$ . The 3D axisymmetric case using volume conservation is in the following discussed. The method for the 2D case is conceptually identical.

As depicted on Fig. D.1(a) the bubble is divided into the four volume slices  $V_1$  to  $V_4$  ( $V_3$  might be zero if  $d > d_i$ ). Hence for any given  $D$ ,  $d$  or  $L$  value the program solves the equation,

$$V_1 + V_2 + V_3 + V_4 = V_b \Leftrightarrow \quad (\text{D.1})$$

$$\begin{aligned} \frac{1}{3}\pi H^2(3R - H) + \frac{1}{3}\pi L_1((d/2)^2 + dD/4 + (D/2)^2) \\ + (L - L_1)\pi(d_i/2)^2 + \frac{1}{3}\pi h^2(3r - h) = V_b \end{aligned} \quad (\text{D.2})$$

with respect to  $D$ ,  $d$  or  $L$  depending on the situation. Where  $L = L_1 + L_2$  and

$$d = D - 2 \tan \theta_t L \quad (\text{D.3})$$

$$d = d_i \quad \text{if} \quad d < d_i \quad (\text{D.4})$$

$$L_1 = L \quad \text{if} \quad d > d_i \quad (\text{D.5})$$

$$L_1 = \frac{D - d_i}{2 \tan \theta_t} \quad \text{if} \quad d < d_i. \quad (\text{D.6})$$

The volumes are easily found as the geometry is axis-symmetric. The program uses the MATLAB `fsolve.m` standard function to solve the equations. The source code is located at the end of this Appendix. After determining the geometric factors the relevant curvatures  $1/R$  and  $1/r$ , the pressure drop due to surface tension Eq. (5.14) and the overall surface area of the bubble are calculated. All data is further plotted as a function of  $D$ .

To illustrate the program the following data is chosen.  $D_i = 300 \mu\text{m}$ ,  $d_i = 100 \mu\text{m}$ ,  $\tan \theta_t = 1/5$ ,  $\theta_c = 73^\circ$ ,  $\sigma = 0.0725 \text{ N/m}$  and an initial bubble volume equal to that of a sphere with radius  $R_b = 95 \mu\text{m}$ . The data is presented in Fig. D.2.

Though this section is a "program Appendix" it is worth noticing how the curvatures and hence the pressures seem discontinuous at the point where the right side of the bubble enters the non-tapered section (when  $d = d_i = 100 \mu\text{m}$ ). This is because the tapering angle is discontinuous at this point.

The passage is actually not discontinuous. A method to handle the passage has been implemented by introducing a decreasing radius of curvature at that edge point (see Fig. D.3). The right curvature,  $r$ , decreases from  $r = d/(2 \cos(\theta_c + \theta_t))$  to  $r = d_i/(2 \cos \theta_c)$  continuously while volume conservation is obviously still required. The actual implementation of the method increases the complexity of the program as it requires a shift in variable parameters from  $d$  to  $L$  and finally to  $D$ .

On Fig. D.4 a zoom is made of Fig. D.2(b) just at the transition area, notice how the length  $L$  decreases a little while the bubble enters the non-tapered

region. The overall relative change in bubble volume is calculated and found to be about the order of magnitude of the machine precision.

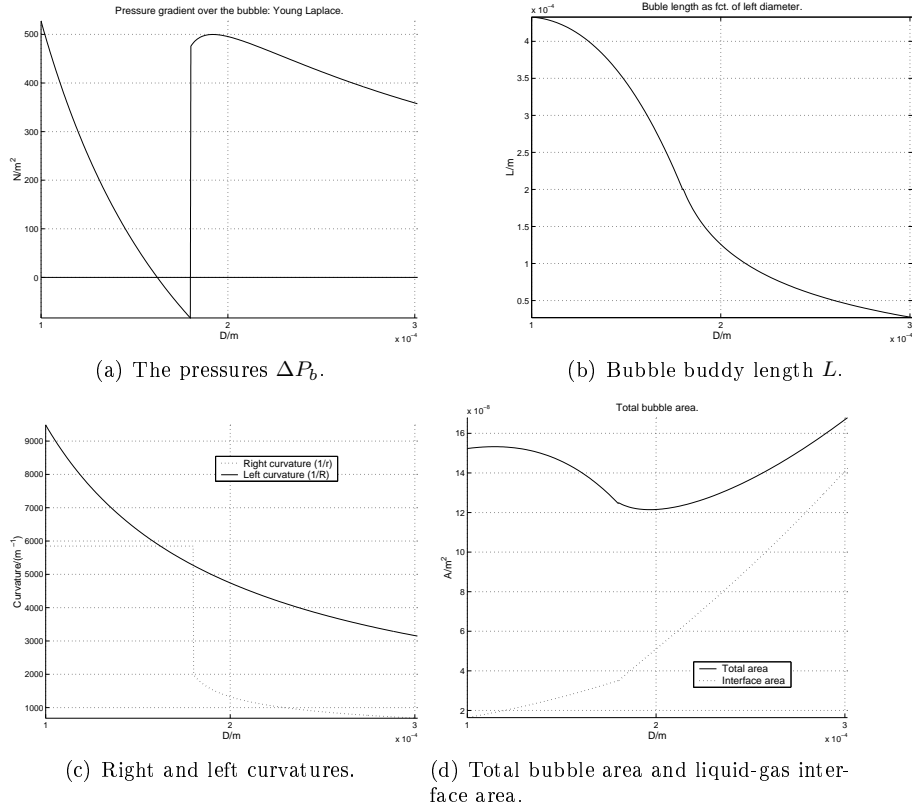


Figure D.2: An example of the different results delivered by the clogging program.

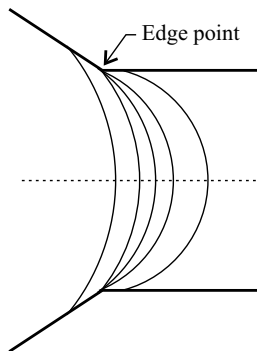


Figure D.3: Continuous deformation of the meniscus about the edge points (transition area).

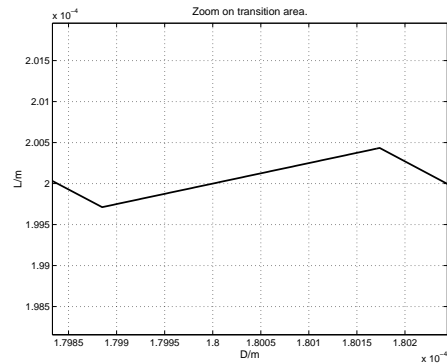


Figure D.4: Zoom on transition area for  $L$  as function of  $D$ .

## D.2 Source Code

The main program is roughly similar for 2D and 3D bubbles. The essential difference lies in the four subroutines `volume` in 3D and `area` in 2D. Only the 3D version of the main program is included.

**Main Program 3D** (`clogging02.m`):

**Volume function 1** (`volume0a.m`):

**Volume function 2** (`volume0b.m`):

**Volume function 3** (`volume0c.m`):

**Volume function 4** (`volume0d.m`):

**Area function 1** (`area0a.m`):

**Area function 2** (`area0b.m`):

**Area function 3** (`area0c.m`):

**Area function 4** (`area0d.m`):



## Appendix E

# Interface in Tubes of Constant Cross Section

The shape of a static liquid-gas interface in a capillary tube is a function of the tube geometry. The problem of finding the interface curvature/shape can in some cases be simplified. For the case of tubes with constant or slowly varying cross sections the problem condenses to a 2D description. The method is based on an energy and work consideration.

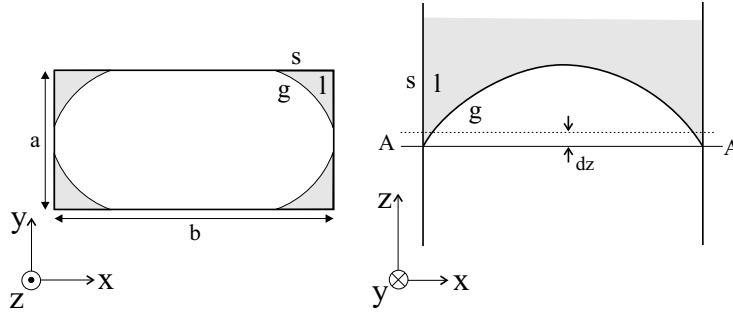


Figure E.1: Two cross sections of a rectangular tube with a gas-liquid interface. Solid (s), liquid (l), and gas (g) regions are marked.

A capillary of rectangular cross section is depicted in Fig. E.1. Firstly, if the contact angle  $\theta$  is less than some critical value  $\theta_c$  only portions of the gas perimeter,  $L$ , are in contact with the solid walls and

$$L = L_{gl} + L_{gs}, \quad (\text{E.1})$$

where  $s$ ,  $l$ , and  $g$  stand for solid, liquid and gas, respectively. At equilibrium the pressure across the interface  $\Delta P_i$  is constant. The pressure volume work associated with an infinitesimal displacement  $dz$  of the interface is equal to the net change in surface energies. The work is given by

$$\Delta P_i dV = \sigma_{gl} dS_{gl} + \sigma_{gs} dS_{gs} + \sigma_{sl} dS_{sl}, \quad (\text{E.2})$$

where  $\sigma$  is the interface tension (surface free energy),  $dS$  are the changes in respective surface areas and  $dV$  the change in gas volume. The interface shape

above plane  $A-A$  does not change with the displacement  $dz$ , hence

$$dV = Adz, \quad (\text{E.3})$$

$$dS_{gl} = L_{gl}dz, \quad (\text{E.4})$$

$$dS_{gs} = -dS_{ls} = L_{gs}dz, \quad (\text{E.5})$$

where  $A$  represents the gas cross section area at  $A-A$  in the  $xy$ -plane. Using the Young equation Eq. (4.5) (where  $\sigma \equiv \sigma_{gl}$ ) together with Eqs. (E.3), (E.4), and (E.5) yields,

$$\Delta P_i = \sigma \left( \frac{L_{gl} + L_{gs} \cos \theta}{A} \right)_{\min} = \sigma \left( \frac{L'}{A} \right)_{\min}, \quad (\text{E.6})$$

where  $\theta$  is the static contact angle. As the meniscus is in equilibrium the right hand side of Eq. (E.6) is at its minimum. So, in order to find the correct  $\Delta P_i$  a general expression for the term in brackets  $L'/A$  in Eq. (E.6) is to be found and minimized with respect to an introduced parameter. Eq. (E.6) is valid for any cross section shape and can in most simple geometries be determined analytically.

Finally when the contact angle is greater than the critical value  $\theta_c$  the gas bubble totally wets the solid and  $L_{gl} = 0$ . In this case the interface is generally found to be part of an ellipsoid or a sphere. The shape and hence  $\Delta P_i$  is now found according to the contact angle description. The following example is meant to illustrate the difference.

The transition or critical contact angle is found when the pressure drop  $\Delta P_i$  defined by the two methods is identical. At this point both methods predict the same minimum energy configuration.

### Example

The case of a rectangular capillary, also depicted on Fig. E.2, is illustrated in the following example.

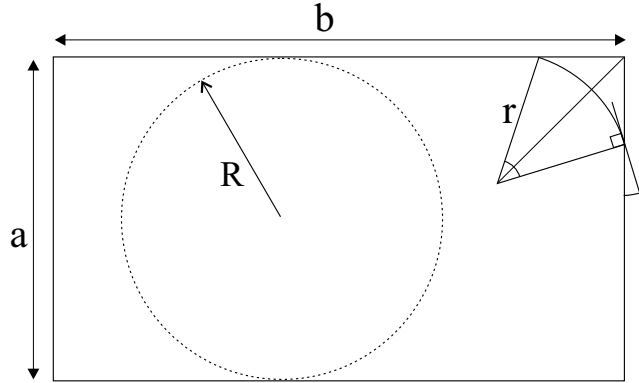


Figure E.2: Cross section of a rectangular capillary with relevant parameters.

**1:** For  $\theta < \theta_c$  and by use of simple geometry and the introduction of the parameter  $r$ , on Fig. E.2, a general expression for  $L'/A$  is found to be

$$\frac{L'}{A} = \frac{2}{R} \frac{(\pi - 4\theta)\tilde{r} + [(2 + 2N) - 4\sqrt{2}\tilde{r}\sin(\omega/2)] \cos \theta}{4N - 4\tilde{r}^2 \sin^2(\omega/2) + 2\tilde{r}^2(\omega - \sin \omega)} \quad (\text{E.7})$$

with

$$\omega = \frac{\pi}{2} - 2\theta, \quad a = 2R, \quad b = Na, \quad \tilde{r} = \frac{r}{R}, \quad (\text{E.8})$$

where  $a$  and  $b$  are the rectangle dimensions,  $\theta$  the contact angle,  $N$  the aspect ratio,  $R$  the radius of the largest inscribed circle, and  $\tilde{r}$  is the dimensionless radius of curvature. The minimum of Eq. (E.7) is found by a MATLAB program made by the author.

**2:** For  $\theta > \theta_c$  the gas totally wets the solid walls and the pressure drop is approximated by

$$\Delta P_i = \sigma \left( \frac{1}{R_1} + \frac{1}{R_2} \right) \quad (\text{E.9})$$

where

$$R_1 = \frac{a}{2 \cos \theta} \quad \text{and} \quad R_2 = \frac{b}{2 \cos \theta}. \quad (\text{E.10})$$

The two radii of curvatures are found according to the principles discussed in Sec. 5.2.

The two described pressure drops are labelled with the subscript 1 and 2 respectively. The critical contact angle  $\theta_c$  is found when one of the following conditions is fulfilled,

$$L_{sg} + L_{lg} > L_{total} = 2a + 2b \quad (\text{E.11})$$

$$\frac{L'}{A} \quad \text{has no more minimum} \quad (\text{E.12})$$

$$\Delta P_{i,1} = \Delta P_{i,2}. \quad (\text{E.13})$$

The first condition is geometrical whereas the last two conditions specify that the utilized theory should render an energy minimum.

The dimensionless curvature  $C_m = 2RH = R\Delta P_i/\sigma$  discussed in Sec.5.3 is found and plotted as a function of the contact angle  $\theta$ , see Fig. E.3. The critical contact angle  $\theta_c$  is also found and presented in the plot title. The dotted curves represent the prediction of the false theory in the specific region delimited by  $\theta = \theta_c$ . The results are found to agree with numerical solution of the full 3D Young-Laplace equation made by Wong *et al.* [36].

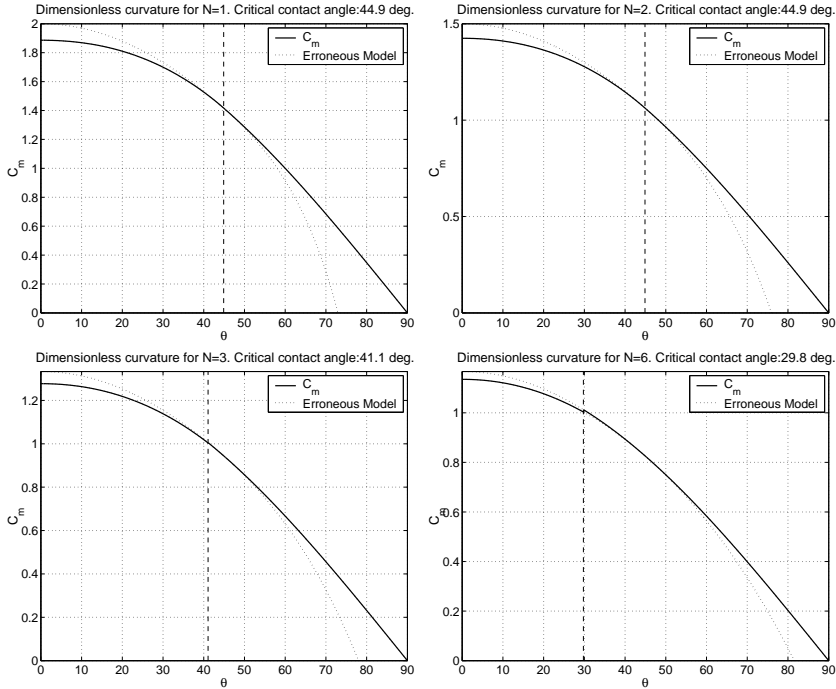


Figure E.3: Dimensionless curvature  $C_m$  plotted as function of contact angle. Four aspect ratios are presented  $N = 1$ ,  $N = 2$ ,  $N = 3$ , and  $N = 6$ . The predictions of the erroneous models are plotted as dotted curves the transition  $\theta_c$  is marked with a vertical dashed line.

## Appendix F

# Temperature Dependence of Surface Tension

The temperature dependence of the surface tension is in the following illustrated by a thought experiment depicted in Fig. F.1. The system consists of liquid filling a box having a sliding cover. The solid-liquid interfacial tension is zero and the liquid-gas tension is  $\sigma$ . The temperature of the system is constant as well as the liquid volume.

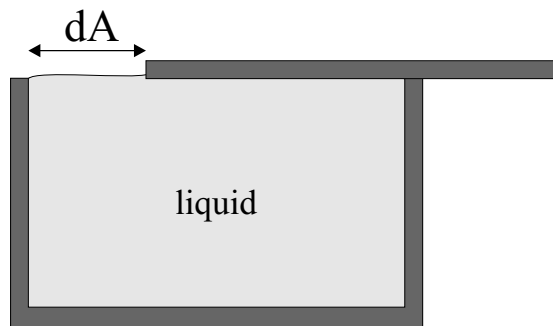


Figure F.1: Set-up consisting of box with a moving lid filled with a liquid.

The cover is moved to uncover an area  $dA$  of liquid. The process is reversible and the work required is  $dW = \sigma dA$ . The following relations follow from thermodynamics:

$$dU = dQ + dW \quad \text{first law of thermo.}, \quad (\text{F.1})$$

$$dF = dU - SdT - TdS \quad \text{follows def. of } F, \quad (\text{F.2})$$

$$dQ = TdS = TS^s dA \quad \text{reversible process.} \quad (\text{F.3})$$

where the superscript  $s$  designates a surface quantity (per area), so that  $dS = S^s dA$ .

Using Eq. (F.1) to Eq. (F.3) at constant temperature,  $dT = 0$ , yields

$$dF = dW = \sigma dA \Rightarrow \sigma = F^s = \left( \frac{dF}{dA} \right)_{T,V}, \quad (\text{F.4})$$

The expression is exactly the definition for surface tension given in Chap. 3. Now, finding the dependence on temperature

$$\left(\frac{dF}{dT}\right)_V = -S \Rightarrow \frac{d\sigma}{dT} = \left(\frac{dF^s}{dT}\right)_V = -\left(\frac{dS}{dA}\right)_V = -S^s < 0. \quad (\text{F.5})$$

As the process is reversible  $dQ = TdS = TS^s dA$  hinting that as  $dS$  decreases  $dA$  must decrease, i.e.,  $dS/dA > 0$ .

## Appendix G

# Flow Around a Bubble with Marangoni effects

In this appendix the effects of gradients in surface tension along a bubble are illustrated. The situation is highly simplified, but still describes some of the physical aspects involved. Consider a bubble moving to the left, in a capillary tube, with speed  $-U_0$  with  $U_0 > 0$ , driven by a pressure gradient  $\Gamma = \frac{dP}{dx} > 0$ . The problem is rotational symmetric and the bubble is in a static frame of reference and the walls seem to move at a speed  $U_0$ , see Fig. G.1. The flow is only considered in the wetting film far from the bubble ends.

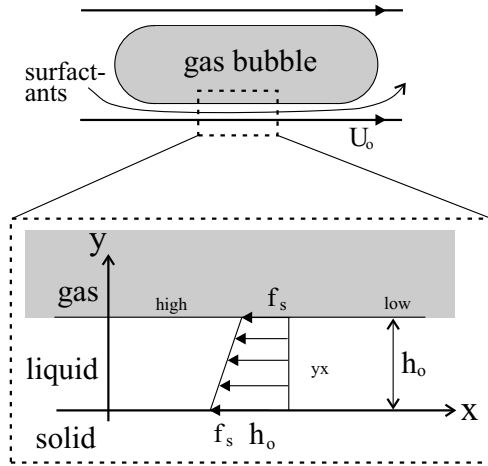


Figure G.1: The gas bubble moving to the left with speed  $|U_0|$  is in a static reference frame. Corresponding to the walls of the tube are moving to the right with speed  $U_0$ . The flow in the wetting film of thickness  $h_0$  is considered. The presence of surfactants create gradients in the surface tension,  $\sigma_{\text{high}} > \sigma_{\text{low}}$  yielding a shear stress at the interface.

Now, imagine that surfactants are present on the liquid-gas interface. The flow will increase the concentration on the interface lying at the back of the bubble (to the right)<sup>1</sup>. This situation will create a gradient in the surface tension along the liquid-gas interface, i.e., a tangential stress

$$\tau_0 = -f_s = \frac{d\sigma}{dx} < 0, \quad f_s > 0 \quad \text{for } y = h_0, \quad (\text{G.1})$$

<sup>1</sup>In a more detailed model the transport of the surfactants on the interface should be included.

where  $f_s$  is the magnitude of the effective tangential force per unit area and  $h_0$  the film thickness. The problem at hand is steady state and uniform in the  $x$  direction. Gravity is neglected. The velocity field is hence given as  $\mathbf{u} = (u(y), 0)$ . The momentum equation then reduces to

$$\frac{\partial^2 u}{\partial y^2} = \frac{\Gamma}{\mu_l}, \quad (\text{G.2})$$

where  $\Gamma$  is a driving pressure gradient and  $\mu_l$  is the dynamic viscosity of the liquid. The respective boundary conditions are,

$$u = U_0, \quad \text{for } y = 0, \quad (\text{G.3})$$

$$(\mu_l - \mu_g) \frac{\partial u}{\partial y} = \tau_0 = -f_0, \quad \text{for } y = h_0, \quad (\text{G.4})$$

$\mu_g$  is the dynamic viscosity of the gas. The second condition follows from Newton's formula (see Chap. 2). In the absence of surface tension,  $\tau_0 = 0$ , Eq. (G.4) represents continuity in the stress tensor. Having  $\mu_g \ll \mu_l$  Eqs. (G.2), (G.3), and (G.4) are easily solved yielding

$$u(y) = \frac{1}{2} \frac{\Gamma}{\mu_l} y^2 - \frac{1}{\mu_l} (f_s + h_0 \Gamma) y + U_0 \quad (\text{G.5})$$

$$\tau_{yx}(y) = \mu_l \frac{\partial u}{\partial y} = \Gamma(y - h_0) - f_s \quad (\text{G.6})$$

where  $\tau_{yx}$  is the shear stress. Note that for  $f_s = 0$  the shear stress vanishes at the liquid-gas interface.

# Appendix H

## Excel Simulation Sheets

### H.1 Couette Flow

#### Test case 1 - 2D Couette flow.

Grid 1: 8\*32 cells  
Grid 2: 16\*64 cells  
Grid 3: 32\*128 cells

Data:	Theoretical results:
$\Delta P/Pa= 2,00E+02$	$U/(m/s)= 1,949$
$L/m= 1,60E-03$	$u_{max}/(m/s)= 2,924$
$d/m= 4,00E-04$	
$\mu/(kg/sm)= 8,55E-04$	$Re= 914,697$
$G/(Pa/m)= 1,25E+05$	
$\rho/(kg/m^3)= 1,00E+03$	

#### Min. Residual: 1e-2

	U	U error (%)	# iterations	calc. time (/min)
Grid 1	1,198	38,558	40	-
Grid 2	1,082	44,483	102	-
Grid 3	1,129	42,108	266	2

#### Min. Residual: 1e-3

	U	U error (%)	# iterations	calc. time (/min)
Grid 1	1,865	14,586	775	-
Grid 2	1,823	6,501	1452	-
Grid 3	1,836	5,839	2793	21

#### Min. Residual: 1e-4

	U	U error (%)	# iterations	calc. time (/min)
Grid 1	1,905	2,299	2108	-
Grid 2	1,929	1,027	3477	-
Grid 3	1,936	0,693	6627	48

## H.2 Poiseuille Flow

### Test case 2 - 3D Poiseuille flow.

Data:	Theoretical results:
$\Delta P/P_a = 1,00E+02$	$U/(m/s) = 0,365$
$U/m = 9,00E-04$	$u_{max}/(m/s) = 0,731$
$a/m = 1,50E-04$	
$\mu/(kg/sm) = 8,55E-04$	$Re = 128,629$
$G/(Pa/m) = 1,11E+05$	
$\rho/(kg/m^3) = 1,00E+03$	

	U/(m/s)	U error (%)	max residual	# cells	# iterations
Grid 1	0,356	2,623	1,42E-08	6144	200
Grid 2	0,365	0,251	1,84E-05	5880	200
Grid 3	0,366	0,143	1,47E-08	5880	200

	umax/(m/s)	umax error (%)	max residual	# cells	# iterations
Grid 1	0,721	1,414	1,42E-08	6144	200
Grid 2	0,704	3,705	1,84E-08	5880	200
Grid 3	0,703	3,835	1,47E-08	5880	200

	U/(m/s)	U error (%)	max residual	# cells	# iterations
Grid 1	0,3577	2,1360	5,44E-14	6144	800
Grid 3	0,3678	0,6410	8,59E-11	5880	450
Grid 3	0,3679	0,6438	5,83E-14	5880	800
Grid 3	0,3678	0,6437	1,47E-14	5880	1200
Grid 3	0,3678	0,6437	1,18E-16	5880	2000

	umax/(m/s)	umax error (%)	max residual	# cells	# iterations
Grid 1	0,7077	3,1839	5,44E-14	6144	800
Grid 3	0,7077	3,1880	8,59E-11	5880	450
Grid 3	0,7077	3,1853	5,83E-14	5880	800
Grid 3	0,7077	3,1841	1,47E-14	5880	1200
Grid 3	0,7077	3,1840	1,18E-16	5880	2000

### Grid Orthogonality Data

#### Grid 1: Bad orthogonality:

Summary of Face Angles (% of faces with):

20.000 < angle < 30.000 =	0.987 %
30.000 < angle < 40.000 =	0.987 %
40.000 < angle < 50.000 =	1.974 %
50.000 < angle < 60.000 =	10.855 %
60.000 < angle < 70.000 =	14.803 %
70.000 < angle < 80.000 =	15.789 %
80.000 < angle < 90.000 =	54.605 %

#### Grid 2: Good orthogonality and good aspect ratios:

Summary of Face Angles (% of faces with):

60.000 < angle < 70.000 =	1.054 %
70.000 < angle < 80.000 =	12.645 %
80.000 < angle < 90.000 =	86.302 %

#### Grid 3: Good orthogonality, bad aspect ratios and good resolution at walls:

Summary of Face Angles (% of faces with):

60.000 < angle < 70.000 =	3.161 %
70.000 < angle < 80.000 =	12.645 %
80.000 < angle < 90.000 =	84.194 %

## H.3 2D Static Interface

### Test case 3 - 2D Static Meniscus

To reach the static position the meniscus deforms from a straight position to the static position. In the static position it has reached a minimum energy configuration. Grid fineness and aspect ratios are in the following tested.

Width resolution: N  
 Aspect ratio of a cell: a/b  
 Contact angle:  $\theta$   
 $\sigma$ (N/m): 7.25E-02  
 Width d(m): 3.00E-04



Auto time steps.  
 Max dt 1e-4 s  
 CFL: 0.2

N=8  $\theta$ (deg.)= 70 No damping.

a/b	Numerical $\Delta P$ (Pa)	Theoretical		% Deviation - Error $\Delta P$
		$\gamma$ (1/m)	$\Delta P$ (Pa)	
1	150	6,67E+03	4,88E+02	69,0

Note: The numerical results are quite unprecise i.e. hard to collect.

N=8 Damping.

a/b	$\theta$ (deg.)	Numerical $\Delta P$ (Pa)	Theoretical		% Deviation - Error $\Delta P$
			$\gamma$ (1/m)	$\Delta P$ (Pa)	
1	70	143	2,28E+03	1,65E+02	13,5
1	50	315	4,29E+03	3,11E+02	1,4
1	30	457	5,77E+03	4,19E+02	9,2

Note: Highly increased resolution with the introduction of surface dampening.

N=12 Damping.

a/b	$\theta$ (deg.)	Numerical $\Delta P$ (Pa)	Theoretical		% Deviation $\Delta P$	#cells	End t(s)	# Steps	Oscil. (+/- Pa)
			$\gamma$ (1/m)	$\Delta P$ (Pa)					
1	90	0	4,08E-13	2,96E-14	-	288	3,0E-02	-	
1	70	159	2,28E+03	1,65E+02	3,8	288	3,0E-02	531	
1	50	317	4,29E+03	3,11E+02	2,0	288	3,0E-02	507	
1	30	459	5,77E+03	4,19E+02	9,7	288	3,0E-02	465	
2	70	159	2,28E+03	1,65E+02	3,8	144	3,0E-02	357	
2	50	309	4,29E+03	3,11E+02	0,5	144	3,0E-02	394	
2	30	450	5,77E+03	4,19E+02	7,5	144	3,0E-02	357	
1/2	70	165	2,28E+03	1,65E+02	0,2	576	3,0E-02	636	
1/2	50	342	4,29E+03	3,11E+02	10,1	576	3,0E-02	694	
1/2	30	437	5,77E+03	4,19E+02	4,4	576	3,0E-02	577	

General Notes: There are some oscillations in the P field in time -> P found as a mean value. # Steps increase because of CFL.  
 Oscillations: Surface capillary waves (relation found depending on  $\sqrt{\sigma/\rho}$ )

N=16 Damping.

a/b	$\theta$ (deg.)	Numerical $\Delta P$ (Pa)	Theoretical		% Deviation $\Delta P$	#cells	End t(s)	# Steps	Oscil. (+/- Pa)
			$\gamma$ (1/m)	$\Delta P$ (Pa)					
1	70	161,5	2,28E+03	1,65E+02	2,3	512	3,0E-02	709	
1	50	320	4,29E+03	3,11E+02	3,0	512	3,0E-02	738	
1	30	451	5,77E+03	4,19E+02	7,7	512	3,0E-02	719	

General Notes: There are some oscillations in the P field in time -> P found as a mean value.

N=40 T\_cal=25 min Damping.

a/b	$\theta$ (deg.)	Numerical $\Delta P$ (Pa)	Theoretical		% Deviation $\Delta P$	#cells	End t(s)	# Steps	Oscil. (+/- Pa)
			$\gamma$ (1/m)	$\Delta P$ (Pa)					
1	50	320	4,29E+03	3,11E+02	3,0	3200	2,0E-03	147	

N=40 High Damping.

a/b	$\theta$ (deg.)	Numerical $\Delta P$ (Pa)	Theoretical		% Deviation $\Delta P$	#cells	End t(s)	# Steps	Oscil. (+/- Pa)
			$\gamma$ (1/m)	$\Delta P$ (Pa)					
1	50	320	4,29E+03	3,11E+02	3,0	3200	2,0E-03	100	
1	50	324	4,29E+03	3,11E+02	4,3	3200	1,0E-02	441	

N=40

No Damping

a/b	$\theta$ (deg.)	Numerical $\Delta P$ (Pa)	$\kappa$ (1/m)	Theoretical $\Delta P$ (Pa)	% Deviation $\Delta P$	#cells	End t(s)	# Steps	Os oil (+/- Pa)
1	50	320	4,29E+03	3,11E+02	3,0	3200	2,0E-03	715	6

N=40    T\_calc=3 h    No Damping (~~oil~~ aspect changed a factor 4)     $\sigma_{new}= 0,29$

a/b	$\theta$ (deg.)	Numerical $\Delta P$ (Pa)	$\kappa$ (1/m)	Theoretical $\Delta P$ (Pa)	% Deviation $\Delta P$	#cells	End t(s)	# Steps	Os oil (+/- Pa)
1	50	1294	4,29E+03	1,24E+03	4,1	3200	2,0E-03	1605	29

- The numerical value of  $\Delta P$  is found after the oscillations stop.
- The drastic reduction in number of time steps needed when damping is applied i.e. a smaller  $\delta t$  because of smaller velocities at the surface.
- See the Matlab generated graphs in the main report for further details.

N=12, a/b=1,  $\theta=50$  deg.  
 Marangoni option activated.  
 $\Delta P_{theory}=311$  Pa  
 $\Delta P_{num}=625$  Pa +/- 28 Pa



**Second Slide :**

Simulation (2D)				Inlet BC					
$\Delta P$ b/N	F <sub>wall</sub>	h <sub>0</sub> *N	w*N	G	h <sub>0</sub> /e(Ca)	$\Delta P$ <sub>bif</sub> (Ca)	w/g(Ca)	Continuity	
5,00E+00	1,77E-01	4,43E-06	5,01E-02	1333,33	5,61E-01	3,74E+00	9,53E-01	a 7,51E-06	
5,00E+01	3,25E-01	8,13E-06	6,92E-02	13333,33	4,75E-01	7,96E+00	6,07E-01	b 1,04E-05	
8,40E+01	3,85E-01	9,63E-06	5,40E-02	20000,00	4,94E-01	1,03E+01	4,16E-01	c 8,11E-06	
1,00E+02	4,25E-01	1,06E-05	6,13E-02	26666,67	4,95E-01	1,01E+01	4,28E-01	d 9,20E-06	
1,70E+02	4,95E-01	1,24E-05	8,86E-02	40000,00	4,98E-01	1,28E+01	5,35E-01	e 1,33E-05	
1,90E+02	5,40E-01	1,35E-05	9,84E-02	53333,33	4,92E-01	1,17E+01	5,38E-01	f 1,48E-05	
3,10E+02	6,20E-01	1,55E-05	1,15E-01	80000,00	4,90E-01	1,44E+01	5,47E-01	g 1,73E-05	
4,00E+02	7,40E-01	1,85E-05	1,35E-01	133333,33	4,90E-01	1,31E+01	5,36E-01	h 2,02E-05	
4,00E+02	6,00E-01	2,00E-05	1,52E-01	133333,33	5,26E-01	1,29E+01	5,99E-01	h2	

Simulation (2D)				Inlet BC					
$\Delta P$ b/N	F <sub>wall</sub>	h <sub>0</sub> *N	w*N	G	h <sub>0</sub> /e(Ca)	$\Delta P$ <sub>bif</sub> (Ca)	w/g(Ca)	Continuity	
2,50E+02	5,25E-01	1,91E-05	1,28E-01	80000,00	6,00E-01	1,15E+01	6,07E-01	h 1,93E-05	